気象庁
Japan Meteorological Agency

CLIMATE CHANGE MONITORING REPORT 2018

September 2019

Published by the
Japan Meteorological Agency

1-3-4 Otemachi, Chiyoda-ku, Tokyo 100-8122, Japan

Telephone +81 3 3211 4966
Facsimile +81 3 3211 2032
E-mail iao-jma@met.kishou.go.jp

CLIMATE CHANGE MONITORING REPORT 2018

September 2019

JAPAN METEOROLOGICAL AGENCY

Preface

The Japan Meteorological Agency (JMA) has published annual assessments under the title of *Climate Change Monitoring Report* since 1996 to highlight the outcomes of its activities (including monitoring and analysis of atmospheric, oceanic and global environmental conditions) and provide up-to-date information on climate change in Japan and around the world.

In 2018, extreme meteorological phenomena such as heavy rainfall, droughts and heat waves occurred worldwide. Japan experienced particularly significant rainfall from its western part to the Tokai region during the Heavy Rain Event of July 2018, when overall precipitation nationwide was the highest since 1982, and extremely high temperatures subsequently persisted throughout the whole country other than the Okinawa/Amami region. Both the monthly mean temperature for July and the seasonal mean temperature for summer in eastern Japan were the highest since 1946.

The increasing frequency and scale of such extreme weather events are considered to stem from global warming. JMA, in consultation with the Advisory Panel on Extreme Climatic Events, has concluded that the Heavy Rain Event of July 2018 and the subsequent heatwave may have been linked to global warming.

As global warming continues, the frequency and scale of extreme events are expected to increase. The Paris Agreement will be implemented in 2020, forming a new international framework with which to combat climate change and support adaptation to its effects. With Japan's introduction of the Climate Change Adaptation Act in December 2018, national and local governments are currently stepping up their efforts in this regard.

This report is intended to provide a scientific basis for better implementation of measures relating to climate change and to raise awareness of global environmental issues.

Yasuo Sekita

Yasuo Sekita
Director-General
Japan Meteorological Agency

Index

Topics

I The Heavy Rain Event of July 2018 and the persistent heatwave of summer 2018

○ During the Heavy Rain Event of July 2018, Japan experienced unprecedented heavy rainfall, especially over western Japan and Tokai region. Overall precipitation observed at AMeDAS stations throughout Japan in early July 2018 was extremely high in comparison with past heavy rainfall events since 1982.

○ Seasonal mean temperature in eastern Japan was the highest on record for summer since 1946. On July 23, a new national record maximum temperature of 41.1°C was recorded at Kumagaya in Saitama Prefecture.

I.1 The Heavy Rain Event of July 2018

(1) Characteristics of climate condition

Japan experienced an extreme climate event that brought unprecedented amounts of precipitation especially over western Japan and Tokai region from June 28 to July 8, 2018, which was officially named "The Heavy Rain Event of July 2018" by the Japan Meteorological Agency (JMA), in the presence of the stationary Baiu front and Typhoon Prapiroon (T1807). Some of the JMA Automated Meteorological Data Acquisition System (AMeDAS) stations in Shikoku and Tokai regions recorded more than 1,800 and 1,200 mm, respectively, during the period. Some areas experienced two to four times the precipitation of the monthly climatological normal for July (Figure I.1-1 (a)). Overall precipitation at 966 selected AMeDAS stations throughout Japan in early July 2018 reached 208,035.5 mm (215.4 mm per station), which was the highest among any 10-day period starting 1st, 11th and 21st of the months since 1982, highlighting the nationwide significance of this event.

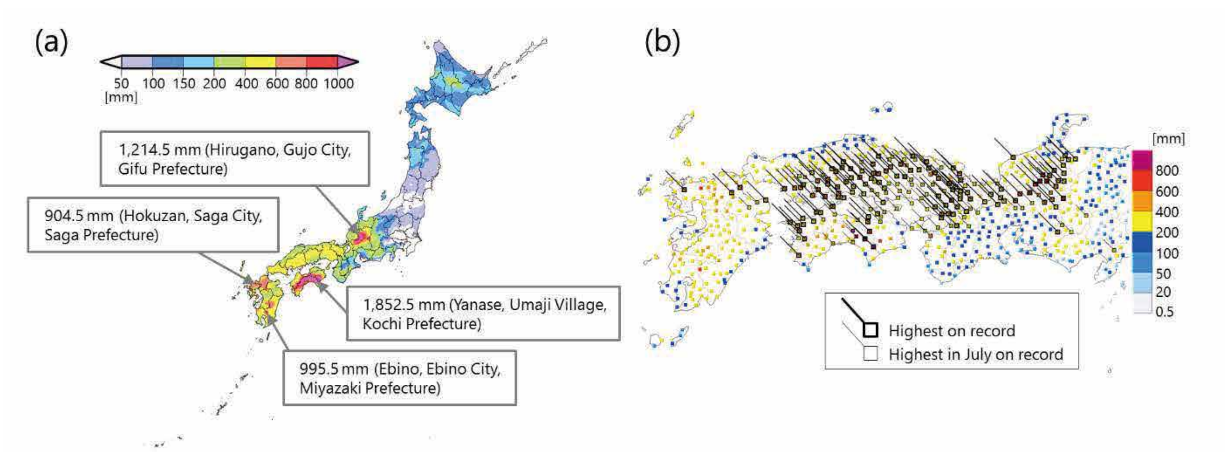

Figure I.1-1 Precipitation amounts (mm) observed during the Heavy Rain Event of July 2018 for the period from June 28 to July 8, 2018. (a) 11-day total over Japan. (b) Maximum 72-hour precipitation during the 11-day event over western Japan and Tokai region

Thick and thin squares with short lines in (b) indicate stations at which the 72-hour maxima during the event were the highest ever any time since 1982 and the highest in July, respectively.

In comparison with past heavy rainfall events caused by frontal systems and typhoons, a prominent characteristic of this rain event is that the record-breaking local precipitation, particularly within 48 to 72 hours, was observed extensively over western Japan and Tokai region, including the Seto Inland Sea side of Chugoku and Shikoku regions, where monthly precipitation normal are lower than in the surroundings (Figure I.1-1 (b)).

(2) Characteristics of atmospheric circulation

During the heavy rainfall observed over western Japan and Tokai region from July 5 to 8, the Baiu front was distinct over western Japan in association with the development of the Okhotsk High to the west of Japan and expansion of the North Pacific Subtropical High (NPSH) to the southeast of Japan (Figure I.1-2 (b)). The persistent confluence of two massively moist air streams over the south of Japan brought unprecedented amounts of moisture to western Japan (Figure I.1-2 (c)). In addition, persistent ascent was associated with the stationary Baiu front around western Japan. Some areas were also affected by line-shaped convective precipitation systems.

The synoptic-scale conditions observed around Japan were attributable to pronounced meanders of the upper-level Polar-front Jet (PFJ) and the Subtropical Jet (STJ). The development of the Okhotsk High and the expansion of the NPSH were associated with northward meanders of the PFJ around Eastern Siberia and the STJ over the east of Japan, respectively, with upper-level quasi-stationary anticyclonic anomalies there (Figure I.1-2 (a)). In addition, the upper-level trough lingering around the Korean Peninsula was associated with the southward meander of the STJ in the area (Figure I.1-2 (a)).

The primary synoptic-scale factors and large-scale atmospheric circulation contributing to the heavy rainfall observed over western Japan and Tokai region from July 5 to 8 are summarized in Figures I.1-3 and I.1-4, respectively.

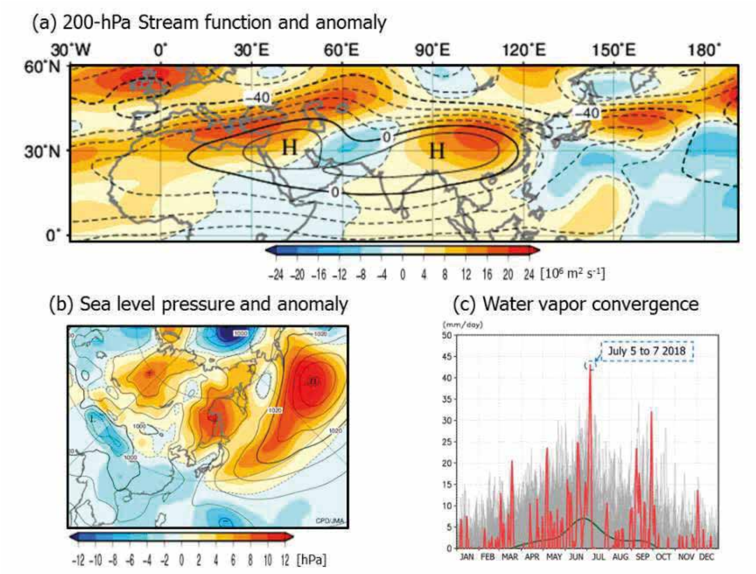

Figure I.1-2 (a) 200-hPa stream function (contours) and anomaly (shade), (b) sea level pressure (contours) and anomaly (shade) for the period from July 4 to 8, 2018, (c) three-day running-mean timeseries representation of vertically integrated horizontal moisture flux convergence (mm per day) within 31.25 – 35°N, 130 – 135°E.

The contours are drawn at intervals of (a) 10 x 10^6 m^2 per s and (b) 4 hPa. In (c), red, grey and green lines are annual timeseries representations for 2018, other individual years from 1958 to 2017 and the normal. The base period for the normal is 1981 – 2010.

(3) Long-term changes in the intensity of relatively prolonged extreme heavy rainfall and atmospheric water vapor content over Japan in association with global warming

On a longer time scale, a trend of increased intensity in extreme precipitation events in Japan is observed. Figure I.1-5 indicates the average of ratios against the baseline (the 1981 – 2010 average) for annual maximum 24-, 48- and 72-hour precipitation over Japan based on AMeDAS observation data. From 1976 to 2018, annual maximum 24- and 48-hour precipitation increased at rates of 3.7 and 3.9% per decade (statistically significant at a confidence level of 95%), respectively, and annual maximum 72-hour precipitation increased at a rate of 3.6% per decade (statistically significant at a confidence level of 90%). An intensity of extremely heavy rainfall lasting one to several days over Japan was approximately 10% higher than that shown in data from 30 years before.

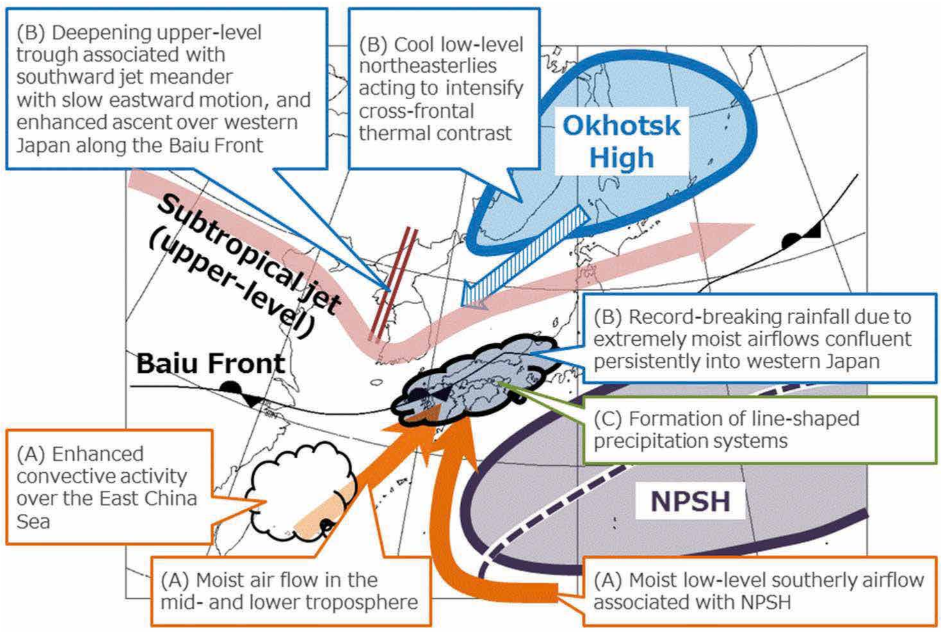

Figure I.1-3 A schematic for primary synoptic-scale factors behind the extreme rainfall event that occurred over western Japan and Tokai region from July 5 to 8, 2018

NPSH stands for the North Pacific Subtropical High. Purple dashed line shows normal position of the NPSH.

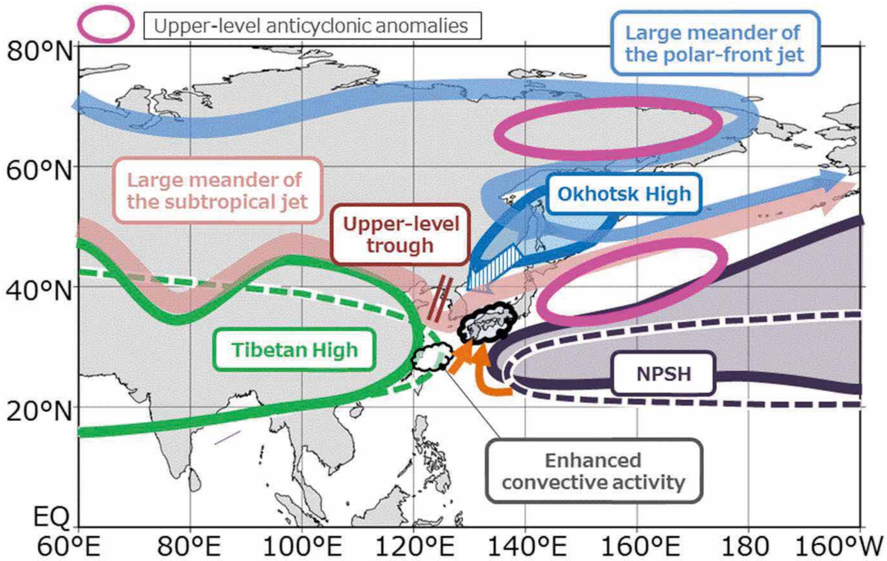

Figure I.1-4 A schematic for large-scale atmospheric circulation behind the extreme rainfall event that occurred over western Japan and Tokai region from July 5 to 8, 2018

NPSH stands for the North Pacific Subtropical High. Purple and green dashed lines show normal position of the NPSH and the Tibetan High, respectively.

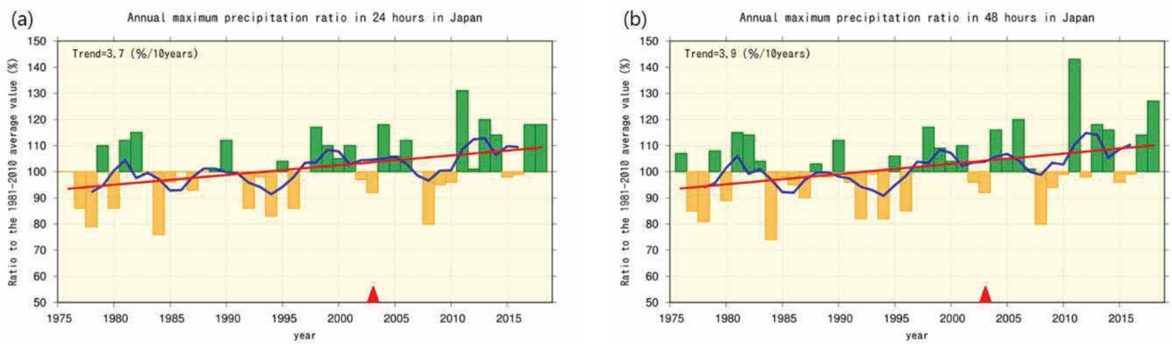

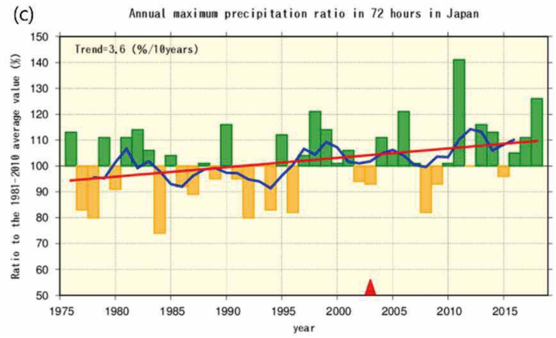

Figure I.1-5 Annual maximum precipitation ratios (%) for (a) 24-hour, (b) 48-hour and (c) 72-hour periods over Japan for the period from 1976 to 2018

Annual averages for each year are presented as ratios against the baseline (i.e., the 1981 – 2010 average). Bars indicate annual maximum precipitation ratios for each year based on 685 AMeDAS stations where ongoing observation was conducted from 1976 to 2018. The blue and red lines indicate five-year running means and the long-term linear trend, respectively. Red triangles indicate the change in observational periodicity for hourly precipitation from every hour to every 10 minutes in 2003.

This trend of increased intensity in extreme precipitation events in Japan may be attributable to a long-term increasing trend of the amount of water vapor in the atmosphere associated with a background of long-term atmospheric warming. It is widely accepted that saturated water vapor amounts increase by approximately 7% for each 1°C increment in air temperature. For example, the average ratios against the baseline (the 1981 – 2010 average) for seasonal mean 850-hPa specific humidity in summer (June-July-August) at 13 upper-air observation stations in Japan increased at a rate of 2.7% per decade from 1981 to 2018 (statistically significant at a confidence level of 99%) (Figure I.1-6). Atmospheric water vapor content over Japan therefore increased by approximately 8% compared to the data for 30 years ago. Though more investigation is needed, these trends suggests a possibility that the Heavy Rain Event of July 2018 may be influenced by the increase of water vapor in association with global warming.

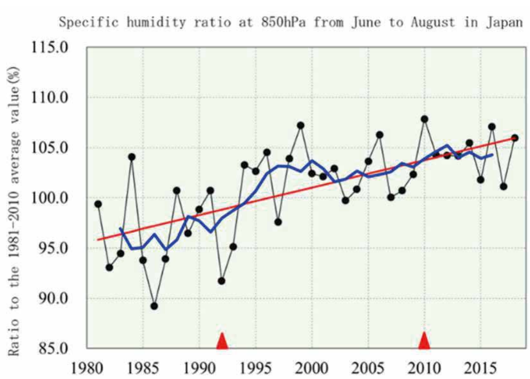

Figure I.1-6 Seasonal (June-July-August) mean ratios of 850-hPa specific humidity over Japan for the period from 1981 to 2018

The data used in this analysis were based on radiosonde observations (balloon-borne instrument platforms with a radio-transmitting device) at 13 upper-air observation stations in Japan. Values for each year are presented as ratios against the baseline (i.e., the 1981 – 2010 average). The thin black line indicates the ratio of seasonal mean 850-hPa specific humidity for each year. The blue and red lines indicate five-year running means and the long-term linear trend, respectively. Red triangles indicate instrument change; values for the term between these marks may be slightly higher than those in other terms.

I.2 Heat wave in summer 2018

(1) Characteristics of climate condition

In summer 2018, eastern and western Japan experienced unprecedentedly hot summer conditions. The July-mean and seasonal-mean temperature anomalies for 2018 in eastern Japan were the highest on record since 1946 at +2.8°C and +1.7°C above the normal, respectively (Figure I.2-1 (a)), and 48 of 153 surface observation stations in Japan reported record or joint-record maximum temperatures for summer. Several reported maximum temperatures exceeding 40°C at the peak of the heatwave, and a new national record maximum temperature of 41.1°C was recorded at Kumagaya in Saitama Prefecture on July 23. At many observation stations, daily maximum temperatures often exceeded 30°C and sometimes even 35°C. A cumulative total of 6,483 AMeDAS stations observed daily temperatures of 35°C or higher from June to September 2018, exceeding the previous record in 2010 among data going back to 1976 (Figure I.2-1 (b)).

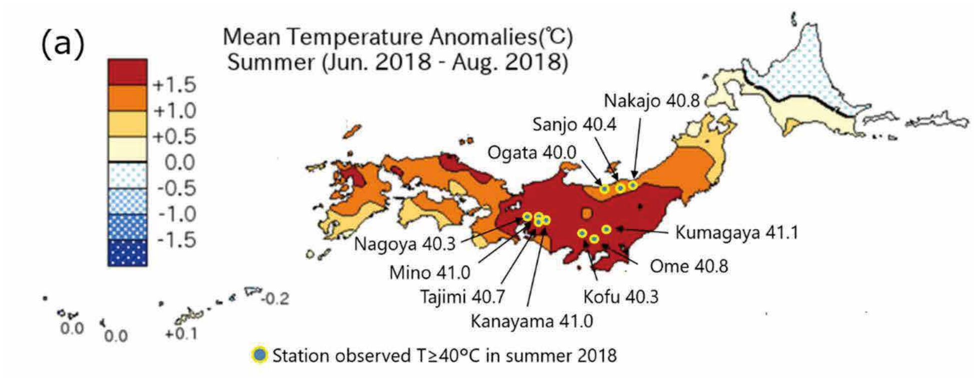

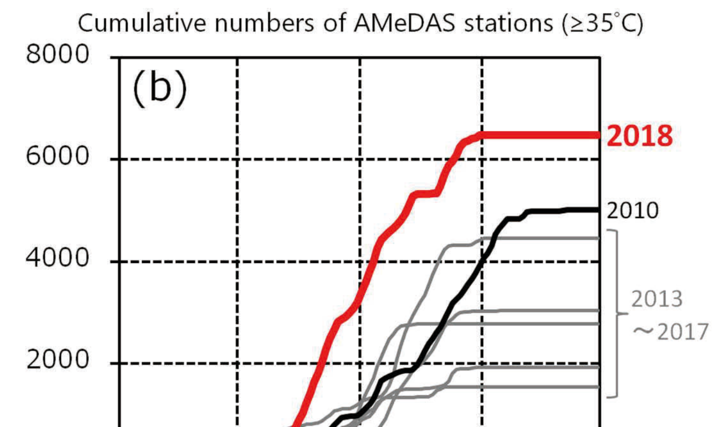

Figure I.2-1 (a) Seasonal mean temperature anomaly (°C) for Japan in summer 2018 and (b) seasonal evolution (June through September) of cumulative numbers of AMeDAS stations with daily maximum temperatures of 35 °C or higher

In (a), stations observed daily maximum temperatures of 40 °C or higher in 2018 summer are also shown. The base period for the normal is 1981 – 2010. In (b), red, black, and grey lines are for 2018, 2010, and for 2013 through 2017. Numbers of available AMeDAS stations are 918 for 2010, 927 for 2013, 2015 and 2018, 923 for 2014, and 929 for 2016 and 2017.

(2) Characteristics of atmospheric circulation

From mid-July to August, both the surface NPSH and the upper-tropospheric Tibetan High persisted in their extension to the main islands of Japan (Figures I.2-2 (a), (b)). Surface temperatures in Japan increased, due mainly to high-pressure systems with warmer-than-normal air covering the islands, predominantly sunny conditions and downward flow associated with the pressure systems.

The expansion of the Tibetan High to Japan was attributable to the northward meandering of the STJ in the vicinity of Japan with varying but persistent extents (Figure I.2-2 (a)). The expansion of the NPSH in the vicinity of Japan was attributable to enhanced convective activity over and around the Philippines (Figure I.2-2 (c)) as well as the significant meandering of the STJ.

In addition to the above effects associated with anomalous circulation, suspected factors behind the heatwave over Japan include marked tropospheric warmth over the Northern Hemisphere mid-latitudes from spring 2018 and a long-term rising trend of surface air temperatures against a background of global warming.

Primary factors behind the unprecedentedly hot conditions observed in summer, especially in mid- and late July 2018, are summarized in Figure I.2-3.

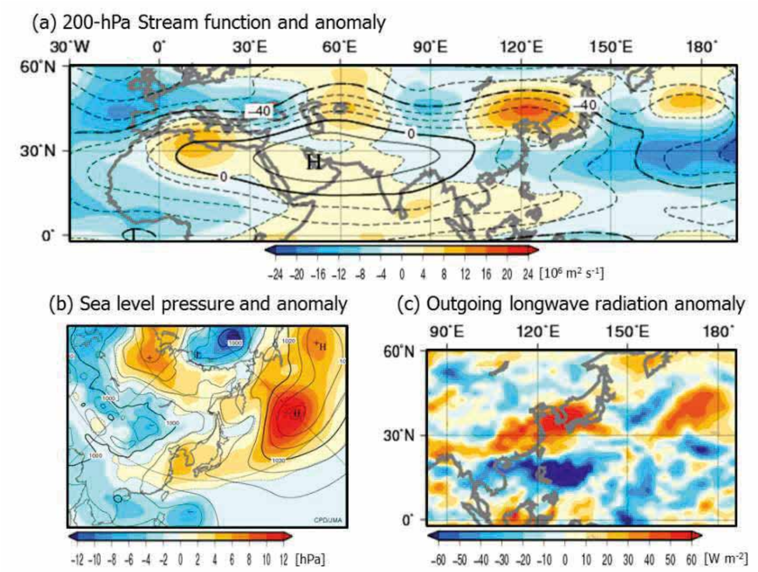

Figure I.2-2 (a) 200-hPa stream function (contours) and anomaly (shade), (b) sea level pressure (contours) and anomaly (shade), (c) outgoing longwave radiation (OLR) anomaly for the period from July 15 to 19, 2018.

The contours are drawn at intervals of (a) 10 x 10^6 m^2 per s and (b) 4 hPa. The base period for the normal is 1981 – 2010.

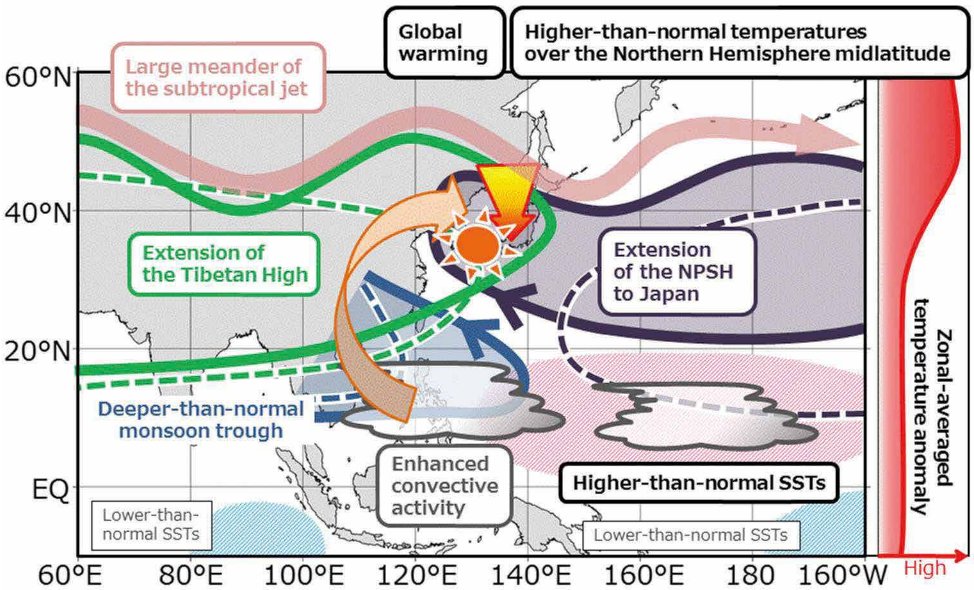

Figure I.2-3 A schematic for large-scale atmospheric circulation behind the heat wave in summer 2018, especially in the middle and late July 2018.

NPSH and SST stand for the North Pacific Subtropical High and sea surface temperature, respectively. Purple, green and blue dashed lines show normal positions of the NPSH, the Tibetan High and the monsoon trough, respectively.

II The recovery trend of the Antarctic ozone hole

- ○ Concentrations of ozone-depleting substances have declined gradually since the mid-1990s.
- ○ Although 2018 weather conditions was likely to have supported stratospheric ozone depletion, the maximum area of the ozone hole in 2018 was less than those observed from the mid-1990s to the mid-2000s.
- ○ The maximum area of the Antarctic ozone hole has exhibited a significant declining tendency since 2000.

The formation and development of the ozone hole are closely related to atmospheric concentrations of ozone-depleting substances (ODSs) such as chlorofluorocarbons (CFCs), and to weather conditions over the Antarctic. ODS concentrations have gradually decreased since the second half of the 1990s thanks to the regulation of their production under the 1987 Montreal Protocol (Figure 3.2-7). As a result, there are positive signs regarding the recovery of the ozone layer worldwide. However, the extent of recovery over the Antarctic remains unclear due to significant annual fluctuations in the size of the ozone hole due to variations in temperature, winds and other upper-atmospheric conditions.

In 2018, lower-than-usual 50 hPa temperatures in the stratosphere over the Antarctic supported the development of polar stratospheric clouds (PSCs). Figure II.1 shows annual changes in the maximum area of the ozone hole over the Antarctic, and the area of stratospheric temperatures below –78°C (indicating ozone hole development) in August and the month of the ozone hole appearance. The data indicate that larger areas of stratospheric temperatures below –78°C are associated with greater maximum hole areas. However, although the area of the former in 2018 was relatively large, the maximum area of the Antarctic ozone hole, 24.6 million km^2 was below the average for the period from the mid-1990s to the mid-2000s. There are also significant indications that the maximum area of the ozone hole has declined since 2000 in spite of the relatively large 2018 value. From these observations, it may be inferred that the Antarctic ozone hole has begun recovering.

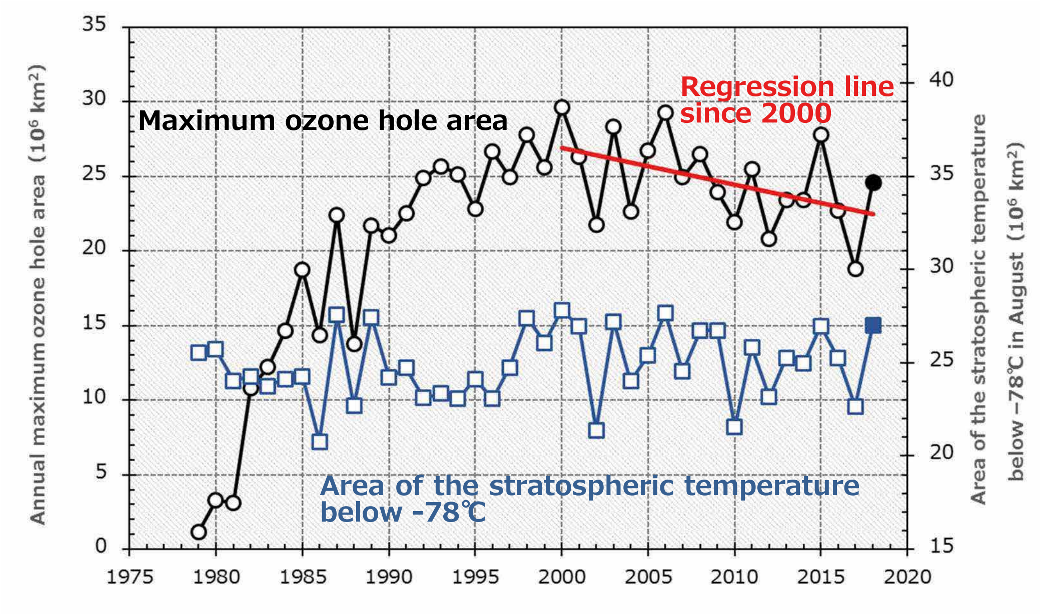

Figure II.1 Annual changes in the maximum area of the Antarctic ozone hole, and the area of stratospheric temperatures below –78°C in August

Black line with circles: maximum ozone hole area (left axis)

Blue line with squares: area of stratospheric temperatures below –78°C in August (right axis)

Red line: trend of the maximum ozone hole area from 2000 to 2018

Maximum ozone hole areas are based on NASA satellite observation data.

Areas of stratospheric temperatures below –78°C are based on JRA-55 data.

Scientific assessments of the ozone depletion situation, including commentary on current and expected conditions, are periodically issued by the World Meteorological Organization (WMO) and the United Nations Environmental Programme (UNEP). The Executive Summary of Scientific Assessment of Ozone Depletion 2018 (published on 5 November 2018 in association with the 30th Meeting of the Parties to the Montreal Protocol in Quito, Ecuador) reported on the recovery of the Antarctic ozone hole and the situation of stratospheric ozone. However, as ODS concentrations are still high and the hole remains large, ongoing monitoring of stratospheric ozone is required.

III JMA's provision of long-term ocean analysis data for the 137°E meridian

○ The Japan Meteorological Agency has conducted oceanographic observation along the 137ºE meridian for over 50 years using two dedicated research vessels, and now provides data from analysis of the long-term body of data collected.

The Japan Meteorological Agency (JMA) has conducted oceanographic observation along the 137ºE meridian since 1967 using two dedicated research vessels (Figure **III.1**). The unique body of data collected during this time is widely referenced by domestic and overseas researchers to help elucidate the structure of the northwest Pacific and clarify variations in the Kuroshio current, the El Niño-Southern Oscillation and long-term oceanic variations relating to climate variability (Oka et al. 2018). Publications based on these data were cited in the 2013 Intergovernmental Panel on Climate Change's Fifth Assessment Report. The information is a valuable scientific resource for validating the reproducibility of oceanic variations in global warming prediction modeling, and is expected to contribute to the formulation of plans for adaptation to the impacts of climate change. As the unique data collected by JMA research vessels and other operators are characterized by various horizontal and vertical observation intervals, analysis based on gridding and unification was applied in the production of JMA's Oceanographic Section Time-series Dataset (for temperature and salinity) to facilitate and encourage the use of such information.

As an example, the figure on the right below shows the variability of the Kuroshio current and water temperature for El Niño/La Niña events. In the La Niña event of summer 1975, water temperatures were higher in the 137°E section near 7°N between depths of 100 and 300 m. The Kuroshio large meander continued in summer 2017, the current's path was shifted southward of its normal position near 31°N, and water temperatures north of the path were lower than normal. Long-term analysis of the 137°E section has helped to clarify variations in the path of the Kuroshio current, El Niño/La Niña-related phenomena and long-term ocean variability.

JMA continues to provide long-term analysis data online at
https://www.data.jma.go.jp/gmd/kaiyou/db/mar_env/results/OI/137E_OI_e.html

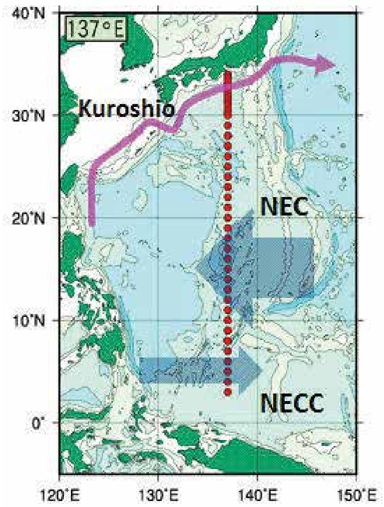

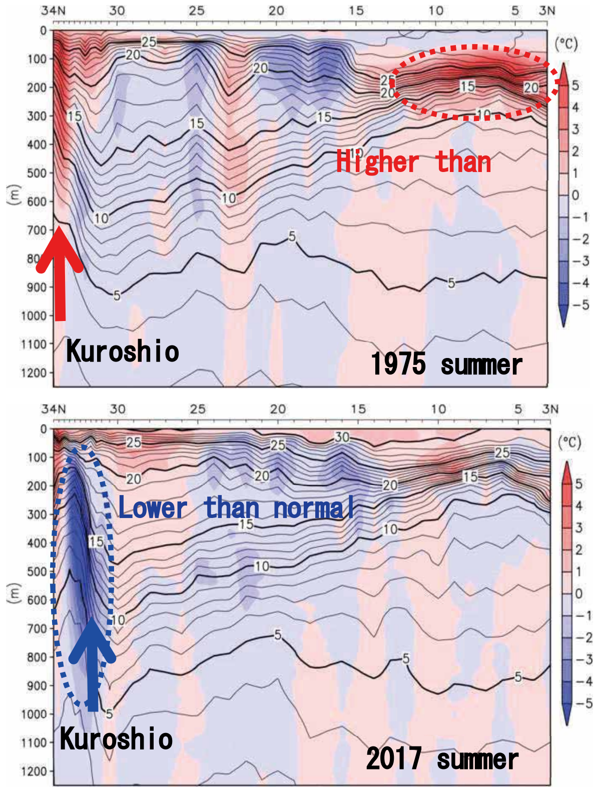

Figure III.1 Observation stations along the 137°E meridian

Hydrographic stations (red circles) and the main ocean current system (NEC: North Equatorial Current; NECC: North Equatorial Counter Current).

Figure III.2 Vertical sections of temperature for summer 1975 (top) and 2017 (bottom)

Contours indicate analysis values (thick/thin lines for 5°/1°) colored to represent anomalies from the climatological normal (red: above normal; blue: below normal).

* Climatological normal: average from 1981 to 2010

Chapter 1 Climate in 2018

1.1 Global climate summary

- ○ Extremely high summer temperatures were frequently observed worldwide, especially in the Northern Hemisphere during boreal summer, with records being set in Europe, East Asia and the southwestern USA.
- ○ Extensive damage and numerous fatalities were caused by heavy rain from eastern to western Japan (June – July), in India (June – September), in Nigeria (July – September) and from northern to central parts of Eastern Africa (March – May), while significant agricultural losses were caused by droughts in and around northern Argentina (January – March) and in southeastern Australia (January – September).

Major extreme climate events[1] and weather-related disasters occurring in 2018 are shown in Figure 1.1-1 and Table 1.1-1.

Extremely high temperatures were frequently observed in many parts of the world ((1), (2), (5), (7), (10), (11), (12), (14), (16), (19), (21), (23), (25), (26) in Figure 1.1-1), even though the La Niña event that began in boreal fall 2017 continued to boreal spring 2018. Record temperatures were observed in Europe, East Asia and the southwestern USA in boreal summer ((14), (5), (21) in Figure 1.1-1), and seasonal mean temperatures for summer (June – August) were the highest on record in eastern Japan, Korea, China and the southwestern USA since 1946, 1973, 1961 and 1895, respectively (Japan Meteorological Agency, Korea Meteorological Administration, China Meteorological Administration, National Oceanic and Atmospheric Administration, USA; (5), (21) in Figure 1.1-1). An all-Japan record daily maximum temperature of 41.1°C was recorded at Kumagaya in Saitama Prefecture.

Contrasting extremes of high and low precipitation were frequently observed in southern and central Europe, respectively ((15) and (13) in Figure 1.1-1). Extremely high precipitation amounts were observed from northeastern to southern parts of the USA (February, May, August – December; (20) in Figure 1.1-1), and seasonal precipitation amounts in fall (September – November) were the highest, second highest and third highest in the southern, northeastern and northern Midwest USA, respectively (National Oceanic and Atmospheric Administration, USA).

Climate extremes caused immense damage worldwide. Japan experienced unprecedentedly heavy rain from its western part to the Tokai region around early July due to a stationary Baiu front and Typhoon Prapiroon, which resulted in 224 fatalities (Cabinet Office of Japan, as of 9 October 2018; (6) in Figure 1.1-1). Heavy rain caused more than 1,500 fatalities in India (June – September) and more than 300 fatalities in Nigeria (July – September) ((9), (17) in Figure 1.1-1). From northern to central parts of Eastern Africa, intermittent heavy rain from March to May and Tropical Storm Sagar in May resulted in more than 500 fatalities ((18) in Figure 1.1-1). Extreme drought conditions in southeastern Australia (January – September; (27) in Figure 1.1-1) made 2018 the worst year in terms of farm cash income since 1978, prompting comparisons to the extreme drought conditions of 2002 – 2003. Total precipitation in New South Wales, Australia, from January to September was the third lowest for the period since 1900 (Bureau of Meteorology, Australia).

---

1 Extreme climate events are defined by anomalies or ratios to climatological normals. Normals represent mean climate conditions at given sites, and are currently based on a 30-year mean covering the period from 1981-2010.

Annual mean temperatures were above normal in most parts of the world, and were very high from Alaska to northwestern Siberia, in the southern part of East Asia, from Micronesia to the central part of Southeast Asia, in the western part of South Asia, from Europe to the Middle East, in and around the southern part of Eastern Africa, from western to southeastern parts of the USA, from Central America to the eastern part of South America, and in Australia. Annual mean temperatures were below normal from eastern Canada to the northern USA, and were very low in and around the northeastern part of Central Asia (Figure 1.1-2).

Annual precipitation amounts were above normal from Mongolia to northern China, from eastern to central parts of Central Asia, from the northwestern part of the Middle East to the eastern part of Northern Africa, from southern Europe to the northwestern part of Northern Africa, and from northeastern to southern parts of the USA, and were below normal in the western part of Central Asia, from the northwestern part of South Asia to the southern part of the Middle East, and in southeastern Australia (Figure 1.1-3).

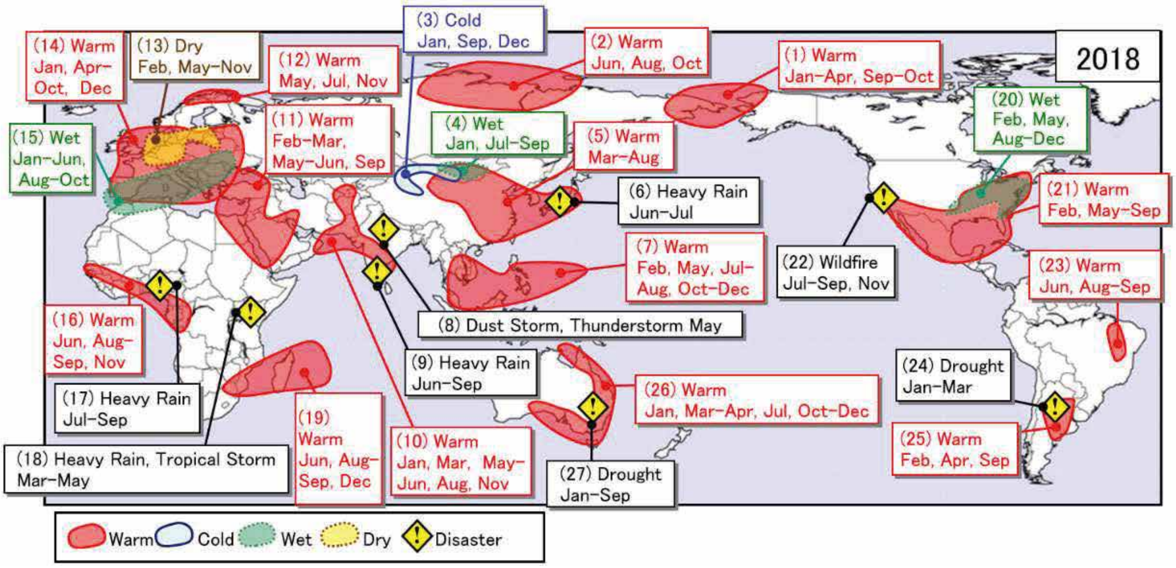

Figure 1.1-1 Major extreme events and weather-related disasters observed in 2018[2]

Schematic representation of major extreme climatic events and weather-related disasters occurring during the year.

“Warm”, Cold”, “Wet” and “Dry” indicate that monthly extreme events occurred three times or more during the year in these regions. JMA defines an extreme climate event as a phenomenon likely to happen only once every 30 years.

Data and information on disasters are based on official reports of the United Nations and national governments and databases of research institutes (EM-DAT).

EM-DAT: The Emergency Events Database - Université Catholique de Louvain (UCL) - CRED, D. Guha-Sapir - www.emdat.be, Brussels, Belgium.

2 Annual distribution maps for major extreme climatic events and weather-related disasters after 2008 are provided at JMA’s website.
https://ds.data.jma.go.jp/tcc/tcc/products/climate/annual/index.html

Table 1.1-1 Major extreme events and weather-related disasters occurring in 2018

No.	Event
(1)	Warm: from western Alaska to the eastern part of Eastern Siberia (January – April, September – October)
(2)	Warm: from the northwestern part of Eastern Siberia to the northwestern part of Central Siberia (June, August, October)
(3)	Cold: from southwestern Mongolia to northwestern China (January, September, December)
(4)	Wet: in and around central Mongolia (January, July – September)
(5)	Warm: from northern Japan to northwestern China (March – August)
(6)	Heavy Rain: from eastern to western Japan (June – July)
(7)	Warm: from northwestern Micronesia to the northwestern part of Southeast Asia (February, May, July – August, October – December)
(8)	Dust Storm and Thunderstorm: northern India (May)
(9)	Heavy Rain: India (June – September)
(10)	Warm: from the southern part of Central Asia to the southeastern part of South Asia (January, March, May – June, August, November)
(11)	Warm: in and around Middle East (February – March, May – June, September)
(12)	Warm: the northern Scandinavian Peninsula (May, July, November)
(13)	Dry: in and around central Europe (February, May – November)
(14)	Warm: from central to southern Europe (January, April – October, December)
(15)	Wet: from southern Europe to the northwestern part of Northern Africa (January – June, August – October)
(16)	Warm: from the western part of Western Africa to the northwestern part of Middle Africa (June, August – September, November)
(17)	Heavy Rain: Nigeria (July – September)
(18)	Heavy Rain and Tropical Storm: from the northern to central parts of Eastern Africa (March – May)
(19)	Warm: from Mauritius to northwestern South Africa (June, August – September, December)
(20)	Wet: from the northeastern to southern USA (February, May, August – December)
(21)	Warm: from the southern part of North America to the central part of Central America (February, May – September)
(22)	Wildfire: the western USA (July – September, November)
(23)	Warm: northeastern Brazil (June, August – September)
(24)	Drought: in and around northern Argentina (January – March)
(25)	Warm: from northern to central Argentina (February, April, September)
(26)	Warm: from eastern to southern Australia (January, March – April, July, October – December)
(27)	Drought: southeastern Australia (January – September)

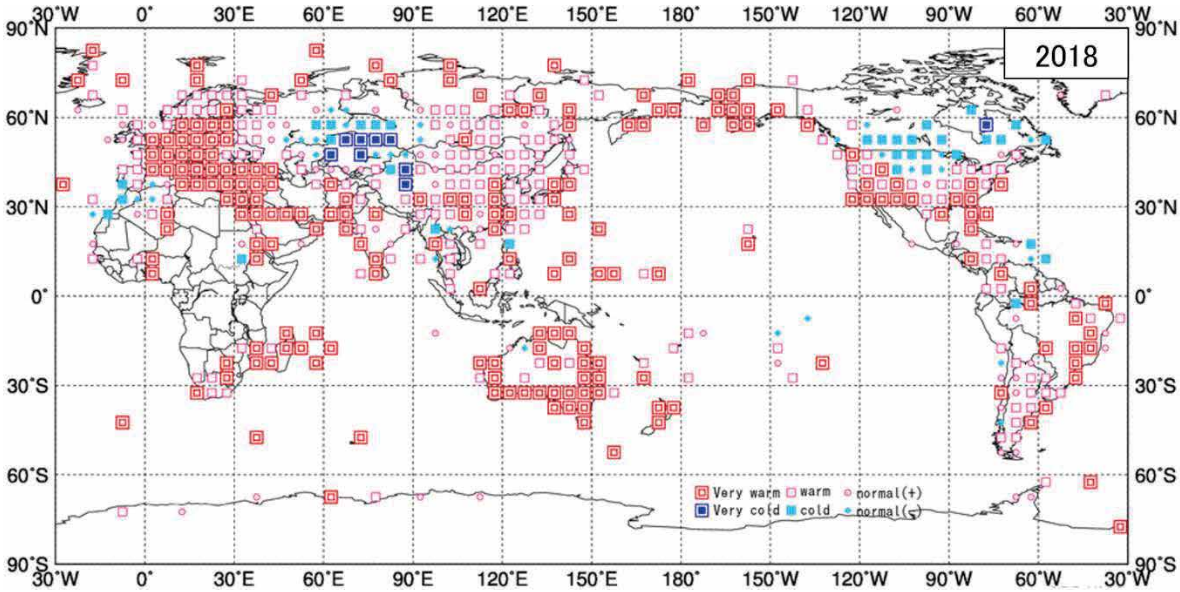

Figure 1.1-2 Annual mean temperature anomalies in 2018[3]

Categories are defined by the annual mean temperature anomaly against the normal divided by its standard deviation and averaged in 5° × 5° grid boxes. Red/blue marks indicate values above/below the normal calculated for the period from 1981 to 2010. The thresholds of each category are –1.28, –0.44, 0, +0.44 and +1.28[4]. Areas over land without graphical marks are those where observation data are insufficient or normal data are unavailable.

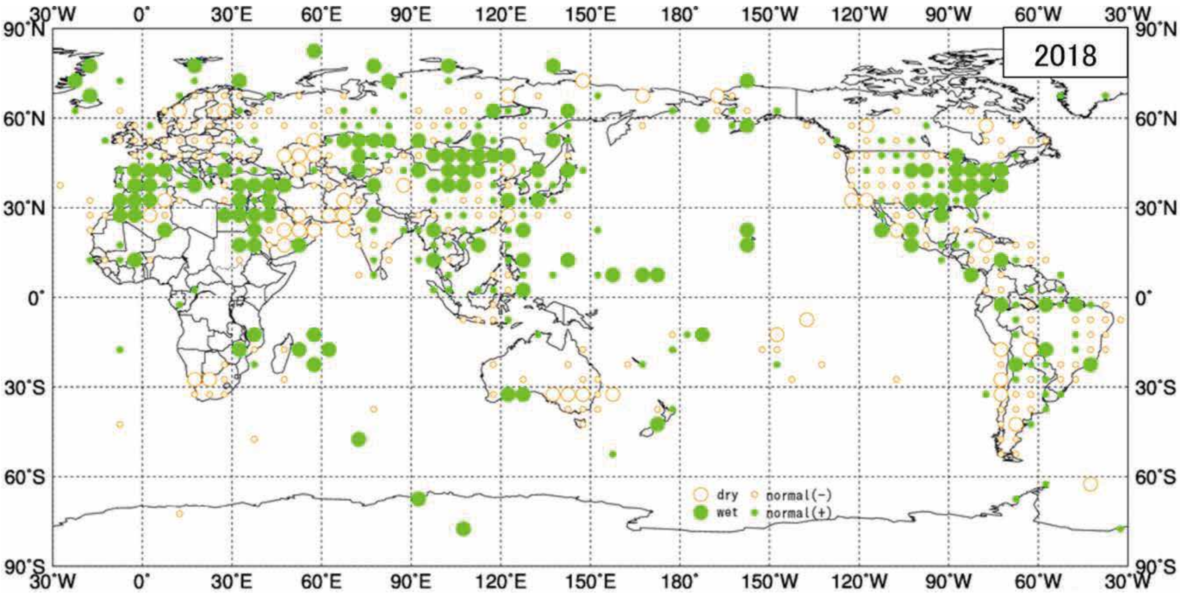

Figure 1.1-3 Annual total precipitation amount ratios in 2018

Categories are defined by the annual precipitation ratio to the normal averaged in 5° × 5° grid boxes. Green/yellow marks indicate values above/below the thresholds. The thresholds of each category are 70, 100 and 120% of the normal calculated for the period from 1981 to 2010. Areas over land without graphical marks are those where observation data are insufficient or normal data are unavailable.

3 Distribution maps for normalized annual mean temperature anomaly and precipitation amount ratio to normal after 2008 are provided at JMA's website.
https://ds.data.jma.go.jp/tcc/tcc/products/climate/annual/index.html

4 In normal distribution, values of 1.28 and 0.44 correspond to occurrence probabilities of less than 10 and 33.3%, respectively.

1.2 Climate in Japan[5]

- In winter (Dec. 2017 – Feb. 2018), seasonal mean temperatures were below normal nationwide with heavy snowfall on the Sea of Japan side of eastern Japan and elsewhere.
- In spring and summer, record-high seasonal mean temperatures were observed in eastern and western Japan.
- In early July, western Japan sustained significant damage from several days of unprecedentedly heavy rain.
- Typhoons Jebi and Trami made landfall on or approached Japan, causing storms and high tides.

1.2.1 Annual characteristics

The annual climate anomaly/ratio for Japan in 2018 is shown in Figure 1.2-1.

- Annual mean temperatures: above normal in nationwide, especially in eastern Japan
- Annual precipitation amounts: above normal nationwide except on the Pacific side of eastern Japan, especially on the Sea of Japan of northern Japan and on the Pacific side of western Japan
- Annual sunshine durations: above normal nationwide except in northern Japan

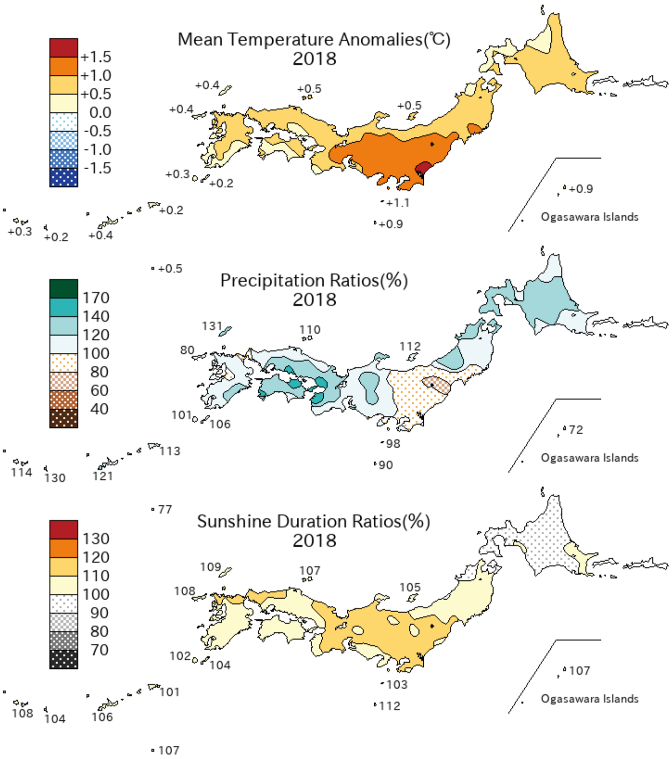

Figure 1.2-1 Annual climate anomaly/ratio for Japan in 2018
The base period for the normal is 1981 – 2010.

5 The term *significantly above normal* is used for cases in which observed mean temperatures or precipitation amounts exceed the 90th percentile for the base period (1981 – 2010), and *significantly below normal* is used when the corresponding figures fall below the 10th percentile.

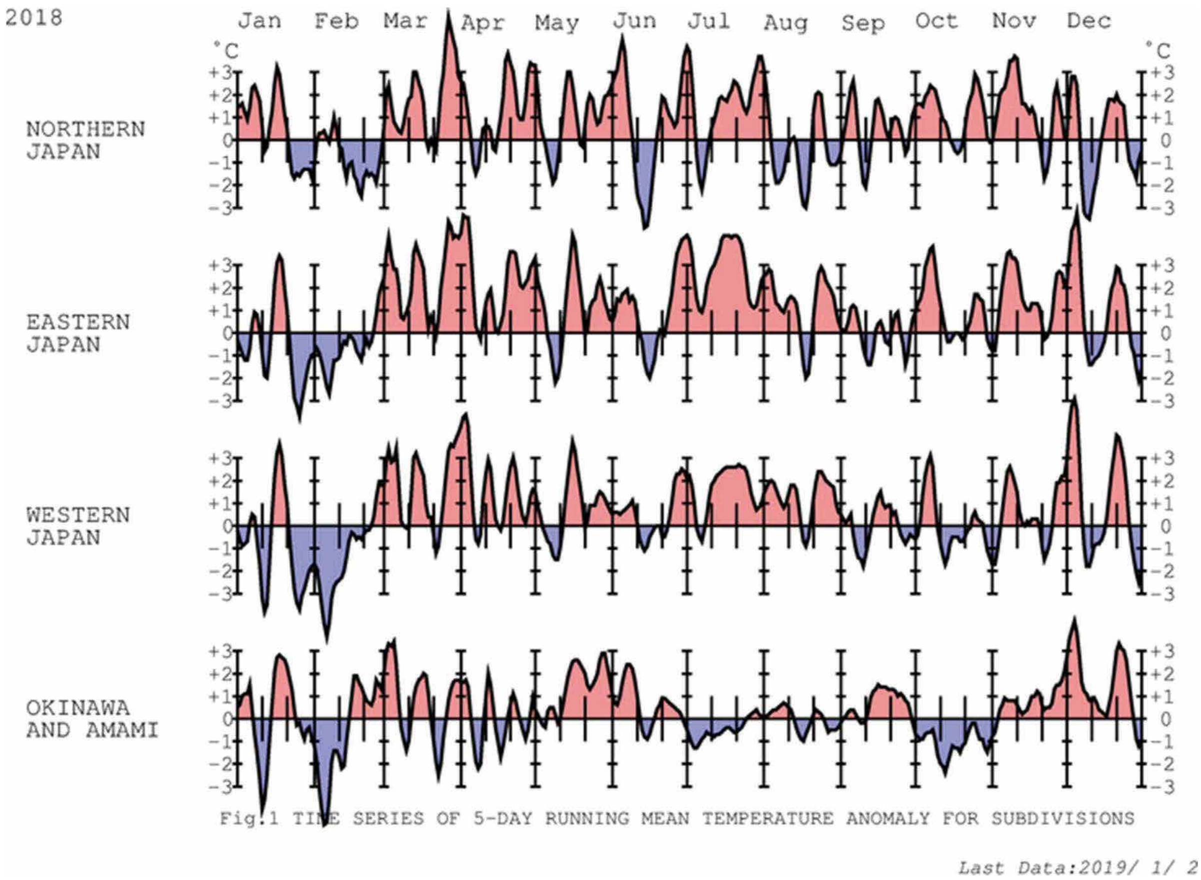

Figure 1.2-2 Five-day running mean temperature anomaly for divisions (January – December 2018)

The base period for the normal is 1981 – 2010.

1.2.2 Seasonal characteristics

Five-day running mean temperature anomalies for different divisions (January – December 2018) are shown in Figure 1.2-2, and seasonal anomalies/ratios for Japan in 2018 are shown in Figure 1.2-3. Numbers of observatories reporting record monthly and annual mean temperatures, precipitation amounts and sunshine durations (2018) are shown in Table 1.2-1.

(1) Winter (December 2017 – February 2018)

- Mean temperatures: below normal nationwide
- Precipitation amounts: significantly above normal on the Sea of Japan side of eastern and western Japan, above normal on the Sea of Japan side of northern Japan, below normal on the Pacific side of eastern Japan, on the Sea of Japan side of western Japan, and in Okinawa/Amami, near normal on the Pacific side of northern and western Japan
- Sunshine durations: significantly above normal on the Pacific side of eastern Japan, above normal on the Pacific side of western Japan and in Okinawa/Amami, near normal on the Pacific side of northern Japan, on the Sea of Japan side of eastern and western Japan

In association with a strong winter monsoon, seasonal mean temperatures were below normal nationwide. In particular, the value for western Japan was the lowest for 32 years at 1.2°C below the normal. On the Sea of Japan side from northern to western Japan, heavy clouds flowing in quickly from the Sea of Japan brought heavy snowfall and traffic disruption on the eastern side. The maximum snow depth in Fukui exceeded 140 cm for the first time in 37 years (147 cm).

(2) Spring (March – May 2018)

- Mean temperatures: significantly above normal nation wide
- Precipitation amounts: above normal from northern to western Japan, especially on the Sea of Japan side of northern and eastern Japan, significantly below normal in Okinawa/Amami
- Sunshine durations: significantly above normal on the Pacific side of eastern Japan and in western Japan and Okinawa/Amami, above normal on the Sea of Japan side of eastern Japan, near normal in northern Japan

Seasonal mean temperatures were significantly above normal nationwide as a result of warm air masses over Japan throughout the period. The value for eastern Japan was the highest since records began in 1946, at 2.0°C over the normal. Sunny conditions and high pressure prevailed from eastern Japan to Okinawa/Amami, while northern to western parts of Japan experienced heavy rain in association with the passage of low-pressure areas containing moist air from the south. Seasonal sunshine durations were significantly above normal on the Pacific side of eastern Japan, in western Japan and in Okinawa/Amami. Seasonal precipitation amounts were significantly above normal on the Sea of Japan side of northern Japan and eastern parts of the country, and were significantly below normal in Okinawa/ Amami.

(3) Summer (June – August 2018)

- Mean temperatures: significant above normal in eastern and western Japan, above normal in northern Japan, near normal in Okinawa/Amami
- Precipitation amounts: significantly above normal on the Sea of Japan side of northern Japan, on the Pacific side of western Japan, and in Okinawa/Amami, above normal on the Pacific side of northern Japan, near normal in eastern Japan and on the Sea of Japan side of western Japan
- Sunshine durations: below normal on the Sea of Japan side of northern Japan and in Okinawa/Amami, significantly above normal in eastern Japan and on the Sea of Japan side of western Japan, near normal on the Pacific side of northern Japan

In early July, several days of record rainfall were observed in western Japan due to the influence of an active Baiu front, causing serious damage including landslides and floods. From mid-July onward, very hot conditions continued in eastern and western Japan due to the presence of a pronounced Subtropical High and Tibetan High over the country. The rainy Baiu season ended significantly earlier than usual in many regions, and very hot conditions continued in eastern and western Japan. On July 23, Japan's all-time high temperature of 41.1°C was recorded at Kumagaya in Saitama Prefecture. The seasonal mean temperature in eastern Japan was the highest for summer since 1946, at 1.7°C above the normal. At 48 of the country's 153 meteorological stations, the seasonal mean temperature for summer was highest or joint-highest on record. Seasonal precipitation amounts were significantly above normal on the Sea of Japan side of northern Japan and from eastern Japan to Okinawa/Amami due to the influence of stationary fronts or typhoons. In Okinawa/Amami, seasonal precipitation amounts were the highest since 1946.

(4) Autumn (September – November 2018)

- Mean temperatures: above normal in eastern and western Japan, near normal in northern and Japan and Okinawa/Amami
- Precipitation amounts: above normal from eastern Japan to Okinawa/Amami, below normal in northern Japan
- Sunshine durations: below normal in eastern Japan and on the Sea of Japan side of western Japan, above normal in northern Japan and Okinawa /Amami, near normal on the Pacific side of western Japan

Seasonal mean temperatures were above normal in northern and eastern Japan because stronger-than-normal high-pressure areas to the east of the country hindered the flow of northerly cold air over these regions. Seasonal precipitation amounts were above normal from eastern Japan to Okinawa/Amami due to the influence of an active stationary front and typhoon activity. In early September, the strong Typhoon Jebi made landfall on the southern part of Tokushima before heading north to the Kinki region. In late September Typhoon Trami approached the Okinawa region and made landfall near Tanabe in Wakayama Prefecture before moving from western to northern Japan, bringing storms, heavy rain, storm surges and high waves to wide areas.

(5) Early Winter (December 2018)

Above-normal temperatures prevailed nationwide except in northern Japan. However, heavy snowfall and snowstorms were observed on the Sea of Japan side of the country in late December due to a strong winter monsoon.

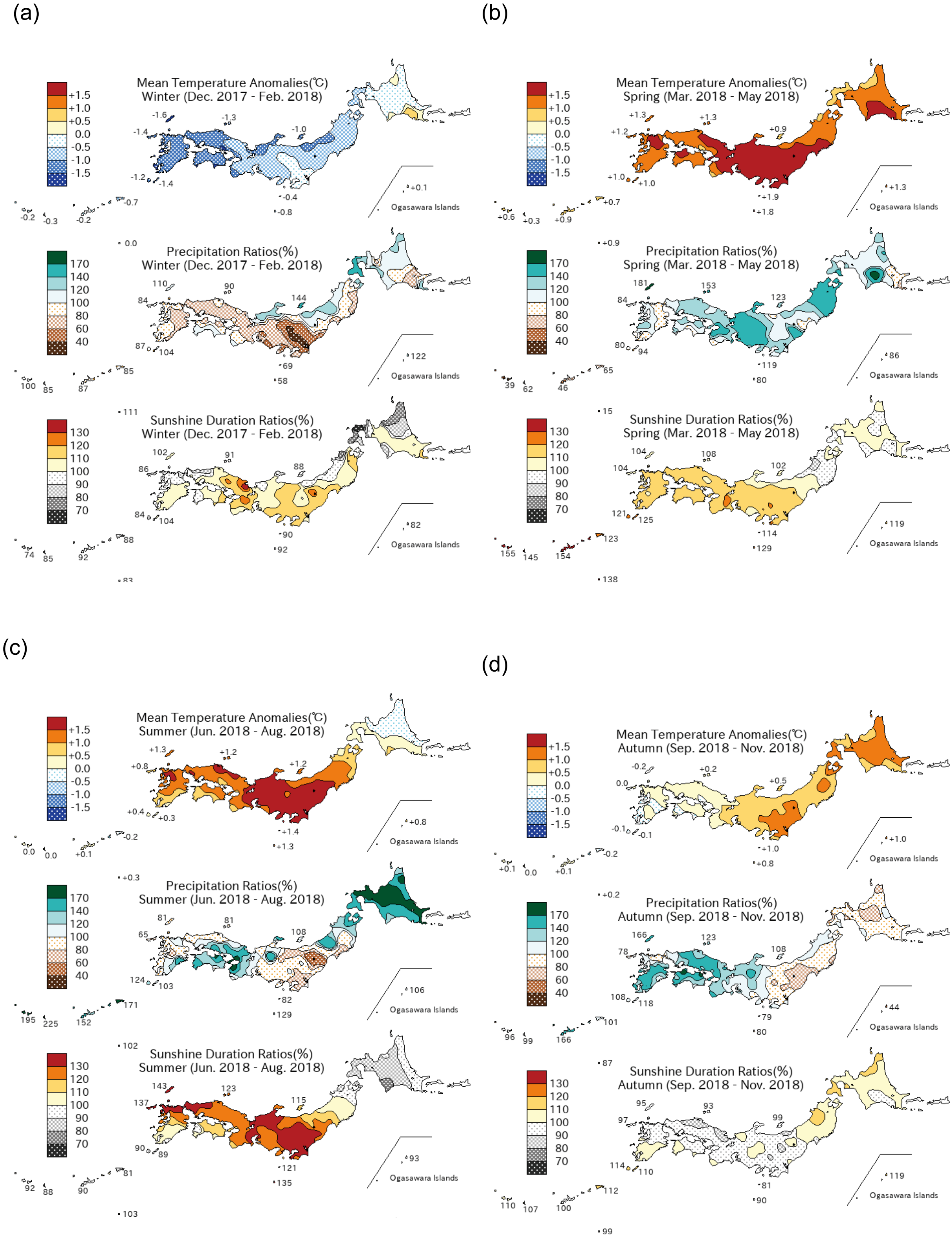

Figure 1.2-3 Seasonal anomalies/ratios for Japan in 2018
(a) Winter (December 2017 to February 2018), (b) spring (March to May 2018), (c) summer (June to August 2018), (d) autumn (September to November 2018). The base period for the normal is 1981 – 2010.

Table 1.2-1 Number of observatories reporting record(include tie record) monthly and annual mean temperatures, precipitation amounts and sunshine durations (2018)

From 153 surface meteorological stations across Japan.

	Temperature		Precipitation amount		Sunshine duration	
	Highest	Lowest	Heaviest	Lightest	Longest	Shortest
January						
February				4	3	
March	60		9		29	
April	21			2	2	
May	1		1	1	1	
June			1	4	2	
July	53		1		5	1
August	12		2	2	1	
September	1		7	6		
October	4					4
November				6	4	
December	1		1	1		6
year	29		2		4	

1.3 Atmospheric circulation and oceanographic conditions[6]

- In winter 2017/2018, tropical convection was enhanced from the Indochina Peninsula to seas east of the Philippines due to La Niña conditions. The subtropical and subpolar jet stream meandered southward over Japan, resulting in strong cold-air-mass flow over the country.
- In summer 2018, as a result of enhanced convection over and around the Philippines as well as the significant northward meandering of the subtropical jet stream in the vicinity of Japan, the expansion of both the North Pacific Subtropical High and the Tibetan High to mainland Japan was stronger than normal. The record heatwave observed in eastern and western Japan is attributed to these conditions.

Monitoring of atmospheric and oceanographic conditions (e.g., upper air flow, tropical convective activity, sea surface temperatures (SSTs) and the Asian monsoon) is key to understanding the causes of extreme weather events[7]. This section briefly outlines the characteristics of atmospheric circulation and oceanographic conditions seen in 2018.

1.3.1 Characteristics of individual seasons[8]

(1) Winter (December 2017 – February 2018)

La Niña conditions continued in the equatorial Pacific from autumn 2017 onward (see Section 2.6.1), with positive SST anomalies in the western part and negative values from central to eastern parts (Figure 1.3-1 (a)). Tropical convection activity was enhanced from the Indochina Peninsula to seas east of the Philippines, and was suppressed from west of the dateline to the central part of the equatorial Pacific (Figure 1.3-1 (b)). In the lower troposphere of the tropical region, cyclonic circulation anomalies straddling the equator were seen from the Indian Ocean to the Maritime Continent (Figure 1.3-1 (c)).

Positive anomalies in the 500-hPa height field were seen in and around the North Pole, and negative height anomalies were seen over Europe. The polar vortex split into East Siberian and North American parts, with respective wave trains clearly observed over southern and northern Eurasia (Figure 1.3-1 (d)). The sea level pressure (SLP) field indicates that the Siberian High was stronger than normal in general and extended northwestward, and that the Aleutian Low was shifted westward and stronger than normal over and around the Kamchatka Peninsula (Figure 1.3-1 (e)). Temperatures at 850 hPa were above normal over the Arctic Ocean and below normal over East Asia, the northern part of North America and Europe (Figure 1.3-1 (f)).

---

6 See the Glossary for terms relating to sea surface temperature variations, monsoon and Arctic Oscillation.

7 The main charts used for monitoring of atmospheric circulation and oceanographic conditions are: sea surface temperature (SST) maps representing SST distribution for monitoring of oceanographic variability elements such as El Niño/La Niña phenomena; outgoing longwave radiation (OLR) maps representing the strength of longwave radiation from the earth's surface under clear sky conditions into space or from the top of clouds under cloudy conditions into space for monitoring of convective activity; 850-hPa stream function maps representing air flow in the lower troposphere for monitoring of atmospheric circulation variability elements such as the Pacific High and the monsoon trough associated with the Asian summer monsoon; 500-hPa height maps representing air flow at a height of approximately 5,000 meters for monitoring of atmospheric circulation variability elements such as westerly jet streams and the Arctic Oscillation; sea level pressure maps representing air flow and pressure systems on the earth's surface for monitoring of the Pacific High, the Siberian High, the Arctic Oscillation and other phenomena; 850-hPa temperature maps representing air temperature at a height of approximately 1,500 meters; and temperature calculated from thickness in the troposphere for monitoring of mean temperature of the troposphere.

8 JMA publishes Monthly Highlights on the Climate System including information on the characteristics of climatic anomalies and extreme events around the world, atmospheric circulation and oceanographic conditions. It can be found at https://ds.data.jma.go.jp/tcc/tcc/products/clisys/highlights/index.html.

With enhanced convection over the Maritime Continent and southward expansion of the polar vortex to eastern Siberia, the subtropical and subpolar jet stream meandered southward over Japan, resulting in cold air-mass flow over the country. This is a possible cause of the tendency for the presence of cold air in areas near Japan.

(2) Spring (March – May 2018)
Ongoing remarkable positive SST anomalies in the western part of the equatorial Pacific and negative values from central to eastern parts were observed, despite the termination of the La Niña event in spring 2018. Remarkably positive SST anomalies were observed from the area east of the Philippines to the western coast of Central America in the tropical North Pacific, and remarkably negative SST anomalies were observed in the eastern part of the tropical South Pacific (Figure 1.3-2 (a)). Tropical convection was enhanced from Eastern Africa to the central Indian Ocean and from Micronesia to Hawaii, and was suppressed from the South China Sea to seas east of Japan and in the central-to-eastern equatorial Pacific (Figure 1.3-2 (b)). In the lower troposphere of the tropical region, anti-cyclonic circulation anomalies were seen over the central-to-eastern Pacific, and cyclonic circulation anomalies were seen over the east of the Philippines (Figure 1.3-2 (c)).

In the 500-hPa height field, wave trains were seen from the North Atlantic to northern Eurasia along the subpolar jet stream, with positive anomalies over northern Europe and the northeastern part of East Asia, and negative anomalies from western Russia to western Siberia (Figure 1.3-2 (d)). Positive SLP anomalies were seen over the central part of North America and northern Europe, and negative SLP anomalies were seen from the northeastern part of the North Atlantic to western Europe and Siberia. Positive SLP anomalies extended zonally over the mid-latitudes from Japan to the North Pacific, and the subtropical high was stronger than normal over the North Pacific and the North Atlantic (Figure 1.3-2 (e)). Temperatures at the 850-hPa level were above normal over the western USA, southern Europe and the mid-latitudes from East Asia to the North Pacific, and were below normal over the northeastern part of North America and from western Russia to western Siberia (Figure 1.3-2 (f)).

(3) Summer (June – August 2018)
SST anomalies were remarkably positive in the western part of the equatorial Pacific and remarkably negative in the Indian Ocean south of Java. The North Atlantic tripole pattern exhibited remarkably positive SST anomalies in the mid-latitudes and remarkably negative values south of Greenland and in the eastern part of the tropical region (Figure 1.3-3 (a)). Tropical convection was enhanced from the Philippines to the 10 – 20°N latitude band in the North Pacific, and was suppressed over the Indian Ocean and the central part of the South Pacific (Figure 1.3-3 (b)). In the lower troposphere over the tropical region, cyclonic circulation anomalies were seen from the northern part of the South China Sea to seas east of the Philippines, indicating a stronger-than-normal monsoon trough over Southeast Asia (Figure 1.3-3 (c)).

In the 500-hPa height field, the polar vortex in the Northern Hemisphere was shifted toward North America. Positive anomalies in the 500-hPa height field were generally distributed over the mid-latitudes, and were seen over the seas south of Alaska, the eastern part of North America, northern Europe, from Central to Eastern Siberia and over the northeastern part of East Asia. Negative anomalies in the 500-hPa height field were seen over the Mediterranean Sea and from the South China Sea to seas south of Japan (Figure 1.3-3 (d)). Negative SLP anomalies were seen in and around Greenland, and positive SLP anomalies were seen over the mid-latitudes of the North Pacific and the North Atlantic. The extension of the North Pacific Subtropical High (NPSH) toward mainland Japan was stronger than normal (Figure 1.3-3 (e)). Temperatures at 850 hPa were above normal over seas south of Alaska, the eastern part of North America, northern Europe, from Central to Eastern Siberia, and over the eastern part of East Asia, and below normal over northern Canada and the Sea of Okhotsk (Figure 1.3-3 (f)).

In summer, as the result of enhanced convective activity over and around the Philippines as well as the significant meandering of the subtropical jet stream in the vicinity of Japan, the expansion of both the NPSH and the Tibetan High to mainland Japan was stronger than normal. The record-breaking extreme heatwave in eastern and western Japan is attributed to these conditions (see Topics I).

(4) Autumn (September – November 2018)

Positive SST anomalies were observed over most of the equatorial Pacific, and remarkably positive anomalies were observed in western parts of the tropical region. El Niño conditions were considered present in autumn. In the Indian Ocean, remarkably negative SST anomalies were observed near the southwestern coast of Australia, and the North Atlantic SST anomaly tripole pattern remained following the anomaly observed in summer 2018 (Figures 1.3-3 (a) and 1.3-4 (a)). Tropical convection was enhanced over seas east of New Guinea, over the latitudinal bands of 10°N in central to eastern areas of the Pacific and from Western Africa to the Middle East, and was suppressed over the eastern Indian Ocean and from the South China Sea to seas east of the Philippines (Figure 1.3-4 (b)). In the lower troposphere of the tropical region, anticyclonic circulation anomalies straddling the equator were seen from the Indian Ocean to the Maritime Continent, and cyclonic circulation anomalies straddling the equator were seen over the Pacific (Figure 1.3-4 (c)).

Positive anomalies in the 500-hPa height field were clearly seen in and around Alaska and over northern Europe, and negative values were seen from central Canada to seas west of the UK and in and around China (Figure 1.3-4 (d)). Positive SLP anomalies were seen from northern Europe to Central Asia and from Alaska to Canada, and negative values were seen over Western Siberia (Figure 1.3-4 (e)). Temperatures at 850 hPa were above normal in and around Alaska and Europe, and below normal over the eastern part of North America (Figure 1.3-4 (f)).

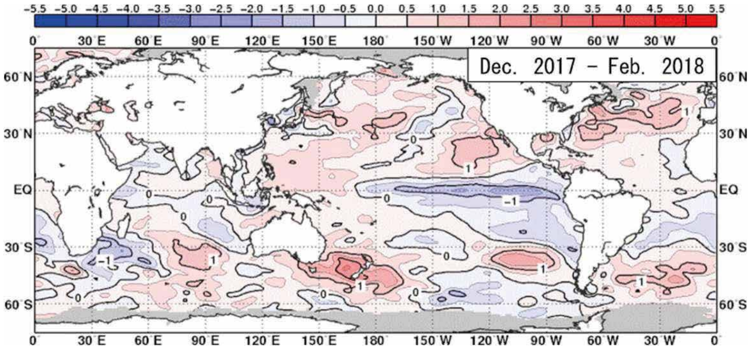

Figure 1.3-1 (a) Three-month mean sea surface temperature (SST) anomaly (December 2017 – February 2018)
The contour interval is 0.5°C. Sea ice coverage areas are shaded in gray. The base period for the normal is 1981 – 2010.

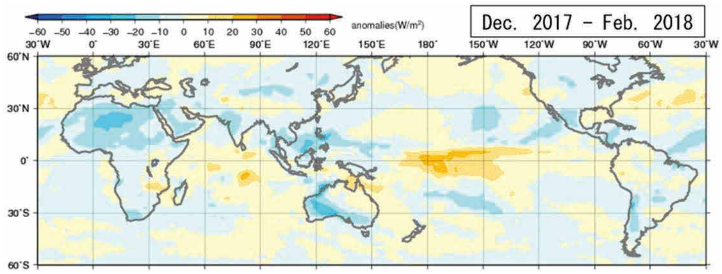

Figure 1.3-1 (b) Three-month mean outgoing longwave radiation (OLR) anomaly (December 2017 – February 2018)
The base period for the normal is 1981 – 2010. Negative (cold color) and positive (warm color) OLR anomalies show enhanced and suppressed convection, respectively, compared to the normal.

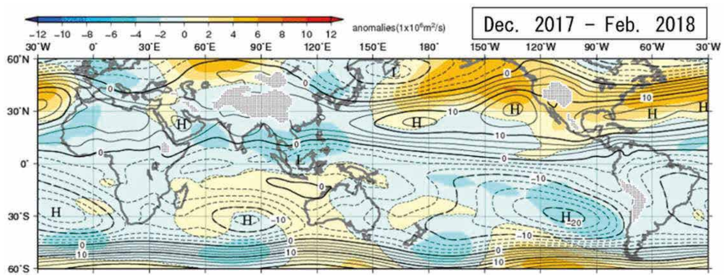

Figure 1.3-1 (c) Three-month mean 850-hPa stream function and anomaly (December 2017 – February 2018)
The contour interval is 2.5 x 10^6 m^2 per s. The base period for the normal is 1981 – 2010. “H” and “L” denote high- and low-pressure systems, respectively.

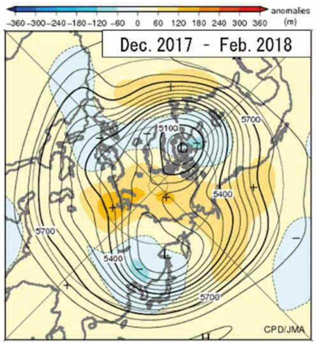

Figure 1.3-1 (d) Three-month mean 500-hPa height and anomaly in the Northern Hemisphere (December 2017 – February 2018)
Contours show 500-hPa height at intervals of 60 m, and shading indicates height anomalies. The base period for the normal is 1981 – 2010. “H” and “L” denote high- and low-pressure systems, respectively.

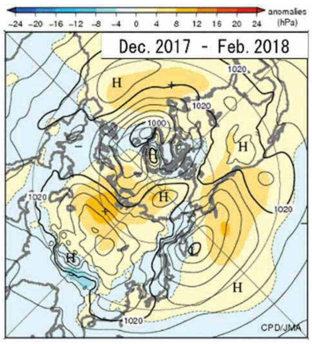

Figure 1.3-1 (e) Three-month mean sea level pressure and anomaly in the Northern Hemisphere (December 2017 – February 2018)
Contours show sea level pressure at intervals of 4 hPa, and shading indicates sea level pressure anomalies. The base period for the normal is 1981 – 2010. “H” and “L” denote high- and low-pressure systems, respectively.

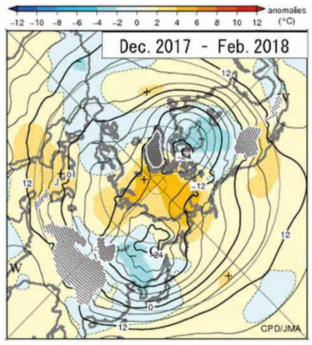

Figure 1.3-1 (f) Three-month mean 850-hPa temperature and anomaly in the Northern Hemisphere (December 2017 – February 2018)
Contours show temperature at intervals of 4 degree C, and shading indicates temperature anomalies. The base period for the normal is 1981 – 2010. “W” and “C” denote warm and cold conditions, respectively.

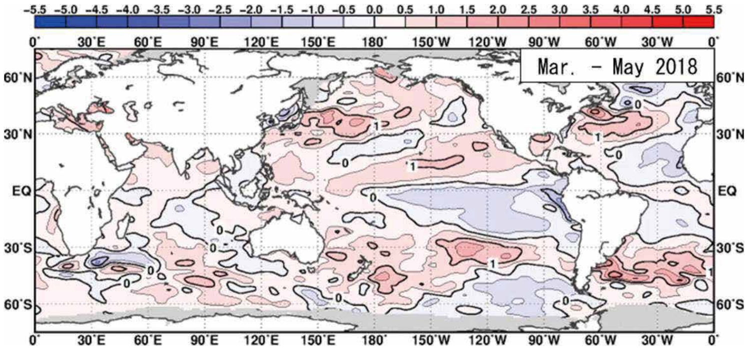

Figure 1.3-2 (a) Three-month mean sea surface temperature (SST) anomaly (March – May 2018)
As per Figure 1.3-1 (a), but for March – May 2018.

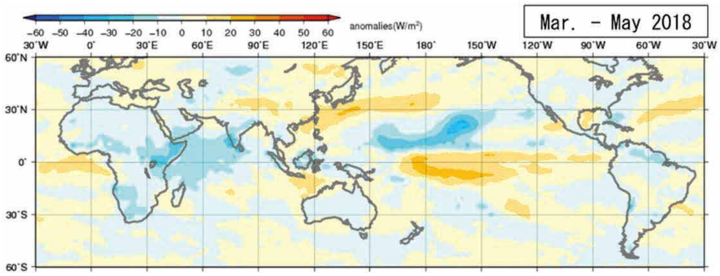

Figure 1.3-2 (b) Three-month mean outgoing longwave radiation (OLR) anomaly (March – May 2018)
As per Figure 1.3-1 (b), but for March – May 2018.

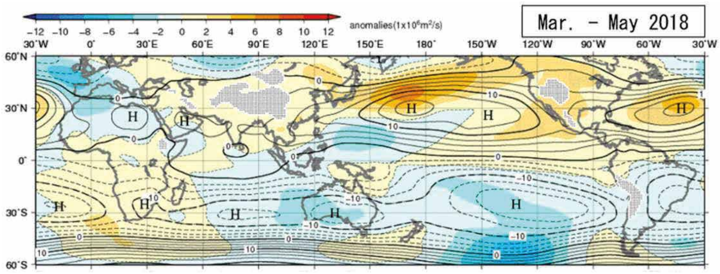

Figure 1.3-2 (c) Three-month mean 850-hPa stream function and anomaly (March – May 2018)
As per Figure 1.3-1 (c), but for March – May 2018.

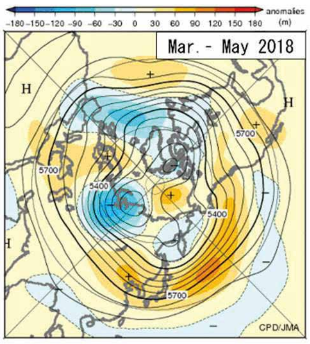

Figure 1.3-2 (d) Three-month mean 500-hPa height and anomaly in the Northern Hemisphere (March – May 2018)
As per Figure 1.3-1 (d), but for March – May 2018.

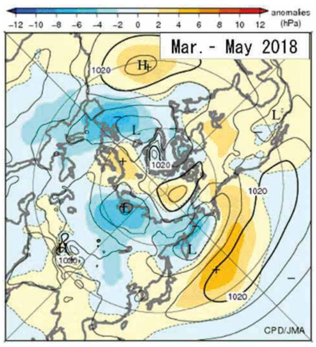

Figure 1.3-2 (e) Three-month mean sea level pressure and anomaly in the Northern Hemisphere (March – May 2018)
As per Figure 1.3-1 (e), but for March – May 2018.

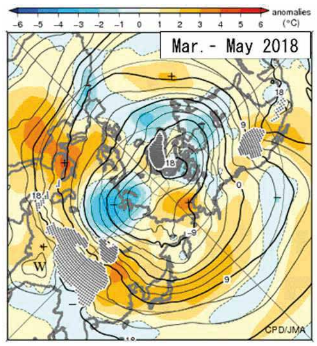

Figure 1.3-2 (f) Three-month mean 850-hPa temperature and anomaly in the Northern Hemisphere (March – May 2018)
As per Figure 1.3-1 (f), but for March – May 2018. Contour interval is 3 degree C.

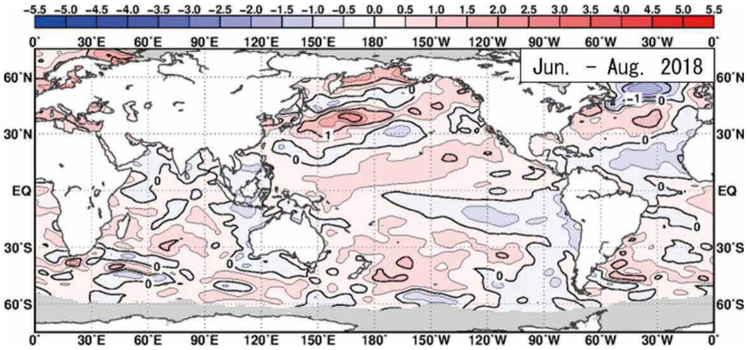

Figure 1.3-3 (a) Three-month mean sea surface temperature (SST) anomaly (June – August 2018)
As per Figure 1.3-1 (a), but for June – August 2018.

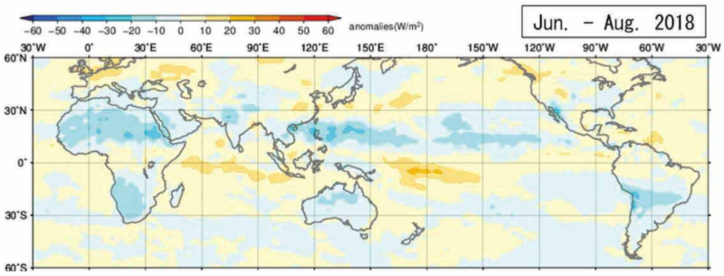

Figure 1.3-3 (b) Three-month mean outgoing longwave radiation (OLR) anomaly (June – August 2018)
As per Figure 1.3-1 (b), but for June – August 2018.

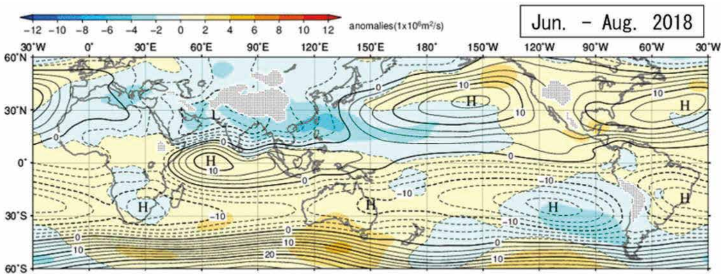

Figure 1.3-3 (c) Three-month mean 850-hPa stream function and anomaly (June – August 2018)
As per Figure 1.3-1 (c), but for June – August 2018.

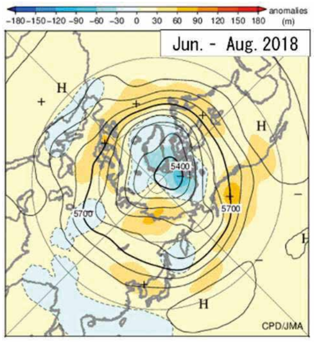

Figure 1.3-3 (d) Three-month mean 500-hPa height and anomaly in the Northern Hemisphere (June – August 2018)
As per Figure 1.3-1 (d), but for June – August 2018.

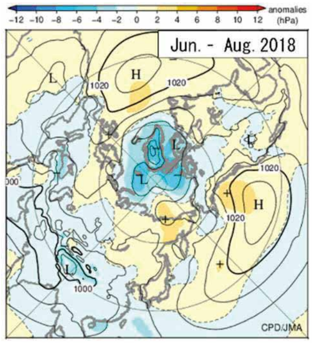

Figure 1.3-3 (e) Three-month mean sea level pressure and anomaly in the Northern Hemisphere (June – August 2018)
As per Figure 1.3-1 (e), but for June – August 2018.

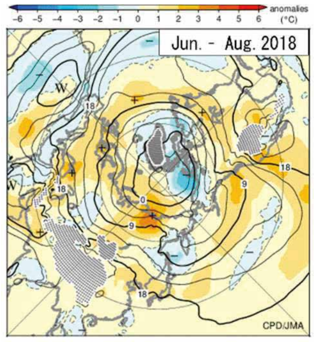

Figure 1.3-3 (f) Three-month mean 850-hPa temperature and anomaly in the Northern Hemisphere (June – August 2018)
As per Figure 1.3-1 (f), but for June – August 2018.
Contour interval is 3 degree C.

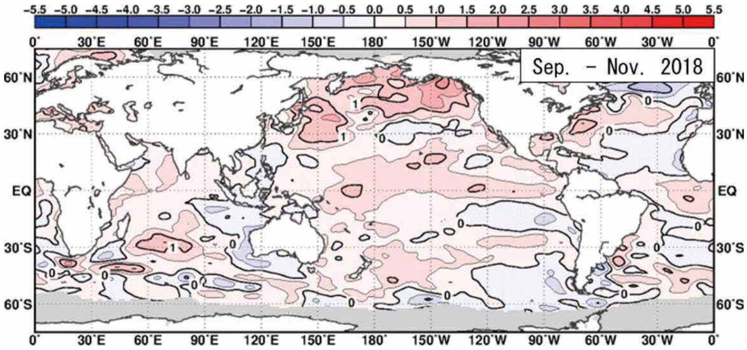

Figure 1.3-4 (a) Three-month mean sea surface temperature (SST) anomaly
(September – November 2018)
As per Figure 1.3-1 (a), but for September – November 2018.

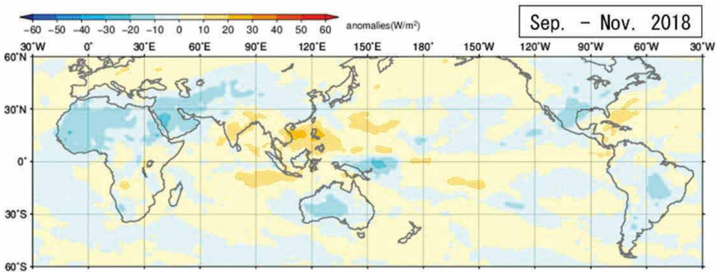

Figure 1.3-4 (b) Three-month mean outgoing longwave radiation (OLR) anomaly (September – November 2018)
As per Figure 1.3-1 (b), but for September – November 2018.

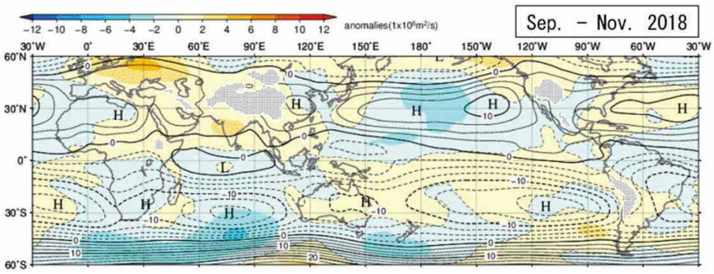

Figure 1.3-4 (c) Three-month mean 850-hPa stream function and anomaly (September – November 2018)
As per Figure 1.3-1 (c), but for September – November 2018.

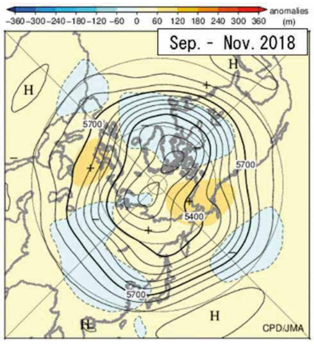

Figure 1.3-4 (d) Three-month mean 500-hPa height and anomaly in the Northern Hemisphere (September – November 2018)
As per Figure 1.3-1 (d), but for September – November 2018.

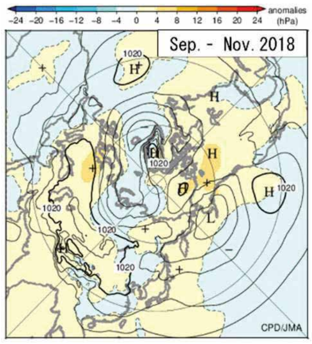

Figure 1.3-4 (e) Three-month mean sea level pressure and anomaly in the Northern Hemisphere (September – November 2018)
As per Figure 1.3-1 (e), but for September – November 2018.

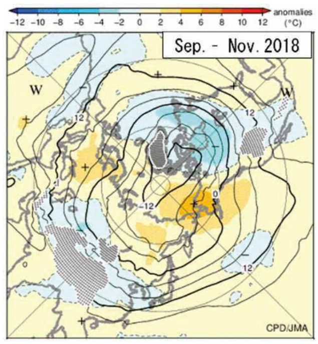

Figure 1.3-4 (f) Three-month mean 850-hPa temperature and anomaly in the Northern Hemisphere (September – November 2018)
As per Figure 1.3-1 (f), but for September – November 2018.

1.3.2 Global average temperature in the troposphere

The global average temperature in the troposphere peaked in spring 2016 and remained higher than normal until 2018 (Figure 1.3-5). Values over the mid-latitudes of the Northern Hemisphere showed a rising tendency from 2017 onward and peaked in summer 2018 (figure not shown). In July 2018, zonal mean temperatures in the troposphere were significantly above normal from 40 to 70°N (Figure 1.3-6). The significantly warm conditions observed are associated with the extreme heatwave seen worldwide around boreal summer (see Section 1.1).

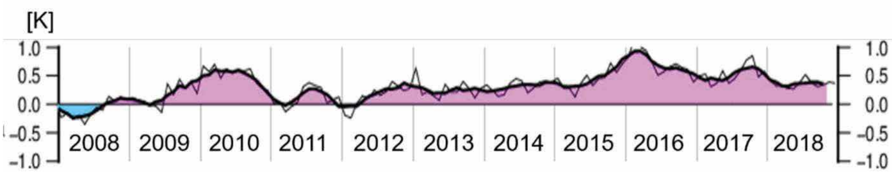

Figure 1.3-5 Time-series representation of global average temperature anomalies calculated from thickness in the troposphere (2008 to 2018)

The thin and thick lines show monthly mean and five-month running mean values, respectively. The base period for the normal is 1981 – 2010.

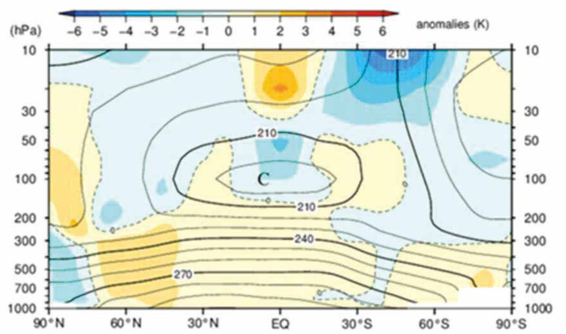

Figure 1.3-6 Latitude-height cross section of zonal mean temperature and anomaly (July 2018)

Contours show zonal mean temperature at intervals of 10 K, and shading indicates temperature anomalies. The base period for the normal is 1981 – 2010. "W" and "C" denote warm and cold conditions, respectively.

1.3.3 Asian summer monsoon

Convection during the 2018 Asian summer monsoon season (i.e., June – September) was generally enhanced from June to August as indicated by the OLR index (SAMOI (A)[9], JMA, 1997; Figure 1.3-7), particularly over the Philippines in the first half of June and from mid-July to August, and an associated deep monsoon trough was observed. This enhancement around the Philippines was associated with the extreme summer heatwave in Japan (see Topics I). In connection with the deep monsoon trough, near-surface westerly winds in the western part of the tropical North Pacific were stronger than normal. These conditions may have contributed to the series of typhoon events observed over the northwestern Pacific.

9 SAMOI (A) is defined as reversed-sign area-averaged OLR anomalies normalized by its standard deviation. The area for average is enclosed by green line in the bottom of Figure 1.3-7.

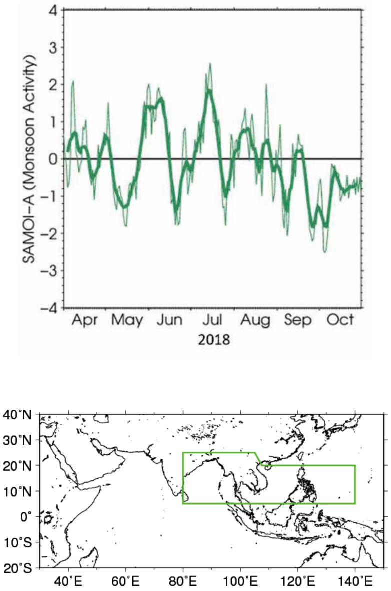

Figure 1.3-7 Time-series representation of the Asian summer monsoon OLR index (SAMOI (A)) (April – October 2018)

The thin and thick green lines indicate daily and seven-day running mean values, respectively. SAMOI (A) indicates the overall activity of the Asian summer monsoon, and positive and negative values indicate enhanced and suppressed convective activity, respectively, compared to the normal. The base period for the normal is 1981 – 2010.

1.3.4 Tropical cyclones over the western North Pacific and the South China Sea

In 2018, 29 tropical cyclones (TCs) with maximum wind speeds of ≥ 34 kt[10] formed over the western North Pacific and the South China Sea (Figure 1.3-8, Table 1.3-1), which was above the normal of 25.6 (1981 – 2010 average). A total of 9 TCs formed in August 2018 (against a normal of 5.9), which tied as the third highest on record for August since 1951 behind the totals of 10 for 1960 and 1966. In addition, 7 TCs reached peak intensity with maximum wind speeds of ≥ 105 kt, which was the highest since records began in 1977 (exceeding the previous high of 6 for 1983). A total of 16 TCs came within 300 km of the Japanese archipelago, which was above the normal of 11.4. A total of 5 made landfall on Japan, exceeding the normal of 2.7.

TC Jongdari formed east of the Philippines on 24 July (JST[11]) before moving northeastward south of the Ogasawara Islands and then westward near the Izu Islands, making landfall on the city of Ise in Mie Prefecture on 29 July (JST). This was the first TC to move westward across western Japan after making landfall since records began in 1951. TC Jebi formed around the Marshall Islands on 28 August (JST) and made landfall on the southern part of Tokushima Prefecture on 4 September (JST), making it the first TC since 1993 to make landfall on Japan with maximum wind speeds of ≥ 85 kt. Jebi brought unusually strong winds and storm surges, causing particular damage to the Shikoku and Kinki areas.

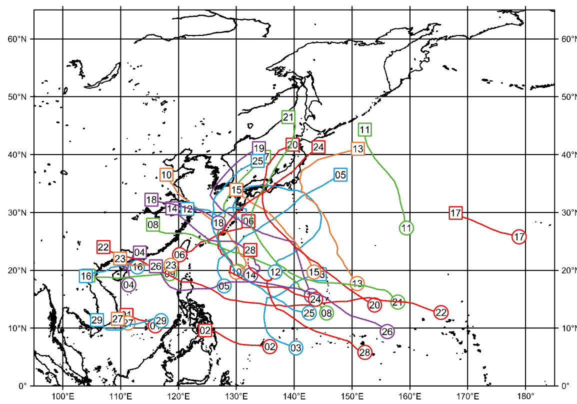

Figure 1.3-8 Tracks of TCs with maximum wind speeds of ≥ 34 kt in 2018

Numbered circles indicate positions of the TC formed (maximum wind speeds of ≥ 34 kt), and numbered squares indicate positions of the TC dissipated (maximum wind speeds lower than 34 kt). Source: RSMC Tokyo-Typhoon Center data

10 One knot (kt) is about 0.51 m/s.
11 Japan Standard Time (JST) is defined to set nine hours forward of UTC.

Table 1.3-1 TCs with maximum wind speeds of ≥ 34 kt in 2018 (Source: RSMC Tokyo-Typhoon Center data)

Number ID	Tropical Cyclone	Duration (UTC)	Maximum Wind[1)] (kt)	Number ID	Tropical Cyclone	Duration (UTC)	Maximum Wind[1)] (kt)
1801	BOLAVEN	1/3-1/4	35	1816	BEBINCA	8/13-8/17	45
1802	SANBA	2/11-2/13	35	1817	HECTOR	8/13-8/15	40
1803	JELAWAT	3/25-4/1	105	1818	RUMBIA	8/15-8/18	45
1804	EWINIAR	6/5-6/8	40	1819	SOULIK	8/16-8/24	85
1805	MALIKSI	6/7-6/11	60	1820	CIMARON	8/18-8/24	85
1806	GAEMI	6/15-6/17	45	1821	JEBI	8/27-9/5	105
1807	PRAPIROON	6/29-7/4	65	1822	MANGKHUT	9/7-9/17	110
1808	MARIA	7/4-7/11	105	1823	BARIJAT	9/11-9/13	40
1809	SON-TINH	7/17-7/19	40	1824	TRAMI	9/21-10/1	105
1810	AMPIL	7/18-7/23	50	1825	KONG-REY	9/29-10/6	115
1811	WUKONG	7/23-7/27	50	1826	YUTU	10/22-11/2	115
1812	JONGDARI	7/24-8/3[2)]	75	1827	TRAJI	11/17-11/18	35
1813	SHANSHAN	8/3-8/10	70	1828	MAN-YI	11/20-11/27[2)]	80
1814	YAGI	8/8-8/13	40	1829	USAGI	11/22-11/26	60
1815	LEEPI	8/11-8/15	50				

1) Estimated maximum 10-minute mean wind speed
2) The duration of Jongdari and Man-yi includes periods with maximum wind speeds intermittently lower than 34 kt.

Chapter 2 Climate Change

2.1 Changes in temperature[12]

- The annual anomaly of the global average surface temperature in 2018 was the 4th highest since 1891. On a longer time scale, it is virtually certain that the annual global average surface temperature has risen at rates of 0.73ºC per century.
- The annual anomaly of the average temperature over Japan was the 6th highest since 1898. On a longer time scale, it is virtually certain that the annual average temperature over Japan has risen at rates of 1.21ºC per century.
- It is virtually certain that the annual number of days with maximum temperatures of 35 ºC or higher ($T_{max} \geq 35$ºC) and that with minimum temperatures of 25ºC or higher ($T_{min} \geq 25$ºC) have increased, while the annual number of days with minimum temperatures below 0ºC ($T_{min} < 0$ºC) has decreased.

2.1.1 Global surface temperature

The annual anomaly of the global average surface temperature in 2018 (i.e., the combined average of the near-surface air temperature over land and the SST) was +0.31ºC above the 1981 – 2010 average. This was the 4th highest since 1891. The global average temperature fluctuates on different time scales ranging from years to decades. On a longer time scale, it is virtually certain that the global average surface temperature has risen at a rate of 0.73ºC per century[13] (statistically significant at a confidence level of 99%[14]).

The surface temperature anomalies over the Northern Hemisphere and the Southern Hemisphere were +0.41ºC (the 4th highest) and +0.20ºC (the 4th highest) above the 1981 – 2010 average, respectively (Figure 2.1-1). It is virtually certain that average surface temperatures over the Northern Hemisphere and the Southern Hemisphere have risen at rates of 0.79 and 0.69ºC per century, respectively (both statistically significant at a confidence level of 99%).

Linear temperature trends for 5° × 5° latitude/longitude grid boxes indicate that most areas of the world, especially in the high latitudes of the Northern Hemisphere, have experienced long-term warming (Figure 2.1-2). These long-term trends in annual average temperatures can be largely attributed to global warming caused by increased concentrations of greenhouse gases such as CO_2. On a shorter time scale, temperatures fluctuate due to the influence of natural climate dynamics over different time scales ranging from years to decades.

---

12 Monthly, seasonal and annual estimates of average temperatures around the globe and around Japan are published on JMA's website.
https://www.data.jma.go.jp/cpdinfo/temp/index.html (Japanese)
https://ds.data.jma.go.jp/tcc/tcc/products/gwp/gwp.html (English)

13 According to IPCC AR5, the global average surface temperature has risen about 0.85°C (The 90% uncertainty interval is 0.65 to 1.06°C) over the period 1880 to 2012. The values given in IPCC AR5 and those in this report are considered to show no remarkable difference that have risen on a longer time scale and are higher since the mid-1990s, although they do not correspond exactly because of differences in dataset calculation methods and the statistical period examined.

14 For evaluation and clarification of the significance statistics used here, see "Explanatory note on detection of statistical significance in long-term trends" at the end of the report.

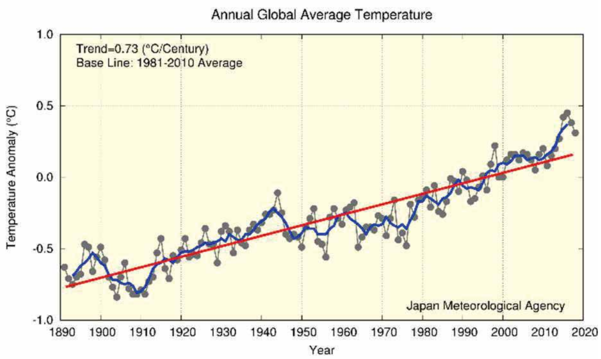

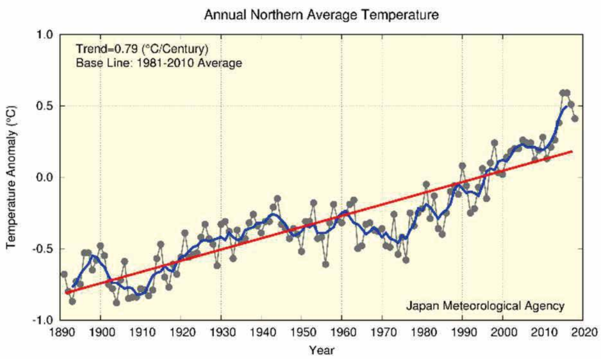

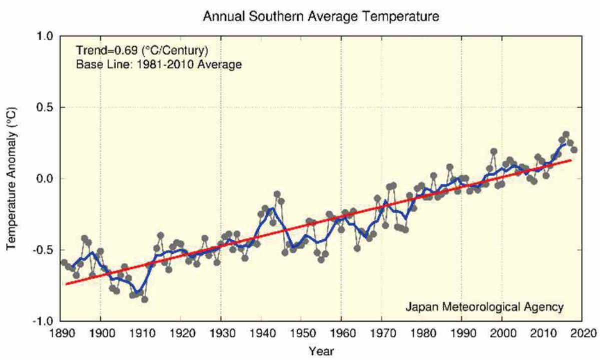

Figure 2.1-1 Annual anomalies in surface temperature (i.e., the combined average of the near-surface air temperature over land and the SST) from 1891 to 2018 for the globe (top left), for the Northern Hemisphere (top right) and for the Southern Hemisphere (bottom).

Anomalies are deviations from the baseline (i.e., the 1981 – 2010 average). The thin black line with dots indicates surface temperature anomalies for each year. The blue line indicates the five-year running mean, and the red line indicates the long-term linear trend.

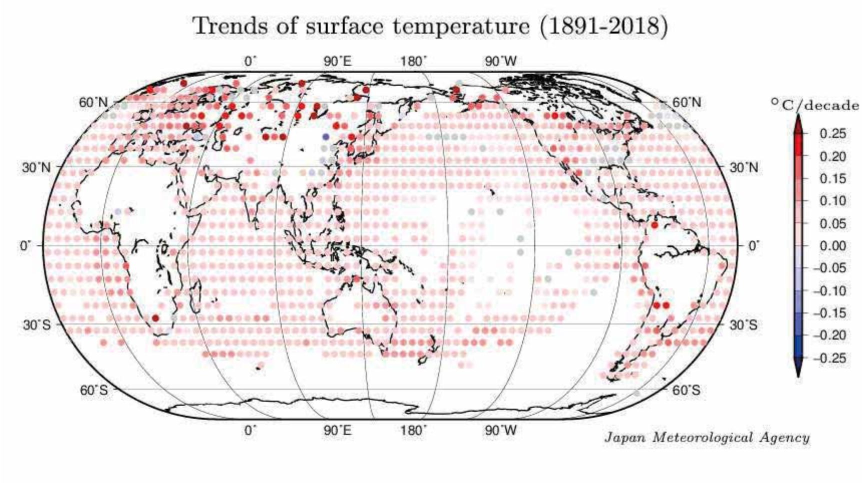

Figure 2.1-2 Linear temperature trends for 5° × 5° latitude/longitude grid boxes for the period of 1891 to 2018

The grid boxes with gray circles have no statistically significant trend (not statistically significant at a confidence level of 90%). Blank areas indicate those with insufficient data to analyze long-term trends.

2.1.2 Surface temperature over Japan

Long-term changes in the surface temperature over Japan are analyzed using observational records dating back to 1898. Table 2.1-1 lists the meteorological stations whose data are used to derive annual mean surface temperatures.

Table 2.1-1 Observation stations whose data are used to calculate surface temperature anomalies over Japan

Miyazaki and Iida were relocated in May 2000 and May 2002, respectively, and their temperatures have been adjusted to eliminate the influence of the relocation.

Element	Observation stations
Temperature (15 stations)	Abashiri, Nemuro, Suttsu, Yamagata, Ishinomaki, Fushiki, Iida, Choshi, Sakai, Hamada, Hikone, Tadotsu, Miyazaki, Naze, Ishigakijima

The mean surface temperature in Japan for 2018 is estimated to have been 0.68ºC above the 1981 – 2010 average, which is the 6th highest since 1898 (Figure 2.1-3). The surface temperature fluctuates on different time scales ranging from years to decades. On a longer time scale, it is virtually certain that the annual mean surface temperature over Japan has risen at a rate of 1.21ºC per century (statistically significant at a confidence level of 99%). Similarly, it is virtually certain that the seasonal mean temperatures for winter, spring, summer and autumn have risen at rates of about 1.10, 1.45, 1.11 and 1.20ºC per century, respectively (all statistically significant at a confidence level of 99%).

It is noticeable from Figure 2.1-3 that the annual mean temperature remained relatively low before the 1940s, started to rise and reached a local peak around 1960, entered a cooler era through to the mid-1980s and then began to show a rapid warming trend in the late 1980s. The warmest years on record have all been observed since the 1990s.

The high temperatures seen in recent years have been influenced by fluctuations over different time scales ranging from years to decades, as well as by global warming resulting from increased concentrations of greenhouse gases such as CO_2.

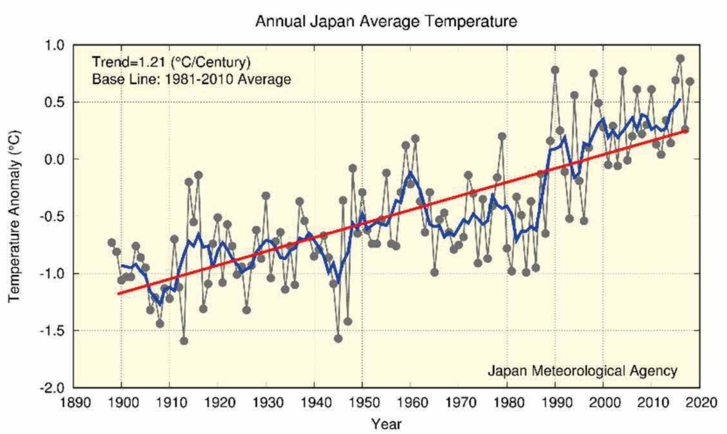

Figure 2.1-3 Annual surface temperature anomalies from 1898 to 2018 in Japan.
Anomalies are deviations from the baseline (i.e., the 1981 – 2010 average). The thin black line indicates the surface temperature anomaly for each year. The blue line indicates the five-year running mean, and the red line indicates the long-term linear trend.

2.1.3 Long-term trends of extreme temperature events[15] in Japan

This section describes long-term trends of extremely high/low-temperature events in Japan, as derived from analysis of temperature records from the 15 observation stations. Though monthly mean temperatures of the stations in Miyazaki and Iida have been adjusted to eliminate the influence of their relocation, records from these two stations are not used for analysis of daily temperatures due to the difficulty of adjustment in regard to the relocation.

(1) Long-term trends of monthly extreme temperatures

It is virtually certain that the frequency of extremely high monthly temperatures has increased, while that of extremely low monthly temperatures has decreased (both statistically significant at the confidence level of 99%) (Figure 2.1-4). The frequency of extremely high monthly temperatures has largely increased since about 1990.

15 Here, judgment of extremely high/low temperatures is based on the fourth-highest/lowest monthly values on records over the 118-year period from 1901 to 2018. The frequency of occurrence of the highest/lowest to the fourth-highest/lowest values over this period is once approximately every 30 years, which is close to JMA's definition of extreme climate events as those occurring once every 30 years or longer (See the Glossary for terms relating to Extreme climate event).

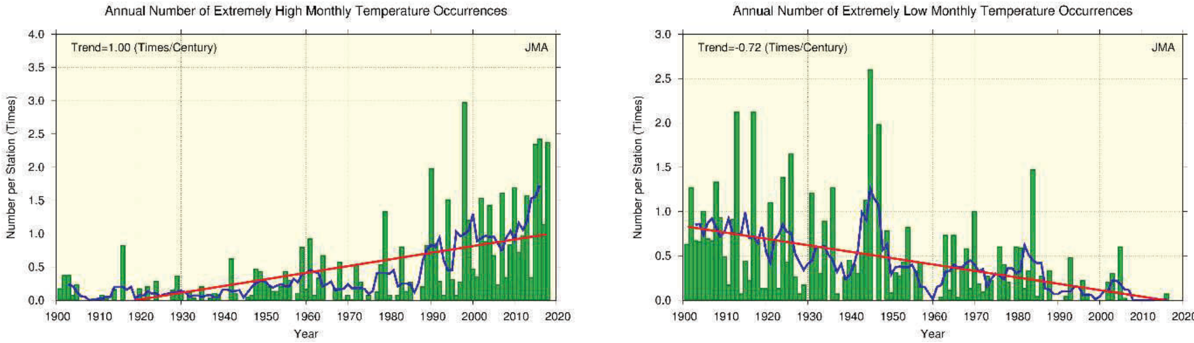

Figure 2.1-4 Annual number of extremely high/low monthly mean temperature occurrences from 1901 to 2018
The graphs show the annual number of occurrences of the highest/lowest first-to-forth values for each month during the period from 1901 to 2018. The green bars indicate annual occurrences of extremely high/low monthly mean temperatures divided by the total number of monthly observation data sets available for the year (i.e., the average occurrence per station). The blue line indicates the five-year running mean, and the straight red line indicates the long-term linear trend.

(2) Annual number of days with maximum temperatures of ≥ 30°C and ≥ 35°C

The annual number of days with maximum temperatures (T_{max}) of ≥ 30°C and T_{max} ≥ 35°C is virtually certain to have increased (both statistically significant at a confidence level of 99%) (Figure 2.1-5). Especially, the annual number of days with T_{max} ≥ 35°C has largely increased since about mid-1990s.

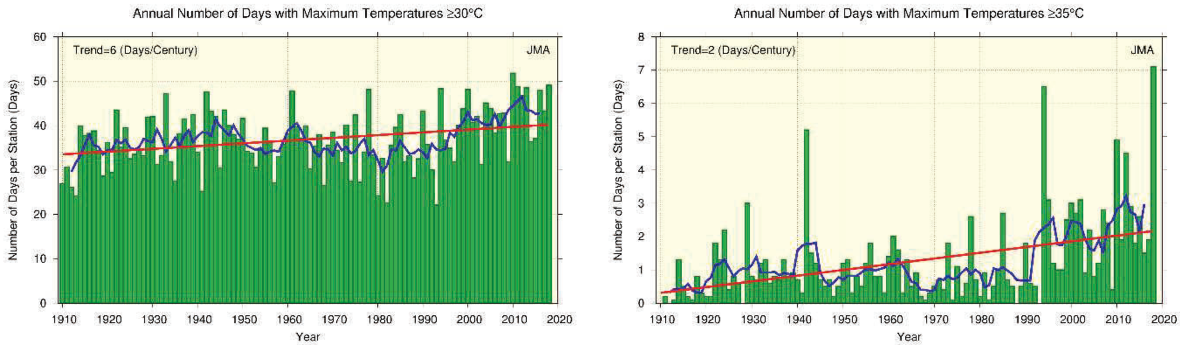

Figure 2.1-5 Annual number of days with maximum temperatures of ≥ 30°C and ≥ 35°C from 1910 to 2018
The green bars indicate the annual number of days per station for each year. The blue line indicates the five-year running mean, and the straight red line indicates the long-term linear trend.

(3) Annual number of days with minimum temperatures of < 0°C and ≥ 25°C

It is virtually certain that the annual number of days with minimum temperatures (T_{min}) of < 0°C has decreased, while the annual number of days with T_{min} ≥ 25°C has increased (both statistically significant at a confidence level of 99%) (Figure 2.1-6).

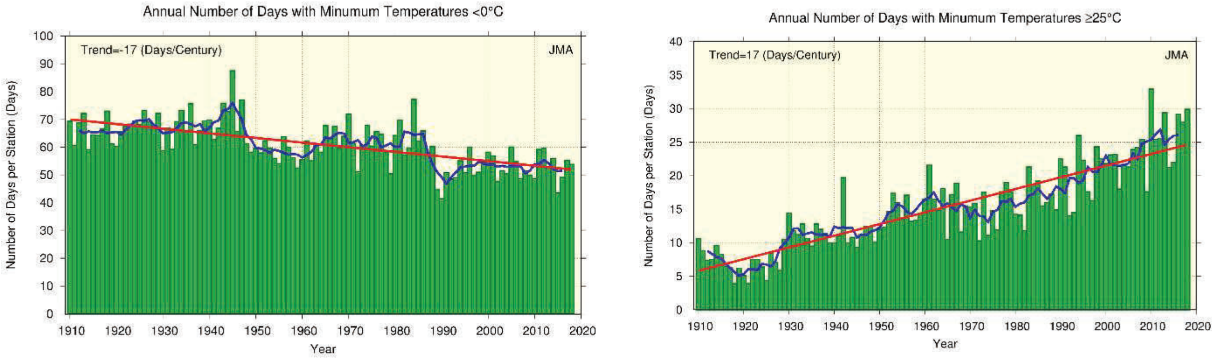

Figure 2.1-6 Annual number of days with minimum temperatures of <0°C and ≥ 25°C from 1910 to 2018
As per Figure 2.1-5.

2.1.4 Urban heat island effect at urban stations in Japan

The long-term trends of annual average temperatures are more pronounced for urban observation stations whose data are homogeneous over a long period (Sapporo, Sendai, Niigata, Tokyo, Yokohama, Nagoya, Kyoto, Osaka, Hiroshima, Fukuoka, Kagoshima) than for the average of the 15 rural observation stations (Table 2.1-2 and Figure 2.1-7).

Table 2.1-2 Long-term trends of annual and seasonal average temperatures at urban stations in Japan
These figures are based on data from 1927 to 2018. The trend of the 15 rural station averages (Table 2.1-1) is also listed. Values shown in italics are not statistically significant at a confidence level of 90%. For stations with asterisks (5 urban stations, and Iida and Miyazaki among the 15 rural stations), trends are calculated after adjustment to eliminate the influence of relocation.

Station	Long-term temperature trend (°C/century)														
	Average					Daily maximum					Daily minimum				
	Ann	Win	Spr	Sum	Aut	Ann	Win	Spr	Sum	Aut	Ann	Win	Spr	Sum	Aut
Sapporo	2.6	3.3	2.8	1.7	2.4	0.9	1.5	1.5	*0.5*	*0.4*	4.4	5.6	4.6	3.2	4.1
Sendai	2.4	2.9	2.8	1.4	2.4	1.2	1.6	1.7	0.9	0.9	3.1	3.6	3.8	2.0	3.2
Niigata*	2.0	2.2	2.6	1.4	1.8	1.9	2.6	2.7	0.8	1.6	2.2	2.3	2.7	1.8	1.8
Tokyo*	3.2	4.2	3.3	2.1	3.3	1.8	2.0	2.1	1.4	1.7	4.4	5.8	4.6	2.9	4.3
Yokohama	2.8	3.4	3.1	1.8	2.8	2.5	2.7	2.9	1.8	2.4	3.4	4.5	3.7	2.2	3.4
Nagoya	2.8	2.9	3.1	2.2	3.0	1.3	1.5	1.7	1.0	1.2	3.8	3.7	4.4	3.2	4.2
Kyoto	2.7	2.5	3.0	2.3	2.7	1.1	0.8	1.7	1.1	0.8	3.7	3.6	4.1	3.2	3.9
Osaka*	2.6	2.5	2.7	2.1	2.9	2.1	2.1	2.4	2.0	2.0	3.5	3.1	3.5	3.2	4.0
Hiroshima*	1.9	1.5	2.3	1.6	2.4	0.9	*0.6*	1.6	1.2	*0.4*	3.1	2.7	3.3	2.6	3.8
Fukuoka	3.0	2.8	3.4	2.2	3.7	1.7	1.6	2.1	1.4	1.6	4.9	4.2	5.8	3.7	6.0
Kagoshima*	2.5	2.4	2.8	2.0	2.8	1.2	1.1	1.6	1.1	1.3	3.9	3.5	4.4	3.3	4.6
15 stations*	1.5	1.5	1.9	1.1	1.4	1.1	1.1	1.6	0.8	0.8	1.8	1.8	2.1	1.6	1.8

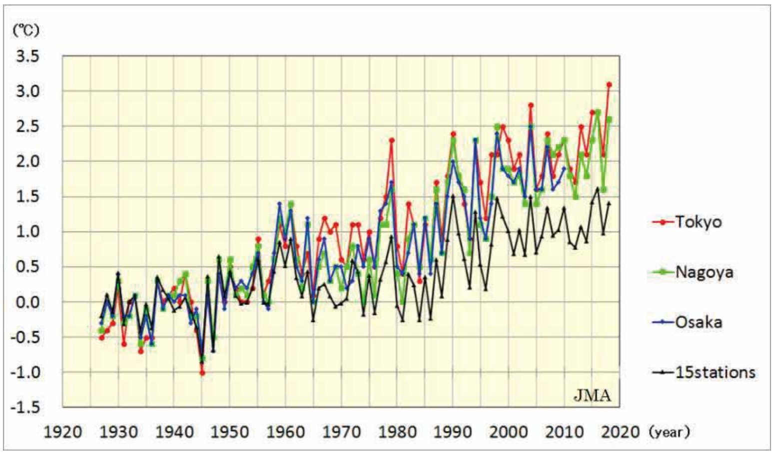

Figure 2.1-7 Annual temperature anomalies at Tokyo, Nagoya and Osaka and values averaged over 15 rural stations in Japan from 1927 to 2018

Anomalies are deviations from the baseline (i.e., the 1927 – 1956 average). Values averaged between 1927 and 1956 for respective stations all equal zero.

As it can be assumed that the long-term trends averaged over the 15 rural stations reflect large-scale climate change, the differences in the long-term trends of urban stations from the average of the 15 stations largely represent the influence of urbanization.

Detailed observation reveals that the long-term trends are more significant in winter, spring and autumn than in summer and more pronounced for minimum temperatures than for maximum temperatures at every urban observation station.

Records from urban stations whose data are not affected by relocation are used to determine long-term trends for the annual number of days with minimum temperatures of < 0°C and ≥ 25°C and maximum temperatures of ≥ 30°C and ≥ 35°C. The number of days with T_{min} < 0°C is very likely to have decreased with statistical significance at all urban stations, and the number with T_{min} ≥ 25°C, T_{max} ≥ 30°C and T_{max} ≥ 35°C is very likely to have increased with statistical significance at most stations except Sapporo (Table 2.1-3).

Table 2.1-3 Long-term trends for the annual number of days with minimum temperatures of < 0°C and ≥ 25°C and maximum temperatures of ≥ 30°C and ≥ 35°C.

These figures are based on data from 1927 to 2018. The trend of the 13 rural station averages (Table 2.1-1, excluding Iida and Miyazaki) is also listed. Values shown in italics are not statistically significant at a confidence level of 90%.

Station	Annual number of days			
	Trend (days/decade)			
	T_{min} < 0°C	T_{min} ≥ 25°C	T_{max} ≥ 30°C	T_{max} ≥ 35°C
Sapporo	−4.4	*0.0*	*0.1*	*0.0*
Sendai	−5.6	0.3	0.9	0.1
Yokohama	−6.0	3.0	2.2	0.2
Nagoya	−6.7	3.7	1.2	1.0
Kyoto	−7.1	3.6	1.3	1.3
Fukuoka	−4.9	4.7	1.1	1.1
13 Stations	−2.0	1.7	0.6	0.2

2.2 Changes in precipitation[16]

- The annual anomaly of global precipitation (for land areas only) in 2018 was +39 mm.
- The annual anomaly of precipitation in 2018 was +204.1 mm in Japan. Annual precipitation over Japan shows no discernible long-term trend.
- The annual number of days with daily and hourly extreme precipitation has increased in Japan, while that with wet days has decreased.
- Snow depth on the Sea of Japan side has decreased.

2.2.1 Global precipitation over land

Annual precipitation (for land areas only) in 2018 was +39 mm above the 1981 – 2010 average (Figure 2.2-1), and the figure has fluctuated periodically since 1901. In the Northern Hemisphere, records show large amounts of rainfall around 1930, in the 1950s and after the mid-2000s. Long-term trends are not analyzed because the necessary precipitation data for sea areas are not available.

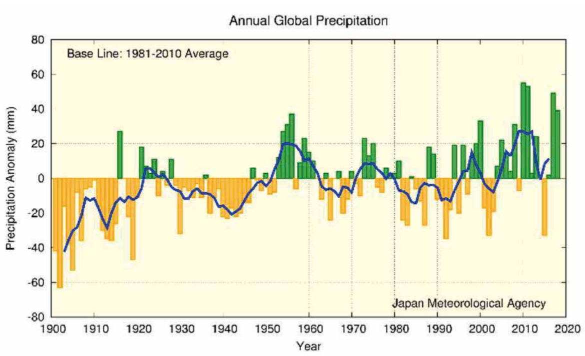

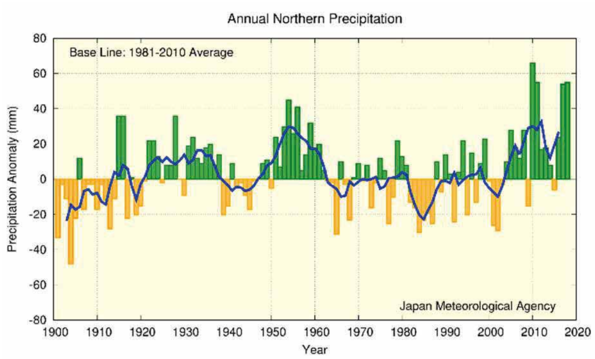

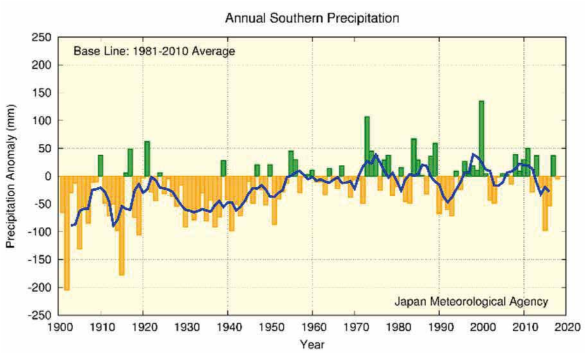

Figure 2.2-1 Annual anomalies in precipitation (over land areas only) from 1901 to 2018 for the globe (top left), for the Northern Hemisphere (top right) and for the Southern Hemisphere (bottom). Anomalies are deviations from the baseline (i.e., the 1981 – 2010 average).

The bars indicate the precipitation anomaly for each year, and the blue line indicates the five-year running mean.

2.2.2 Precipitation over Japan

This section describes long-term trends in precipitation over Japan as derived from analysis of precipitation records from 51 observation stations (Table 2.2-1).

Annual precipitation in 2018 was +204.1 mm above the 1981 – 2010 average. Japan experienced relatively large amounts of rainfall until the mid-1920s and around the 1950s. The annual figure exhibits greater variability for the period from the 1970s to the 2000s (Figure 2.2-2).

16 Data on annual precipitation around the world and in Japan are published on JMA's website.
https://www.data.jma.go.jp/cpdinfo/temp/index.html (Japanese)

Table 2.2-1 List of 51 observation stations whose data are used to calculate precipitation anomalies and long-term trends in Japan

Element	Observation stations
Precipitation (51 stations)	Asahikawa, Abashiri, Sapporo, Obihiro, Nemuro, Suttsu, Akita, Miyako, Yamagata, Ishinomaki, Fukushima, Fushiki, Nagano, Utsunomiya, Fukui, Takayama, Matsumoto, Maebashi, Kumagaya, Mito, Tsuruga, Gifu, Nagoya, Iida, Kofu, Tsu, Hamamatsu, Tokyo, Yokohama, Sakai, Hamada, Kyoto, Hikone, Shimonoseki, Kure, Kobe, Osaka, Wakayama, Fukuoka, Oita, Nagasaki, Kumamoto, Kagoshima, Miyazaki, Matsuyama, Tadotsu, Kochi, Tokushima, Naze, Ishigakijima, Naha

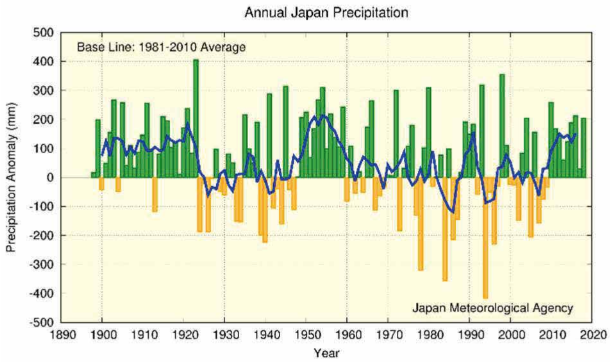

Figure 2.2-2 Annual anomalies in precipitation from 1898 to 2018 in Japan. Anomalies are deviations from the baseline (i.e., the 1981 – 2010 average).

The bars indicate the precipitation anomaly for each year, and the blue line indicates the five-year running mean.

2.2.3 Long-term trends of extreme precipitation events in Japan

This section describes long-term trends in frequencies of extremely wet/dry months and heavy daily precipitation events in Japan based on analysis of precipitation data from 51 observation stations.

(1) Extremely wet/dry months[17]

It is virtually certain that the frequency of extremely dry months increased during the period from 1901 to 2018 (statistically significant at a confidence level of 99%) (Figure 2.2-3 left). There has been no discernible trend in the frequency of extremely wet months (Figure 2.2-3 right).

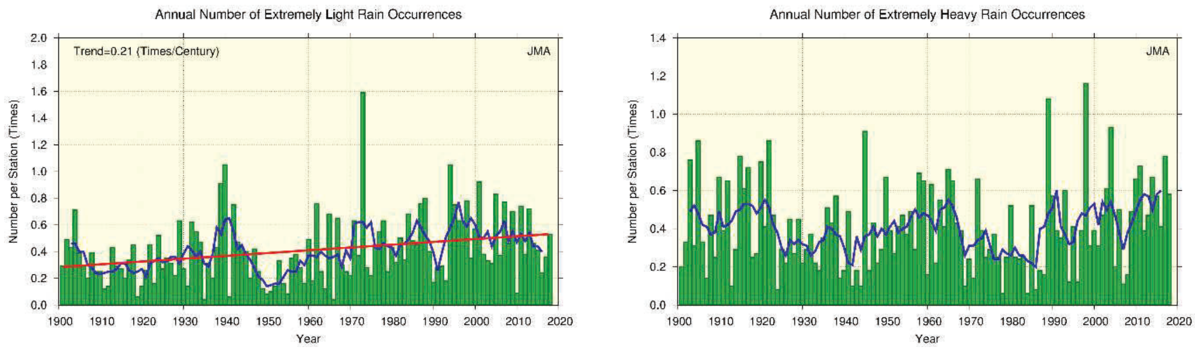

Figure 2.2-3 Annual number of extremely wet/dry months from 1901 to 2018

The graphs show the annual number of occurrences of the first-to-forth heaviest/lightest precipitation values for each month during the period from 1901 to 2018. The green bars indicate annual occurrences of extremely heavy/light monthly precipitation divided by the total number of monthly observation data sets available for the year (i.e., the average occurrence per station). The blue line indicates the five-year running mean, and the straight red line indicates the long-term liner trend.

17 Here, judgment of extremely heavy/light precipitation is based on the fourth–highest/lowest monthly values on record over the 118-year period from 1901 to 2018. The frequency of occurrence of the highest/lowest to the fourth–highest/lowest values over this period is once approximately every 30 years, which is close to JMA’s definition of extreme climate events as those occurring once every 30 years or longer (See the Glossary for terms relating to Extreme climate event).

(2) Annual number of days with precipitation of ≥ 100 mm, ≥ 200 mm and ≥ 1.0 mm

The annual number of days with precipitation of ≥ 100 mm and ≥ 200 mm are virtually certain to have increased (both statistically significant at a confidence level of 99%) during the period from 1901 to 2018 (Figure 2.2-4) . The annual number of days with precipitation of ≥ 1.0 mm (Figure 2.2-5) is virtually certain to have decreased over the same period (statistically significant at a confidence level of 99%). These results suggest decrease in the annual number of wet days including light precipitation and in contrast, an increase in extremely wet days.

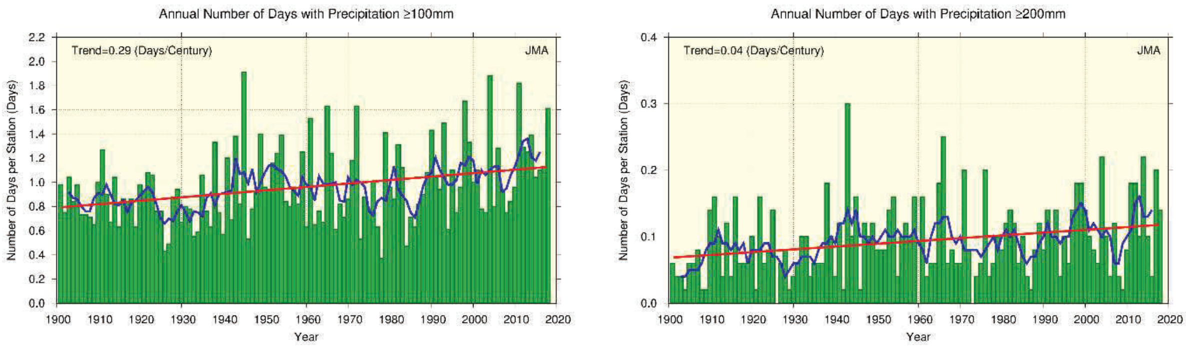

Figure 2.2-4 Annual number of days with precipitation ≥ 100 mm and ≥ 200 mm from 1901 to 2018
The green bars indicate the annual number of days per station for each year. The blue line indicates the five-year running mean, and the straight red line indicates the long-term liner trend.

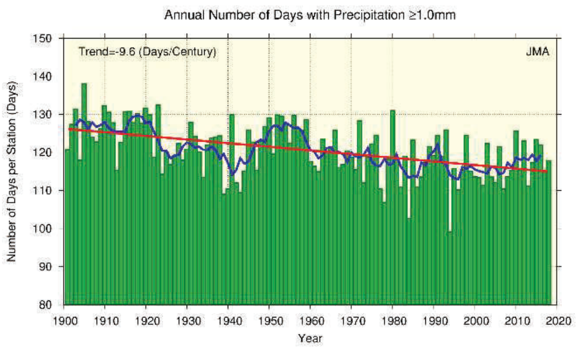

Figure 2.2-5 Annual number of days with precipitation of ≥ 1.0 mm from 1901 to 2018
As per figure 2.2-4.

2.2.4 Long-term trends of heavy rainfall analyzed using AMeDAS data

JMA operationally observes precipitation at about 1,300 unmanned regional meteorological observation stations all over Japan (collectively known as the Automated Meteorological Data Acquisition System, or AMeDAS). Observation was started in the latter part of the 1970s at many points, and observation data covering the approximately 40-year period through to 2018 are available[18]. Although the period covered by AMeDAS observation records is shorter than that of Local Meteorological Observatories or Weather Stations (which have observation records for the past 100 years or so), there are around eight times as many AMeDAS stations as Local Meteorological Observatories and Weather Stations combined. Hence, AMeDAS is better equipped to capture heavy precipitation events that take place on a limited spatial scale.

It is virtually certain that the annual numbers of events with precipitation of ≥ 50 mm and

18 The number of AMeDAS station was about 800 in 1976, and had gradually increased to about 1,300 in 2018. To account for these numerical differences, the annual number of precipitation events needs to be converted to a per-1,300-station basis. Data from wireless robot precipitation observation stations previously deployed in mountainous areas are also excluded.

≥ 80 mm per hour have increased (both statistically significant at a confidence level of 99%) (Figure 2.2-6). For the annual number of days with precipitation of ≥ 50 mm per hour, the number averaged for the last 10 years of the records (2009 – 2018) is about 311 on a per-1,300-station basis, which is about 1.4 times as many as that averaged for the first 10 years (1976 – 1985) of about 226.

The annual number of days with precipitation of ≥ 200 mm is very likely to have increased (statistically significant at a confidence level of 90%), and the corresponding figure for days with precipitation of ≥ 400 mm is extremely likely to have increased (statistically significant at a confidence level of 95%) (Figure 2.2-7).

As the annual number of extreme precipitation events is subject to large annual variations and the period covered by observation records is still relatively short, the addition of future observations to the data series is expected to increase the reliability of statistical trend detection.

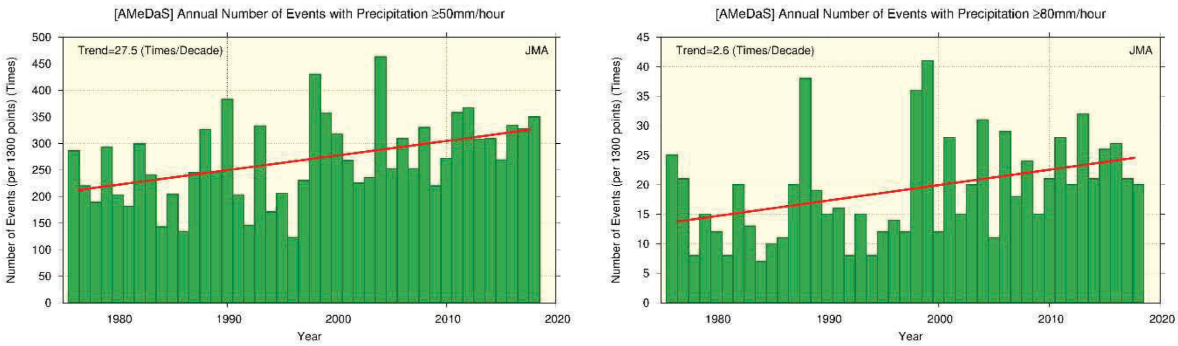

Figure 2.2-6 Annual number of events with precipitation of ≥ 50 mm and ≥ 80 mm per hour from 1976 to 2018
The green bars indicate the annual number of events per 1,300 AMeDAS stations for each year, and the straight red line indicates the long-term liner trend.

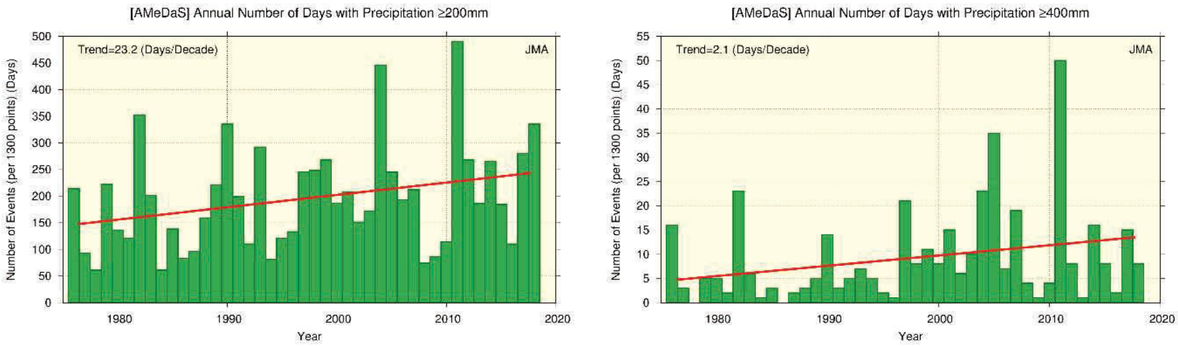

Figure 2.2-7 Annual number of days with precipitation of ≥ 200 mm and ≥ 400 mm from 1976 to 2018
The green bars indicate the annual number of days per 1,300 AMeDAS stations for each year, and the straight red line indicates the long-term liner trend.

2.2.5 Snow depth in Japan

Long-term trends in the annual maximum snow depth (represented in terms of a ratio against the 1981 – 2010 average) in Japan since 1962 are analyzed using observational records from stations located on the Sea of Japan coast (Table 2.2-2).

Table 2.2-2 Observation stations whose data are used to calculate snow depth ratios in Japan

Region	Observation stations
Sea of Japan side of northern Japan	Wakkanai, Rumoi, Asahikawa, Sapporo, Iwamizawa, Suttsu, Esashi, Kutchan, Wakamatsu, Aomori, Akita, Yamagata
Sea of Japan side of eastern Japan	Wajima, Aikawa, Niigata, Toyama, Takada, Fukui, Tsuruga
Sea of Japan side of western Japan	Saigo, Matsue, Yonago, Tottori, Toyooka, Hikone, Shimonoseki, Fukuoka, Oita, Nagasaki, Kumamoto

The annual maximum snow depth ratio in 2018 was 115% relative to the 1981 – 2010 average for the Sea of Japan side of northern Japan, 164% for the same side of eastern Japan, and 154% for the same side of western Japan (Figure 2.2-8). On a longer time scale, the annual maximum snow depth ratio from 1962 onward on the Sea of Japan side of northern Japan is very likely to have decreased at rates of 2.9% per decade (statistically significant at a confidence level of 90%), that on the Sea of Japan side of eastern Japan is extremely likely to have decreased at rates of 10.6% per decade (statistically significant at a confidence level of 95%), and that on the Sea of Japan side of western Japan is extremely likely to have decreased at rates of about 12.3% per decade (statistically significant at a confidence level of 95%). The annual maximum snow depth reached a local peak in the early 1980s followed by a sharp decline until around the early 1990s. The decline was particularly striking on the Sea of Japan side of eastern and western Japan.

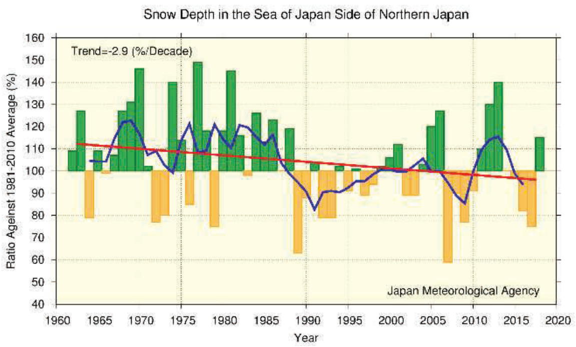

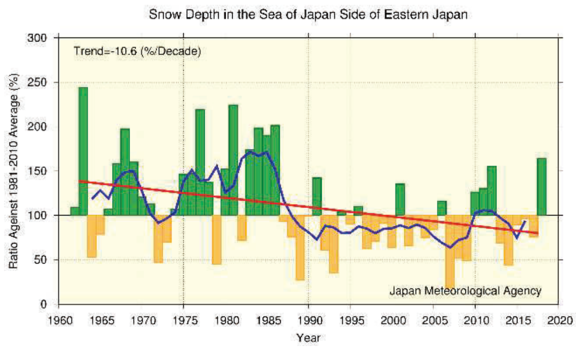

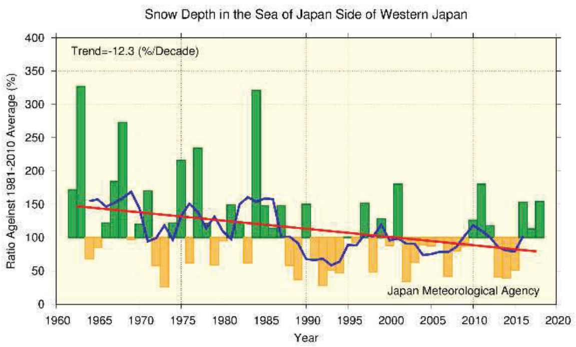

Figure 2.2-8 Annual maximum snow depth ratio from 1962 to 2018 on the Sea of Japan side for northern Japan (top left), eastern Japan (top right) and western Japan (bottom). Annual averages are presented as ratios against the baseline (i.e., the 1981 – 2010 average).
The bars indicate the snow depth ratio for each year. The blue line indicates the five-year running mean, and the red line indicates the long-term linear trend.

2.3 Changes in the phenology of cherry blossoms and acer leaves in Japan

- It is virtually certain that cherry blossoms have been flowering earlier.
- It is virtually certain that acer leaves have been changing color later.

JMA implements phenological observation to research the impact of meteorological condition on plants and animals, and eventually to monitor the progress of seasons as well as geographical variations and long-term changes in relation to the climate. Observation covers the first/full flowering and leaf color change of several plants and the first reported appearance/song of insects, birds and animals.

As part of its phenological monitoring, JMA observes cherry blossoms at 58 stations and acer leaves at 51 stations. Figure 2.3-1 shows interannual changes in the first reported dates of cherry blossom flowering and acer leaf color change between 1953 and 2018. The former exhibits a long-term advancing trend at a rate of 1.0 days per decade, while the latter shows a delaying trend at a rate of 2.8 days per decade (99% level of confidence for both cases). Table 2.3-1 compares climatological normals (based on 30-year averages) of the first reported date of cherry blossom flowering between 1961 – 1990 and 1981 – 2010 at stations in major Japanese cities. These phenomena are closely related to the surface mean temperature in the period before the event, and long-term warming is considered to be a major factor behind the trends observed.

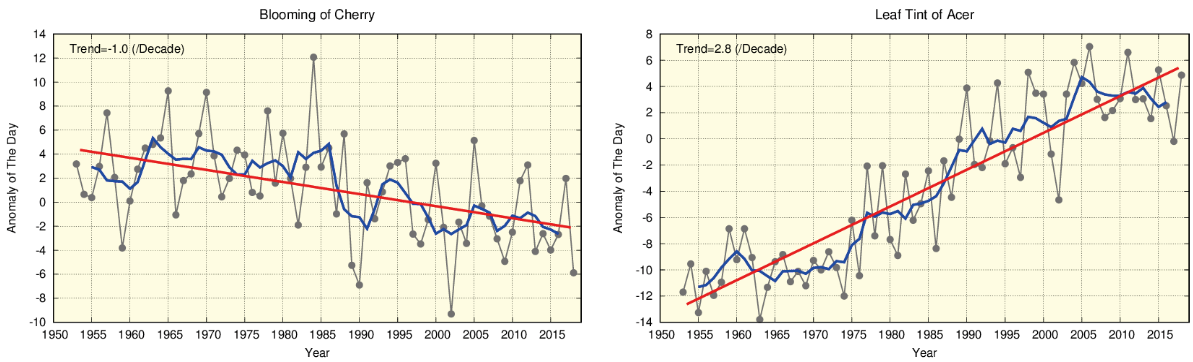

Figure 2.3-1 First reported dates of cherry blossom flowering (left) and acer leaf color change (right)
The black lines show annual anomalies of the first reported date averaged over all observation stations nationwide based on the normals for 1981 – 2010, and the blue lines indicate five-year running means. The red lines show the linear trend (cherry blossoms: −1.0 days per decade; acer leaves: +2.8 days per decade).

Table 2.3-1 Comparison of first reported dates of cherry blossom flowering
Differences in climatological normals for the first reported date of cherry blossom flowering between 1981 – 2010 and 1961 – 1990 at stations in major Japanese cities

Station	1961-1990 average	1981-2010 average	Difference (days)		1961-1990 average	1981-2010 average	Difference (days)
Kushiro	May 19	May 17	-2	Osaka	Apr 1	Mar 28	-4
Sapporo	May 5	May 3	-2	Hiroshima	Mar 31	Mar 27	-4
Aomori	Apr 27	Apr 24	-3	Takamatsu	Mar 31	Mar 28	-3
Sendai	Apr 14	Apr 11	-3	Fukuoka	Mar 28	Mar 23	-5
Niigata	Apr 13	Apr 9	-4	Kagoshima	Mar 27	Mar 26	-1
Tokyo	Mar 29	Mar 26	-3	Naha	Jan 16	Jan 18	+2
Nagoya	Mar 30	Mar 26	-4	Ishigakijima	Jan 15	Jan 16	+1

2.4 Tropical cyclones over the western North Pacific and the South China Sea

- ○ A total of 29 tropical cyclones (TCs) with maximum wind speeds of 34 kt[19] or higher formed over the western North Pacific and the South China Sea in 2018, which was above normal.
- ○ The numbers of formations show no significant long-term trend.

In 2018, 29 tropical cyclones (TCs) with maximum wind speeds of ≥ 34 kt formed over the western North Pacific and the South China Sea (Figure 2.4-1), which was above the normal (i.e., the 1981 – 2010 average) of 25.6. The numbers of formations show no discernible long-term trend during the analysis period from 1951 to 2018, but have often been lower since the latter half of the 1990s than in previous years. Numbers of TCs with maximum wind speeds of ≥ 34 kt approaching and making landfall in Japan were 16 and 5 (Figure 2.4-2), both of which were above the normal of 11.4 and 2.7, respectively. The numbers of TCs approaching Japan also show no discernible long-term trend during the same period from 1951 to 2018.

Figure 2.4-3 shows the numbers and rates of strong TCs with maximum wind speeds of ≥ 64 kt to those with maximum wind speeds of ≥ 34 kt from 1977 (the year in which the collection of complete data on maximum wind speeds near TC centers began). The numbers of strong TCs show no discernible trend.

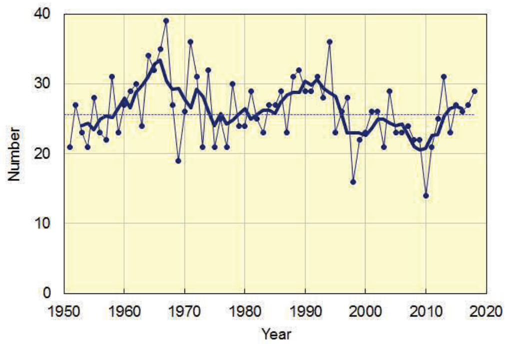

Figure 2.4-1 Time-series of the numbers of TCs with maximum wind speeds of ≥ 34 kt forming in the western North Pacific and the South China Sea from 1951 to 2018. The thin and thick lines represent annual and five-year running means, respectively.

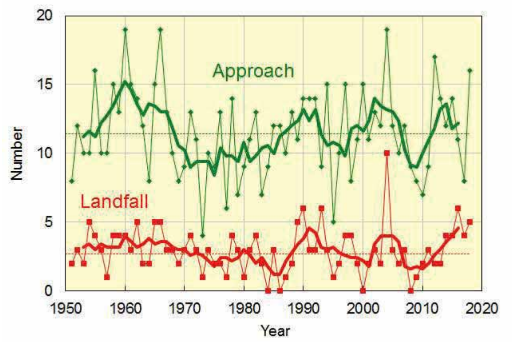

Figure 2.4-2 Time-series of the numbers of TCs with maximum wind speeds of ≥ 34 kt approaching (green) and making landfall in Japan (red) from 1951 to 2018. The thin and thick lines represent annual and five-year running means, respectively.

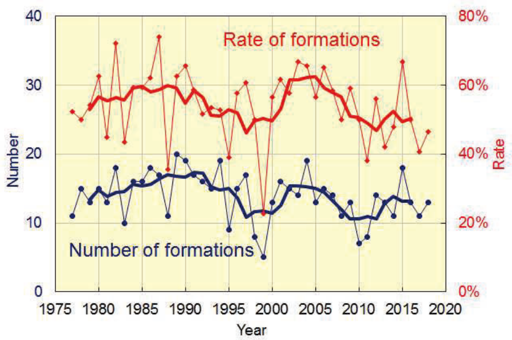

Figure 2.4-3 Time-series of the numbers of strong TCs with maximum wind speeds of ≥ 64 kt (blue) and rates of the strong TCs to the total TCs with maximum wind speeds of ≥ 34 kt (red) forming in the western North Pacific and the South China Sea from 1977 to 2018. The thin and thick lines represent annual and five-year running means, respectively.

19 One knot (kt) is about 0.51 m/s

2.5 Sea surface temperature[20]

- The annual mean global average sea surface temperature (SST) in 2018 was 0.22°C above the 1981 – 2010 average, which was the fourth highest since 1891 (highest: 2016; second highest: 2015; third highest: 2017).
- The global average SST has risen at a rate of about +0.54°C per century.
- Annual average SSTs around Japan have risen by +1.12°C per century.

2.5.1 Global sea surface temperature

The annual mean global average SST in 2018 was 0.22°C above the 1981 – 2010 average. This was the fourth highest since 1891 (highest: 2016; second highest: 2015; third highest: 2017). The years from 2014 to 2018 represent the top-five five warmest since 1891.

The linear trend from 1891 to 2018 shows an increase of +0.54°C per century (Figure 2.5-1). Although magnitudes of the long-term SST trend vary by area, it is extremely likely that SSTs have increased in many parts of the world's oceans (Figure 2.5-2). Global average SSTs and global average surface temperatures (Section 2.1) are affected by natural climate variability on inter-annual to inter-decadal time scales as well as by global warming.

On a multi-year time scale, global average SSTs showed a rising trend from the middle of the 1970s to around 2000, before remaining largely static until the early 2010s and thereafter re-assuming an upward trend (Figure 2.5-1, blue line). This is partly because rising trends overlap with decadal-to-multi-decadal variations in the climate system. It is important to estimate the contribution of these internally induced natural variations in order to properly understand global warming. In the next section, the Pacific Decadal Oscillation (PDO) is presented as a typical example of decadal variability observed in SSTs.

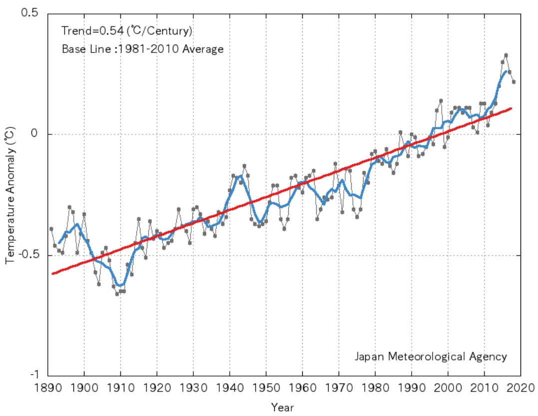

Figure 2.5-1 Time-series representation of global average sea surface temperature anomalies from 1891 to 2018

The black, blue and red lines indicate annual anomalies, the five-year running mean and the long-term linear trend, respectively. Anomalies are deviations from the 1981 – 2010 average.

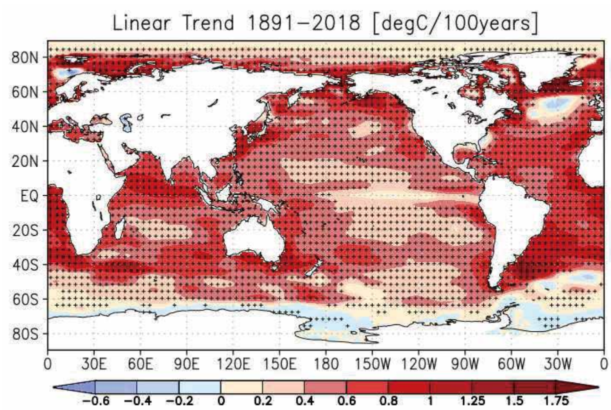

Figure 2.5-2 Linear trend of annual mean sea surface temperature during the period from 1891 to 2018 (°C per century)

Plus signs indicate statistically significant trends with a confidence level of 95%.

20 The results of analysis regarding tendencies of SSTs worldwide and around Japan are published on JMA's website.
https://www.data.jma.go.jp/gmd/kaiyou/english/long_term_sst_global/glb_warm_e.html
https://www.data.jma.go.jp/gmd/kaiyou/english/long_term_sst_japan/sea_surface_temperature_around_japan.html

2.5.2 Sea surface temperature (around Japan)

Figure 2.5-3 shows increase rates of area-averaged annual mean SSTs for 13 areas around Japan. The average SST of all areas around Japan has risen by +1.12°C per century, which is higher than the corresponding value for the North Pacific (+0.52°C per century).

It is virtually certain (statistically significant at a confidence level of 99%) that SSTs have risen by between +0.74 and +1.70°C per century in the sea off Kushiro, the sea off Sanriku, the southern part of the sea off Kanto, the sea off Shikoku and Tokai, the sea east of Okinawa, central and southwestern parts of the Sea of Japan, the Yellow Sea, the East China Sea, and the sea around the Sakishima Islands (areas E1-2, S1-3, N2-3, and W1-4). It is extremely likely (statistically significant at a confidence level of 95%) that SSTs in the eastern part of the sea off Kanto (area E3) have risen by +0.74°C per century. SSTs in the northeastern part of the Sea of Japan (area N1) exhibit no statistical long-term trend.

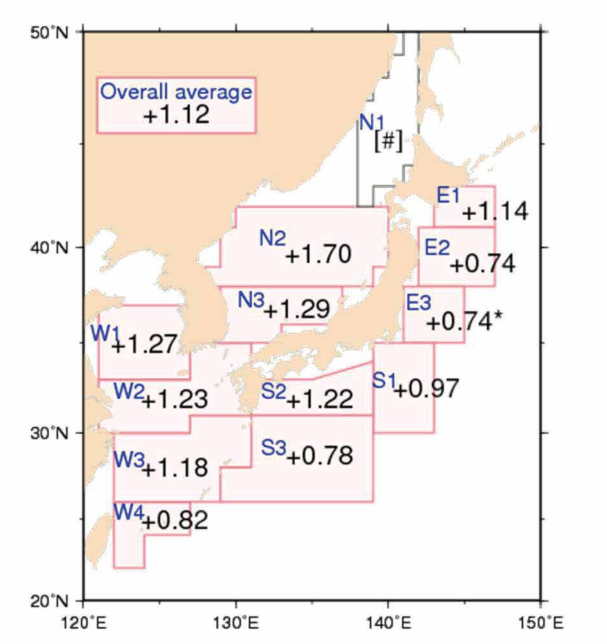

Area number	Area name
E1	Sea off Kushiro
E2	Sea off Sanriku
E3	Eastern part of the sea off Kanto
S1	Southern part of the sea off Kanto
S2	Sea off Shikoku and Tokai
S3	East of Okinawa
N1	Northeastern part of the Sea of Japan
N2	Central part of the Sea of Japan
N3	Southwestern part of the Sea of Japan
W1	Yellow Sea
W2	Northern part of the East China Sea
W3	Southern part of the East China Sea
W4	Sea around the Sakishima Islands

Figure 2.5-3 Increase rates of area-averaged annual mean SSTs around Japan from 1900 to 2018 (°C per century)
Areas with no symbol and those marked with [*] have statistical significant trend at confidence levels of 99% and 95%, respectively. Areas marked with [#] are those where no discernible trend is seen due to large SST variability factors such as decadal oscillation.

2.6 El Niño/La Niña [21] and PDO (Pacific Decadal Oscillation) [22]

- The La Niña event that started in autumn 2017 ended in spring 2018. Thereafter, common characteristics of the past El Niño events have been observed in the equatorial Pacific since autumn 2018.
- Negative PDO index values were generally observed from around 2000 to the early 2010s. Thereafter, the annual mean values have been consecutively positive since 2014, while the value approached zero in 2018.

2.6.1 El Niño/La Niña

An El Niño event is a phenomenon in which sea surface temperatures (SSTs) are above normal over the equatorial Pacific from near the date line to the coast of South America for around a year. In contrast, a La Niña event is a phenomenon in which SSTs are below normal over the same area. Both events occur every few years, causing changes in global atmospheric circulations which result in abnormal weather conditions worldwide. In Japan, cooler summers and warmer winters tend to appear during El Niño events, while hotter summers and colder winters tend to appear during La Niña events.

Figure 2.6-1 shows a time-series representation of SST deviations from climatological means based on a sliding 30-year period for the El Niño monitoring region (5°N – 5°S, 150°W – 90°W) and SST deviations from reference values based on linear extrapolation with respect to the latest sliding 30-year period for the tropical western Pacific region (Eq. – 15°N, 130 – 150°E) since 2008. SSTs in the El Niño monitoring region were below the relevant climatological means from January to April 2018 and have remained above these values since October 2018. SSTs in the Western Pacific region were above the related reference values from January to March of 2018, but have been below these levels since August 2018 except for October. These variations are consistent with the autumn 2017 termination of the La Niña event and the presence of El Niño-like characteristics events since autumn 2018.

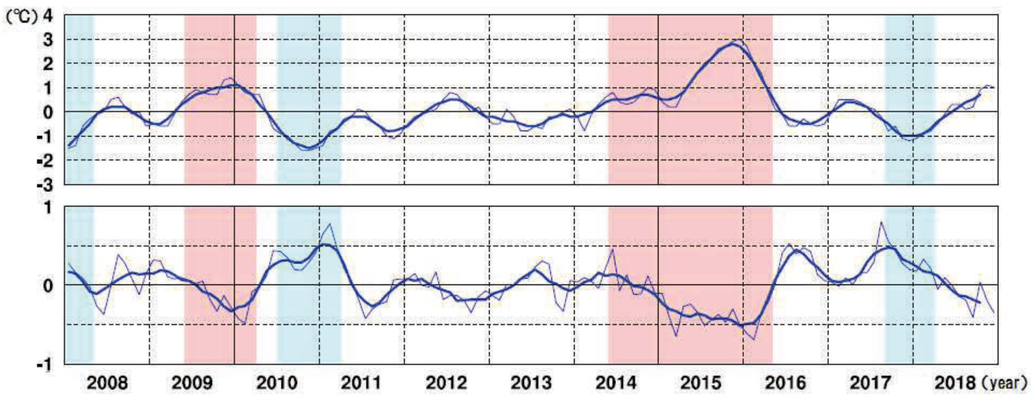

Figure 2.6-1 Time-series representations of SST deviations from the climatological mean based on a sliding 30-year period for the El Niño monitoring region (top) and SST deviations from reference values based on linear extrapolation with respect to the latest sliding 30-year period for the Western Pacific (bottom)
Thin lines indicate monthly means, and smooth thick curves indicate the five-month running mean.
Red shading denotes El Niño periods, and blue shading denotes La Niña periods.

---

21 See the Glossary for terms relating to El Niño phenomena. Monthly diagnosis reports, ENSO monitoring products, ENSO indices and El Niño outlooks are published on JMA's website.
https://ds.data.jma.go.jp/tcc/tcc/products/elnino/index.html
22 The PDO index time series is published on JMA's website.
https://ds.data.jma.go.jp/tcc/tcc/products/elnino/decadal/pdo.html

2.6.2 Pacific Decadal Oscillation

SST variability is also observed on time scales ranging from one to several decades in addition to El Niño/La Niña events, whose time scale is several years, and long-term trends associated with global warming. Among these, the atmosphere and oceans tend to co-vary with a period of more than ten years in the North Pacific in a phenomenon known as the Pacific Decadal Oscillation (PDO). When SSTs are lower (higher) than their normals in the central part of the North Pacific, those in its part along the coast of North America are likely to be higher (lower) than their normals. This seesaw pattern changes slowly, and appears repeatedly with a period of more than ten years. The PDO index, which is defined by the SST anomaly pattern in the North Pacific, is used as a measure of phase and strength of the oscillation. It is noted that both the PDO index and SST anomaly patterns associated with PDO include relatively short-timescale variabilities such as El Niño/La Niña events in addition to decadal to multi-decadal components.

When the PDO index is positive (negative), SSTs in the central part of the North Pacific are likely to be lower (higher) than their normals in addition to those along the coast of North America, and those in the equatorial part from near the date line to the coast of South America are likely to be higher (lower) than normal. This tendency is analogous to the patterns observed in El Niño (La Niña) events (Figure 2.6-2). Additionally, sea level pressures (SLPs) in the high latitudes of the North Pacific are likely to be lower (higher) than their normals in the same time (Figure 2.6-3). This indicates that the Aleutian Low is stronger (weaker) than its normal in winter and spring. These atmospheric variations affect meteorological conditions mainly in North America. When the PDO index is positive, winter temperatures tend to be high in the northwestern part of North America and the northern part of South America, and low in the southeastern part of the USA and in parts of China (Mantua and Hare, 2002).

The PDO index was generally positive from the late 1920s to the early 1940s and from the late 1970s to around 2000, and was generally negative from the late 1940s to the mid-1970s and from around 2000 to the early 2010s. The annual mean PDO index value has remained positive since 2014, although it was close to zero (+0.0) in 2018 (Figure 2.6-4).

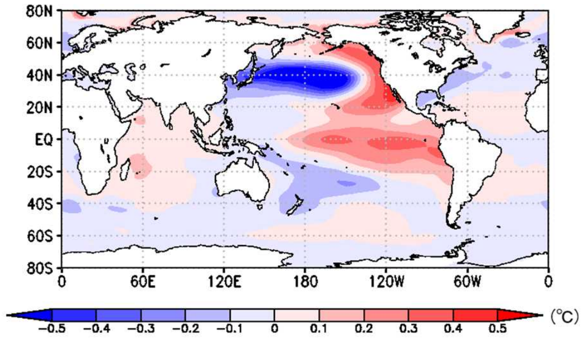

Figure 2.6-2 Typical SST anomaly patterns in the positive phase of the PDO

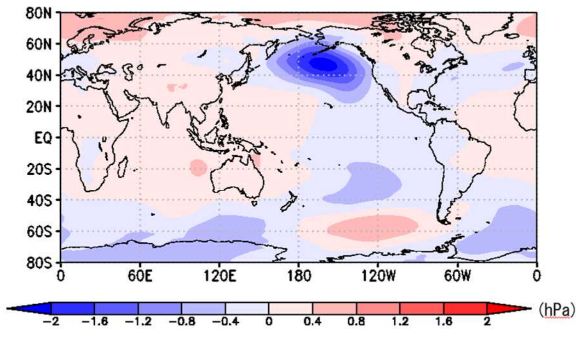

Figure 2.6-3 Typical SLP anomaly patterns in the positive phase of the PDO

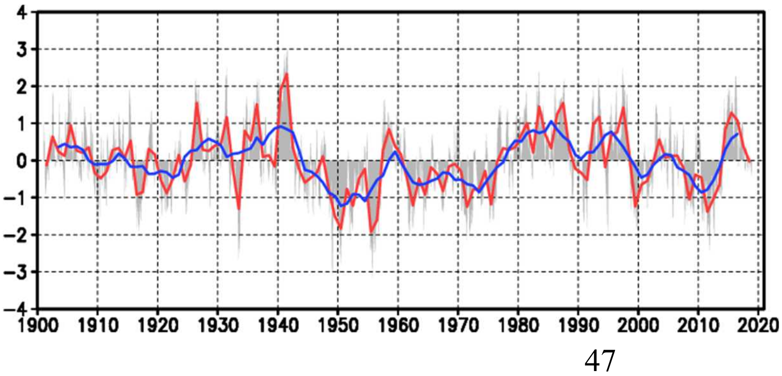

Figure 2.6-4 Time-series of the PDO index

The red line represents annual mean values for the PDO index, the blue line represents five-year running mean values, and the gray bars represent monthly values.

2.7 Global upper ocean heat content[23]

○ An increase in globally integrated upper ocean heat content was observed from 1950 to 2018 with a linear trend of 2.35 × 10^{22} J per decade.

Oceans have a significant impact on the global climate because they cover about 70% of the earth's surface and have high heat capacity. According to the Intergovernmental Panel on Climate Change Fifth Assessment report (IPCC, 2013), more than 60% of the net energy increase in the climate system from 1971 to 2010 is stored in the upper ocean (0 – 700 m), and about 30% is stored below 700 m. Oceanic warming results in sea level rises due to thermal expansion.

It is virtually certain that globally integrated upper-ocean (0 – 700 m) heat content (OHC) rose between 1950 and 2018 at a rate of 2.35 × 10^{22} J per decade as a long-term trend with interannual variations (statistically significant at a confidence level of 99%) (Figure 2.7-1). This trend corresponds to a rise of 0.025°C per decade in the globally averaged upper-ocean (0 – 700 m) temperature. OHC has exhibited marked increases since the mid-1990s. These long-term trends can be attributed to global warming caused by increased concentrations of anthropogenic greenhouse gases such as CO_2 as well as natural variability.

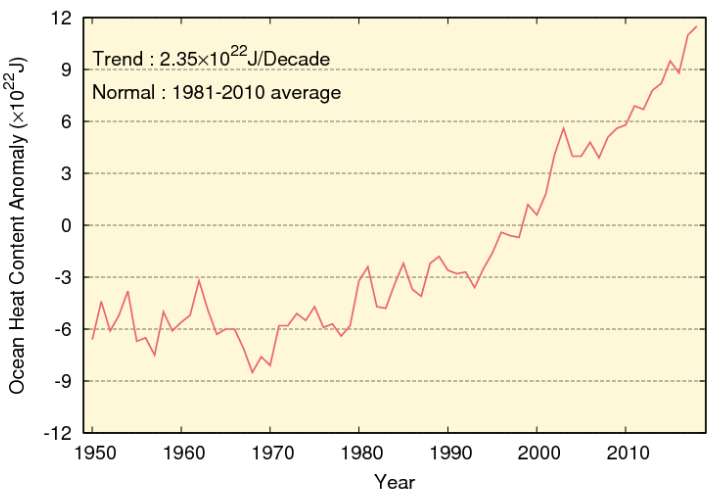

Figure 2.7-1 Time-series representation of the globally integrated upper ocean (0 – 700 m) heat content anomaly
The 1981 – 2010 average is referenced as the normal.

23 The results of ocean heat content analysis are published on JMA's website.
https://www.data.jma.go.jp/gmd/kaiyou/english/ohc/ohc_global_en.html

2.8 Sea levels around Japan [24]

- A trend of sea level rise has been seen in Japanese coastal areas since the 1980s.
- No trend of sea level rise was seen in Japanese coastal areas for the period from 1906 to 2018.

The IPCC Fifth Assessment Report 2013 (AR5) concluded that the global mean sea level had risen due mainly to 1) oceanic thermal expansion, 2) changes in mountain glaciers, the Greenland ice sheet and the Antarctic ice sheet, and 3) changes in land water storage. The report also said it is very likely that the mean rate of global average sea level rise was 1.7 [1.5 to 1.9] mm/year between 1901 and 2010, 2.0 [1.7 to 2.3] mm/year between 1971 and 2010, and 3.2 [2.8 to 3.6] mm/year between 1993 and 2010, where the values in square brackets show the 90% uncertainty range.

Sea levels in Japanese coastal areas exhibited no rise from 1906 to 2018 (Figure 2.8-1), but have shown a rising trend since the 1980s. Recent rates of rise around the country have been 1.1 [0.6 to 1.6] mm/year from 1971 to 2010 and 2.8 [1.3 to 4.3] mm/year from 1993 to 2010. These are comparable to the global average figures provided in AR5.

In Japanese coastal areas, variations with 10- to 20-year periods were between 1906 and 2018. The major factor behind sea level variations with 10- to 20-year periods is the variability of atmospheric circulation over the North Pacific. Westerlies in the mid-latitudes of the Northern Hemisphere are strengthened in boreal winter, and the consequent decadal variations in turn cause sea level variations in the central North Pacific. These propagate westward due to the earth's rotation, causing sea level rise around Japan.

The extent to which global warming has contributed to sea level change around Japan remains unclear due to the involvement of various other factors such as variations with 10- to 20-year periods as mentioned above. Continuous monitoring is needed to clarify the long-term trend of sea level rise caused by global warming.

24 Sea levels around Japan are published on the JMA's website.
https://www.data.jma.go.jp/gmd/kaiyou/english/sl_trend/sea_level_around_japan.html

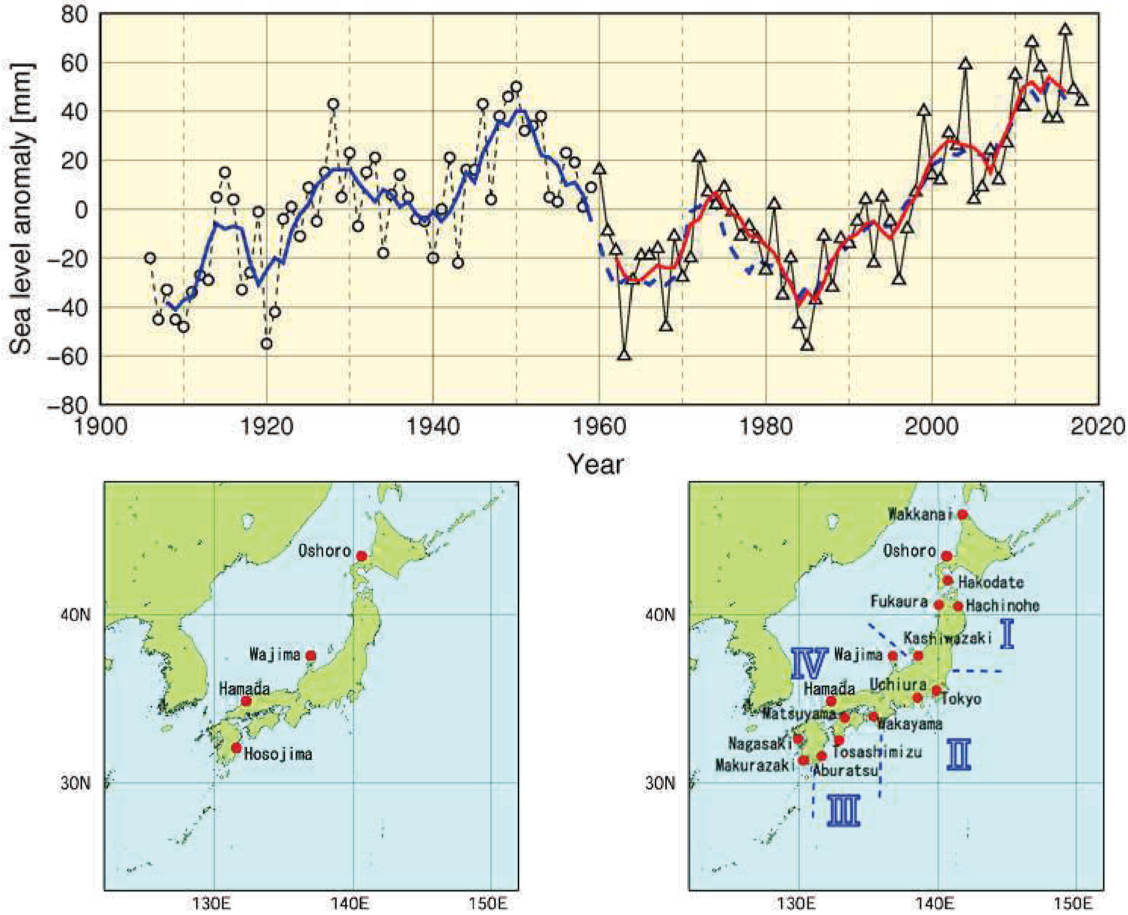

Figure 2.8-1 Time-series representation of annual mean sea levels (1906 – 2018) and locations of tide gauge stations

Tide gauge stations assessed as being affected to a lesser extent by crustal movement are selected. The four stations shown on the map on the left are used for the period from 1906 to 1959, and the sixteen shown on the right are used for the period since 1960. From 1906 to 1959, a time-series representation of mean annual mean sea level anomalies for the selected stations is shown. For the period since 1960, the nation's islands were then divided into four regions based on sea level variation characteristics, annual mean sea level anomalies were averaged for each of the regions, and the variations were plotted in the figure. The four regions are I: from Hokkaido to Tohoku district; II: from Kanto to Tokai district; III: from the Pacific coast of Kinki to that of Kyushu district; and IV: from Hokuriku to East China Sea coast of Kyushu district. Sea level variations are plotted on the chart as a time-series representation of annual mean sea level anomalies for each year, obtained using the 1981 to 2010 average as the normal. The solid blue line represents the five-year running mean of annual sea level anomalies averaged among the four stations shown in the lower left map, while the solid red line represents that averaged among the four divided regions in the lower right map. The dashed blue line represents the value averaged among the four stations shown in the lower left map for the same period shown by the solid red line (after 1960) for reference. The coefficient of correlation between the solid red line and the dashed blue line from 1962 to 2016 is as high as 0.98. Accordingly, the extent to which changing the tide gauge stations used in the monitoring affects the analysis of variance of sea level anomalies can be regarded as small. Among the tide gauge stations, those at Oshoro, Kashiwazaki, Wajima and Hosojima belong to the Geospatial Information Authority of Japan. Sea level data for the Tokyo station are available from 1968 onward. Sea level data for the period from 2011 to 2018 from Hakodate, Fukaura, Kashiwazaki, Tokyo and Hachinohe were not used due to possible influences from the 2011 off the Pacific coast of Tohoku Earthquake.

2.9 Sea ice[25]

○ The sea ice extent in the Arctic Ocean is decreasing. In 2018, the annual maximum sea ice extent in the Arctic Ocean was 14.60 × 10^6 km^2, which were the second-lowest value since 1979.

○ The sea ice extent in the Antarctic Ocean is extremely likely to be on an increasing trend, although values observed since 2016 have been lower than normal. In 2018, the annual minimum sea ice extent in the Antarctic Ocean was 2.32 × 10^6 km^2, which was the second lowest value since 1979.

○ The maximum sea ice extent in the Sea of Okhotsk shows a decreasing trend of 0.066 × 10^6 km^2 per decade.

2.9.1 Sea ice in Arctic and Antarctic areas (Figures 2.9-1, 2.9-2, 2.9-3)

Sea ice is formed when sea water in the Arctic and Antarctic freezes. As the albedo (reflection coefficient) of sea ice is greater than that of the ocean surface, sea ice extent reductions caused by global warming result in more solar energy absorption at the surface, which in turn accelerates global warming. Sea ice also affects deep-ocean circulation because the expelled salt as it forms increases the salinity (and therefore the density) of the water below it causing the water to sink.

It is virtually certain that there has been a long-term trend of decrease in sea ice extent in the Arctic Ocean since 1979, when continuous monitoring of sea ice using satellite sensors with similar properties started (statistically significant at a confidence level of 99%). In particular, the reduction in the annual minimum extent is notable. The rate of decrease in the annual minimum up to 2018 was 0.089 × 10^6 km^2 per year. Meanwhile, it is extremely likely that there has been a long-term trend of increase at a rate of 0.015 × 10^6 km^2 per year in the annual mean sea ice extent in the Antarctic Ocean (statistically significant at a confidence level of 95%). However, values observed since 2016 have been lower than normal (Figure 2.9-1).

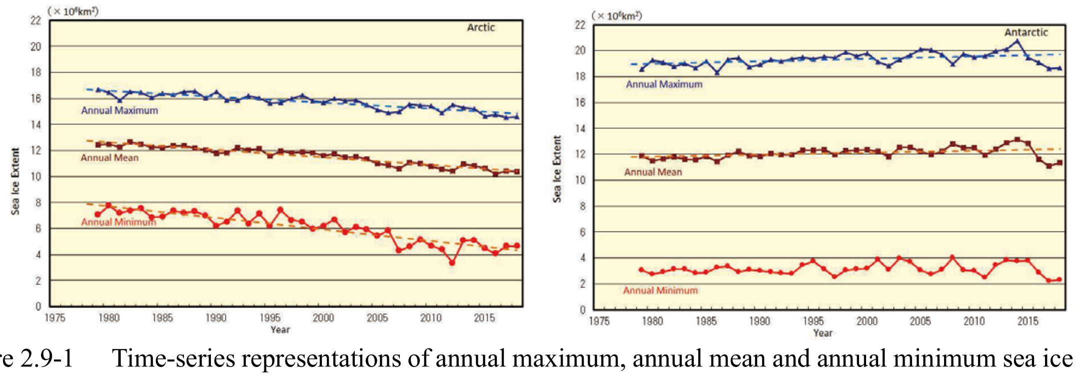

Figure 2.9-1 Time-series representations of annual maximum, annual mean and annual minimum sea ice extent in the Arctic Ocean (including the Sea of Okhotsk and the Bering Sea) (left) and in the Antarctic Ocean (right) from 1979 to 2018

The solid blue, brown and red lines indicate the annual maximum, the annual mean and the annual minimum sea ice extent, respectively. The dashed lines indicate the linear trends. Sea ice extents are calculated from brightness temperature data provided by NASA (the National Aeronautics and Space Administration) and NSIDC (the National Snow and Ice Data Center).

25 Information on sea ice in the Arctic/Antarctic, and in the Sea of Okhotsk are published on JMA's website.
https://www.data.jma.go.jp/gmd/kaiyou/english/seaice_global/series_global_e.html (Arctic/Antarctic)
https://www.data.jma.go.jp/gmd/kaiyou/english/seaice_okhotsk/series_okhotsk_e.html (Sea of Okhotsk)

In 2018, the annual maximum Arctic sea ice extent was 14.60 × 10^6 km^2 on March 16, marking the second-lowest value after 2017 since 1979. The extent subsequently decreased during spring and summer in the Northern Hemisphere and reached its annual minimum of 4.66 × 10^6 km^2 on September 17, marking the eighth-lowest value since 1979. Meanwhile, the Antarctic sea ice extent was at its annual minimum of 2.32 × 10^6 km^2 on February 18, also marking the second-lowest value after 2017 since 1979. The extent subsequently increased during the autumn and winter months of the Southern Hemisphere and reached its annual maximum of 18.65 × 10^6 km^2 on September 30, marking the fourth-lowest value since 1979 (Figures 2.9-1, 2.9-2, 2.9-3).

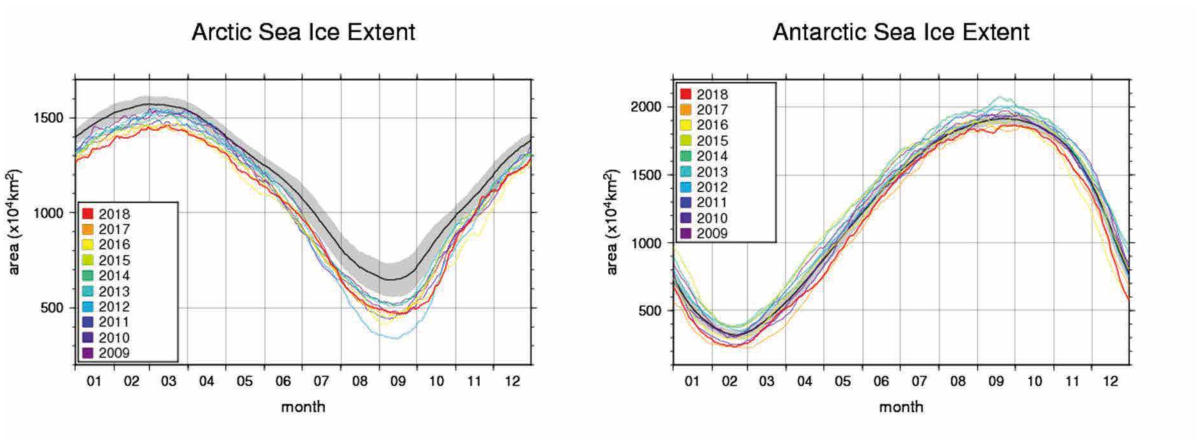

Figure 2.9-2 Annual variations of sea ice extent in the Arctic (left) and Antarctic (right) areas in 2018 (red line)
Black lines represent the normal, and shading represents the range of the normal.

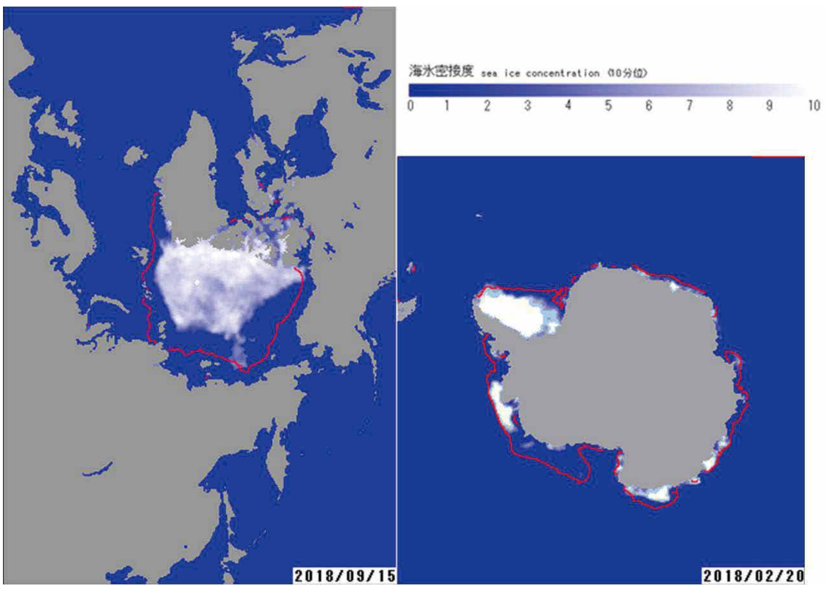

Figure 2.9-3 Annual minimum sea ice distribution for the Arctic and Antarctic
The figure on the left shows Arctic sea ice concentration on September 15 2018, and on the right is Antarctic sea ice concentration on February 20 2018. The red lines represent the normal sea ice edge for the relevant days.

2.9.2 Sea ice in the Sea of Okhotsk (Figure 2.9-4)

The Sea of Okhotsk is the southernmost sea in the Northern Hemisphere where sea ice is observed across a wide area. The variation of the sea ice in the Sea of Okhotsk has effect on climate in coastal area facing the Sea of Okhotsk in Hokkaido and water quality of Oyashio.

The maximum[26] sea ice extent in the Sea of Okhotsk shows large interannual variations. However, it is virtually certain that it exhibited a long-term trend of decrease for the period from 1971 to 2018 (statistically significant at the confidence level of 99%). The maximum extent has decreased by 0.066 × 10^6 km^2 per decade (corresponding to 4.2% of the Sea of Okhotsk's total area).

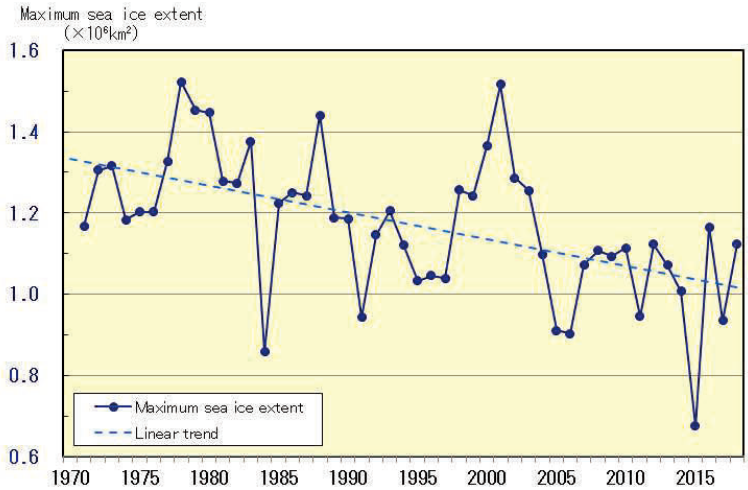

Figure 2.9-4 Time-series representations of maximum sea ice extent for the Sea of Okhotsk from 1971 to 2018
Straight line indicates the linear trend.

26 The maximum sea ice extent: It shows sea ice extent that sea ice was the most expanding of every five days in the winter.

2.10 Snow cover in the Northern Hemisphere

- ○ It is extremely likely that a decreasing trend is observed in the interannual variability of the total snow cover extent in the Northern Hemisphere for January, June and the period from September to December and in Eurasia for April, June and the period from September to December.
- ○ In winter 2017/2018, there were more days of snow cover than normal over the central part of North America and Europe, and fewer over the western part of North America and from Central Asia to East Asia.

JMA monitors snow-cover variations in the Northern Hemisphere using analysis data from satellite observations[27] based on its own algorithm. The average seasonal migration of snow cover in the Northern Hemisphere normally peaks around January – February and decreases in spring.

In the Northern Hemisphere (north of 30°N), it is extremely likely (statistically significant at a confidence level of 95%) that a decreasing trend is observed in the interannual variability of the total snow cover extent over the 31-year period from 1988 to 2018 for January, June and the period from September to December, while no discernible trend is seen for the period from February to May (Figure 2.10-1 (a) and (c)). In Eurasia (north of 30°N from 0° to 180°E), it is extremely likely (statistically significant at a confidence level of 95%) that a decreasing trend is observed in the interannual variability of the total snow cover for April, June and the period from September to December, while no discernible trend is seen for the period from January to March and May (Figure 2.10-1 (b) and (d)). In winter (December to February) 2017/2018, there were more days of snow cover than normal over the central part of North America and Europe, and fewer over the western part of North America and from Central Asia to East Asia (Figure 2.10-1 (e)). In November 2018, there were more days of snow cover than normal over North America and Central Asia, and fewer from eastern Europe to western Russia and over East Asia (Figure 2.10-1 (f)).

The albedo of snow-covered ground (i.e., the ratio of solar radiation reflected by the surface) is higher than that of snow-free ground. The variability of snow cover has an impact on the earth's surface energy budget and radiation balance, and therefore on the climate. In addition, snow absorbs heat from its surroundings and melts, thereby providing soil moisture and related effects on the climate system. The variability of atmospheric circulation and oceanographic conditions affects the amount of snow cover, which exhibits a close and mutual association with climatic conditions. Snow-cover variations in Eurasia and other parts of the Northern Hemisphere may affect climate conditions in Japan, but the mechanisms behind such a potential influence remain unclear. The accumulation of future observation data in addition to the current body of information and the implementation of related research are expected to increase the reliability of statistical work to identify trends of snow cover extent and help to elucidate how snow-cover variations affect climate conditions.

27 The Defense Meteorological Satellite Program (DMSP) polar-orbiting satellites of the USA, equipped with the Special Sensor Microwave/Imager (SSM/I) and the Special Sensor Microwave Imager Sounder (SSMIS)

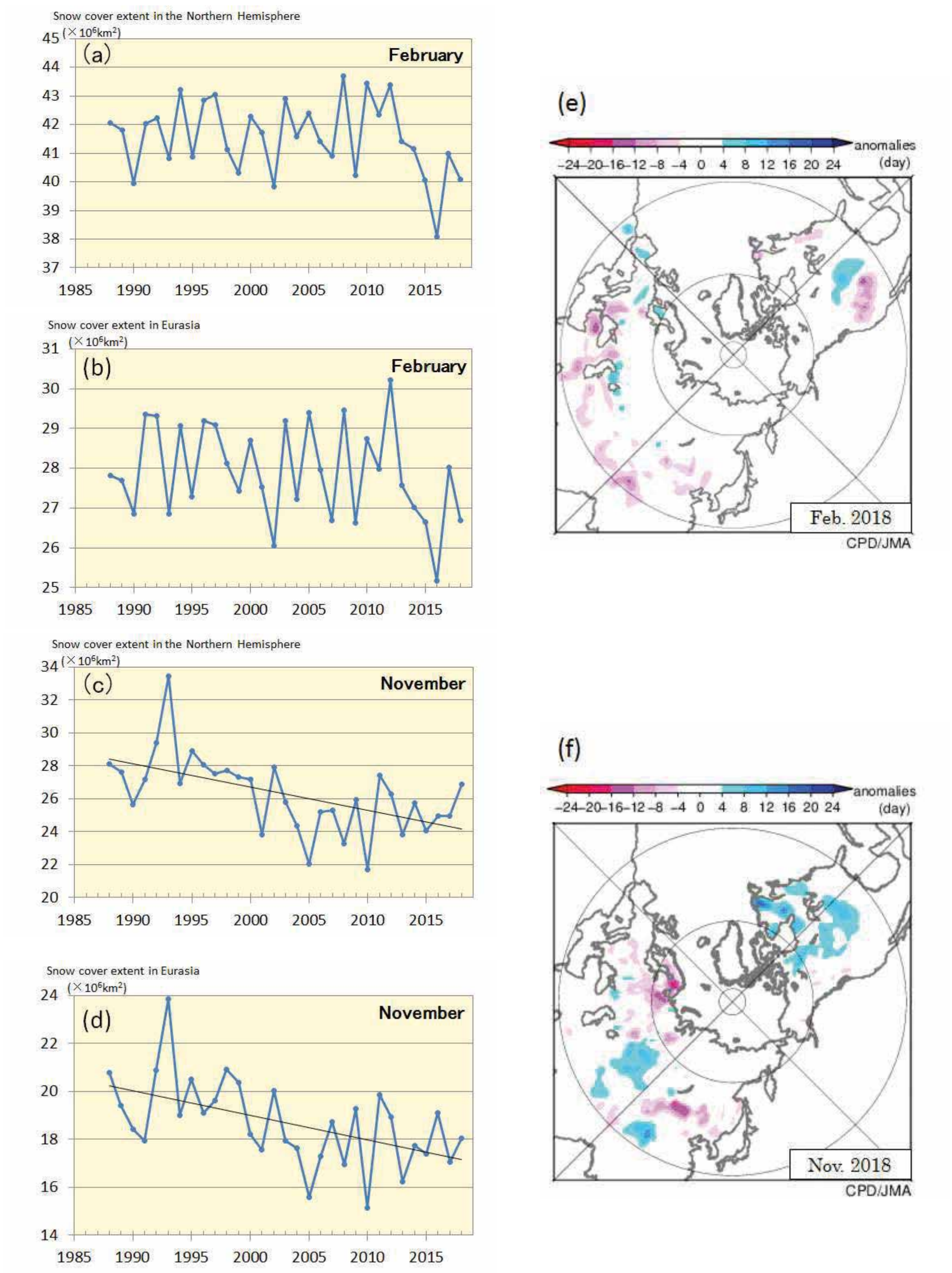

Figure 2.10-1 Interannual variations in the total area of monthly snow cover (km²) in the Northern Hemisphere (north of 30°N) for (a) February and (c) November and in Eurasia (north of 30°N, from 0° to 180°E) for (b) February and (d) November from 1988 to 2018, and anomalies in the number of days with snow cover for (e) February and (f) November in 2018

(a) - (d): The blue lines indicate the total snow cover area for each year, and the black lines show linear trends (statistically significant at a confidence level of 95%).

(e) - (f): Blue (red) shading indicates more (fewer) days of snow cover.

The base period for the normal is 1989 – 2010.

Chapter 3 Atmospheric and Marine Environment Monitoring

3.1 Monitoring of greenhouse gases[28]

- Concentrations of carbon dioxide both in the air and in oceans are increasing.
- Concentrations of atmospheric methane have shown an ongoing increase (with the exception of a stationary phase from 1999 to 2006).
- Concentrations of atmospheric nitrous oxide are increasing.

JMA operates the World Data Centre for Greenhouse Gases (WDCGG)[29] to collect, maintain and provide data on greenhouse gases for related monitoring on a global scale under the Global Atmosphere Watch (GAW) Programme of the World Meteorological Organization (WMO). Analysis of data reported to WDCGG shows that the global mean concentration of greenhouse gases with strong impacts on global warming (in particular, carbon dioxide (CO_2), methane (CH_4) and nitrous oxide (N_2O)) continues to increase (Table 3.1-1).

In Japan, JMA monitors surface-air concentrations of greenhouse gases via three observation stations at Ryori in Ofunato, Minamitorishima in the Ogasawara Islands and Yonagunijima in the Nansei Islands. In the western North Pacific, JMA's research vessels observe oceanic and atmospheric CO_2. In addition, sampling of greenhouse gases in upper-air areas using cargo aircraft was commenced in 2011 (Figure 3.1-1).

Table 3.1-1 Atmospheric concentrations of major greenhouse gases (2017)[30]

	Atmospheric mole fraction			Absolute increase from 2016	Relative increase from 2016	Lifetime
	Pre-industrial level around 1750	Global mean in 2017	Relative increase from Pre-industrial level			
Carbon dioxide	About 278 ppm	405.5 ppm	+ 46 %	+2.2 ppm	+0.55 %	-
Methane	About 722 ppb	1,859 ppb	+157 %	+7 ppb	+0.38 %	12.4 years
Nitrous oxide	About 270 ppb	329.9 ppb	+ 22 %	+0.9 ppb	+0.27 %	121 years

28 Information on greenhouse gas monitoring is published on JMA's website.
https://www.data.jma.go.jp/ghg/info_ghg_e.html (Atmospheric greenhouse gases)
https://www.data.jma.go.jp/gmd/kaiyou/english/oceanic_carbon_cycle_index.html
29 See the WDCGG website for more information.
https://gaw.kishou.go.jp/
30 Data on the annual mean mole fraction in 2017 and its absolute and relative differences from the previous year are from WMO (2018b), while data on pre-industrial levels and lifetime are from IPCC (2013). The lifetime of gas as referred to here describes the time scale over which a local instantaneous increment of gas decays. The increase from pre-industrial levels is calculated from mole fractions for the pre-industrial era and 2017.

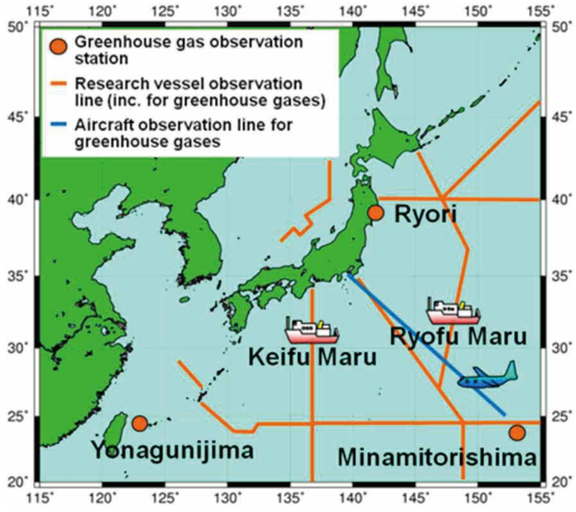

Figure 3.1-1 JMA's greenhouse gas observation network
Observation stations at Ryori, Minamitorishima and Yonagunijima and regular monitoring routes of research vessel and cargo aircraft

3.1.1 Concentration of carbon dioxide

(1) Concentration of global atmospheric carbon dioxide

The global mean concentration of atmospheric CO_2 shows a trend of increase with ongoing seasonal variations (Figure 3.1-2), primarily due to influences associated with human activity such as fossil fuel combustion and deforestation. Some anthropogenic CO_2 is absorbed by the terrestrial biosphere and the oceans, while the rest remains in the atmosphere. As most major sources of CO_2 are located in the Northern Hemisphere, concentrations tend to be higher in the mid- and high latitudes there and lower in the Southern Hemisphere (Figure 3.1-3).

The seasonal variability of CO_2 concentration is generally attributable to terrestrial biosphere activity. In summer, active plant photosynthesis consumes masses of CO_2, while emissions from plant respiration and organic-matter decomposition become dominant in winter. As a result, the annual maximum concentration is observed from March to April in the Northern Hemisphere and from September to October in the Southern Hemisphere. Seasonal variations exhibit larger amplitudes in the mid- and high latitudes of the Northern Hemisphere than in the ocean-rich Southern Hemisphere (Figure 3.1-3). Accordingly, the global mean CO_2 concentration usually peaks around April, reflecting the seasonal variations of the Northern Hemisphere.

WDCGG analysis shows that the global mean CO_2 concentration increased by 2.2 ppm from 2016 to 2017, reaching as much as 405.5 ppm (Table 3.1-1). The most recent 10-year average annual growth rate is 2.2 ppm/year, as opposed to the corresponding value of 1.5 ppm/year for the 1990s.

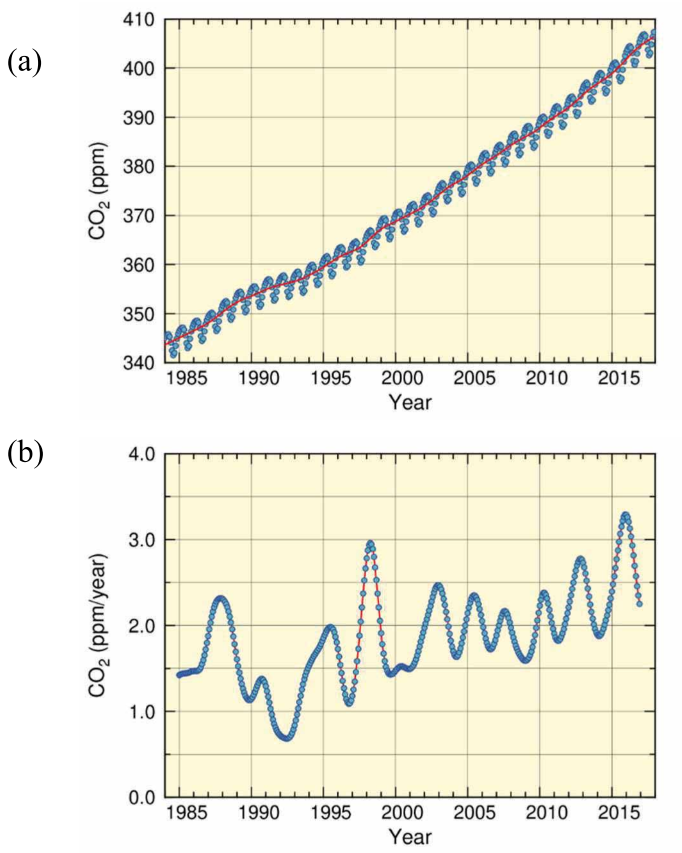

Figure 3.1-2 Global mean concentration of atmospheric CO_2 (a) and annual growth rate (b)

In the upper panel the blue dots are monthly values, and the red line represents the corresponding sequence after removal of seasonal variations. From the latter, the growth rate is derived and shown in the lower panel. Graph content is based on analysis of observation data reported to WDCGG using the method of WMO (2009). Data contributors are listed in WMO (2019).

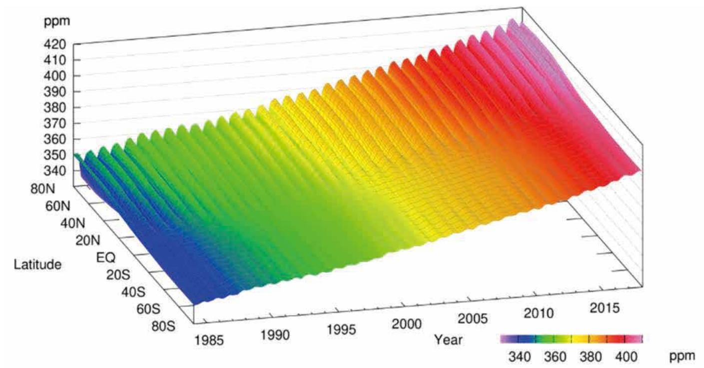

Figure 3.1-3 Latitudinal distribution of atmospheric CO_2 concentrations

The data set and analysis method are as per Figure 3.1-2.

The growth rate of CO_2 concentration exhibits significant interannual variations (Figure 3.1-2 (b)). Major increases in concentration often coincide with El Niño events, largely because the terrestrial biosphere emits more CO_2 than usual under such conditions. In particular, El Niño events bring about high temperatures and droughts in tropical areas and elsewhere, thereby promoting plant respiration and organic-matter decomposition in soil and hindering plant photosynthesis (Keeling *et al.*, 1995; Dettinger and Ghil, 1998).

Figure 3.1-4 illustrates net CO_2 uptake by the terrestrial biosphere as estimated using the method of Le Quéré *et al.* (2016). Here, CO_2 uptake is defined as the amount of anthropogenic emissions minus the increment of atmospheric concentration and the amount of uptake by oceans. The low uptake by the terrestrial biosphere in 2015 and 2016 is generally attributed to the 2014 – 2016 El Niño event (WMO, 2018b). The annual net CO_2 uptake in 2015 and 2016 was 2.1 ± 1.0 GtC/year and 1.8 ± 1.1 GtC/year, respectively, both of which were lower than the 10-year average of 3.4 ± 1.0 GtC/year for the period 2006 – 2015. Similar suppression of net CO_2 uptake was observed in association with the El Niño events of 1997/1998 and 2002/2003. In 1998 in particular, the lowest net uptake since 1990 was recorded. An exception was observed from 1991 to 1992, when net CO_2 uptake by the terrestrial biosphere was large despite the presence of an El Niño event. This is attributable to the eruption of Mt. Pinatubo in June 1991, which triggered worldwide low temperatures and inhibited CO_2 emissions from organic-matter decomposition in soil (Keeling *et al*., 1996; Rayner *et al*., 1999).

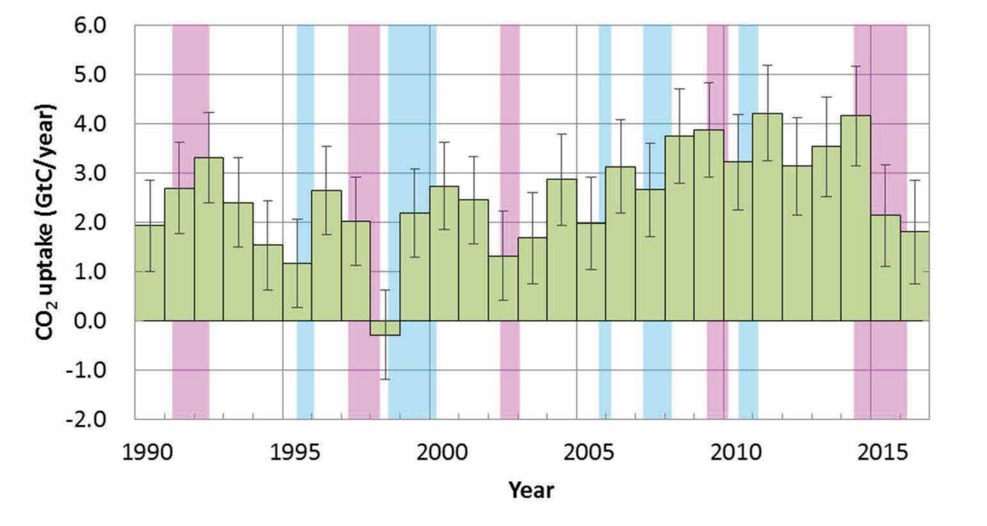

Figure 3.1-4 Annual net CO_2 uptake by the terrestrial biosphere

In this analysis, the net CO_2 uptake is estimated by subtracting the annual increment of atmospheric CO_2 and the amount of uptake by oceans from the amount of anthropogenic emissions. The amount of anthropogenic emissions, stemming from fossil fuel combustion and land-use changes, is based on Le Quéré *et al*. (2018). The annual increment of atmospheric CO_2 is the annual mean of the monthly means shown in Figure 3.1-2 (b). Oceanic uptake is based on Iida *et al*. (2015; see also Section 3.1.1 (3)), and incorporates emissions associated with the natural carbon cycle, corresponding to 0.7 GtC/year (IPCC 2013). Error bars indicate 68% confidence levels. El Niño and La Niña periods are shaded in red and blue, respectively. A negative CO_2 uptake equates to an emission.

(2) Concentration of atmospheric carbon dioxide in Japan

Concentrations of atmospheric CO_2 at all three of Japan's observation stations have shown a continuous increase along with seasonal variations (Figure 3.1-5 (a)). The amplitude of these variations is greater at Ryori than at the other stations because it tends to be larger in higher latitudes of the Northern Hemisphere in association with significant seasonal variations in terrestrial biosphere activity in the mid- and high latitudes (see Figure 3.1-1). Although Yonagunijima and Minamitorishima have similar latitudes, the former tends to observe higher concentrations and seasonal variations with larger amplitudes because of its greater proximity to the Asian continent, which is characterized by major anthropogenic emissions and an extensive biosphere. The annual mean CO_2 concentration in 2018 was 412.0 ppm at Ryori, 409.4 ppm at Minamitorishima and 411.7 ppm at Yonagunijima. All these figures are the highest on record (based on preliminary estimations).

Figure 3.1-5 (b) shows growth rates of CO_2 concentrations observed at the three observation stations. High rates have been observed in most cases during the periods of El Niño events. As a recent example, a sharp increase in CO_2 concentration was observed in association with the event that ran from summer 2014 to spring 2016.

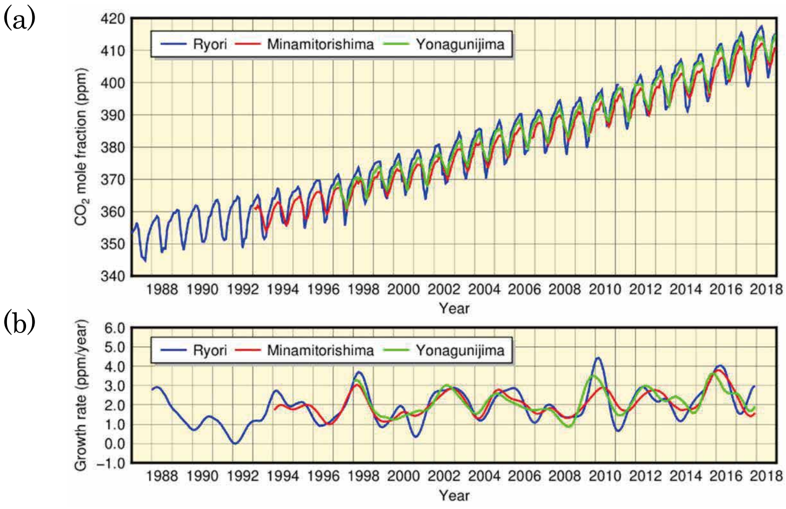

Figure 3.1-5 Monthly mean concentrations (a) and corresponding growth rates (b) of atmospheric CO_2 observed at Ryori (blue), Minamitorishima (red) and Yonagunijima (green)

The method used to calculate the growth rate is described in WMO (2009).

(3) Oceanic carbon dioxide

Based on data collected by JMA research vessels along the 137°E (3 – 34°N) and 165°E (5°S – 35°N) lines, oceanic and atmospheric pCO_2 are increasing in the western North Pacific area (Figures 3.1-6, 3.1-7). The growth rates for oceanic and atmospheric pCO_2 along the 137°E line from 1985 to 2018 were 1.4 – 2.1 and 1.7 – 1.9 µatm/year, respectively, while those along the 165°E line from 1996 to 2018 were 1.6 – 3.0 and 1.8 – 2.1 µatm/year, respectively. Oceanic pCO_2 exhibits seasonal variations, being higher in summer with higher SSTs and lower in winter with lower SSTs, and the range of variation is more volatile at higher latitudes along both lines. Meanwhile, atmospheric pCO_2 is constant and higher than those of oceanic pCO_2 except in summer. Consequently, the ocean absorbs atmospheric CO_2 emissions overall, other than in equatorial areas, resulting in a release of CO_2 into the atmosphere over the year because oceanic pCO_2 values are higher than those of atmospheric pCO_2.

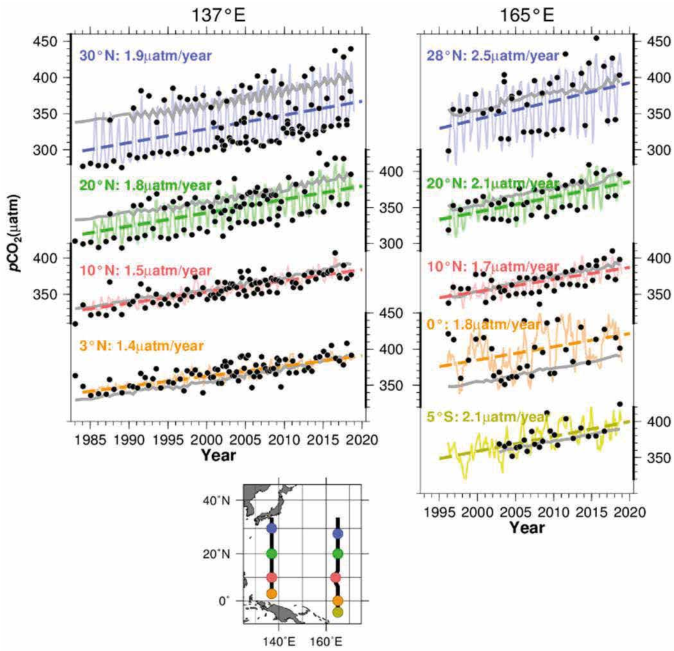

Figure 3.1-6 Annual changes in oceanic and atmospheric pCO_2 along the 137°E (left) and the 165°E (right) lines.

Black plots show oceanic pCO_2 observation values. Solid lines represent monthly oceanic pCO_2 values reconstructed using the method of Ishii et al. (2011), dashed lines show the long-term trend of oceanic pCO_2, and gray lines indicate the observed values of atmospheric pCO_2.

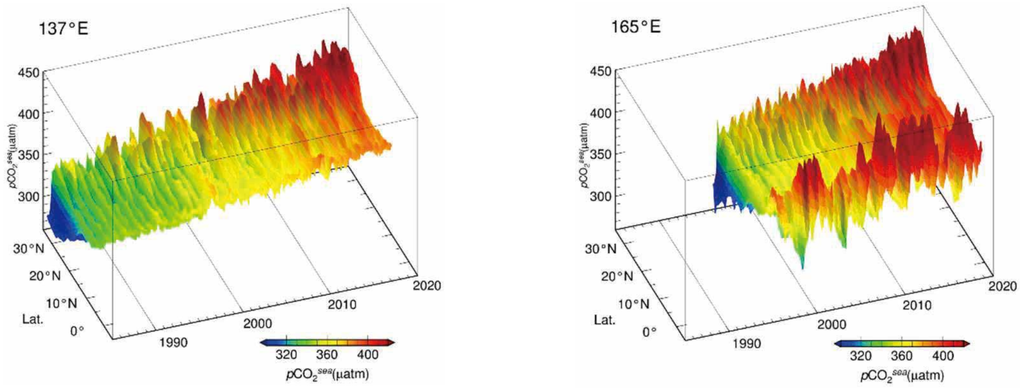

Figure 3.1-7 Time-latitude distribution of oceanic pCO2 along the 137°E (left) and the 165°E (right) lines.

Colors indicate reconstructed monthly oceanic pCO2 value. The part on the left shows oceanic pCO2 along the 137°E (3-34°N) since 1985 and the part on the right shows oceanic pCO2 along the 165°E (5°S-35°N) since 1996.

Analysis of observation data reveals relationships between surface seawater CO_2 concentrations and other oceanographic parameters such as sea surface temperature (SST), salinity and chlorophyll-a concentration, which differ by region. Global oceanic CO_2 concentrations were estimated using datasets of such parameters based on these relationships, and CO_2 exchanges between the atmosphere and the ocean were calculated (Iida *et al.*, 2015). It was found that the ocean releases CO_2 into the atmosphere in equatorial regions and the northern Indian Ocean, where seawater with a high CO_2 concentration upwells and absorbs CO_2 in other regions (Figure 3.1-8 (a)). Lower SSTs in winter and biological CO_2 consumption in spring/autumn result in lower surface ocean CO_2 concentrations and therefore higher CO_2 uptake, especially in the mid-to-high latitudes. Figure 3.1-8 (b) and (c) show monthly and annual variations in global ocean CO_2 uptake, respectively. The estimated mean annual global ocean CO_2 uptake during 1990 to 2017 was 1.8 GtC per year. Considering natural CO_2 efflux of 0.7 GtC per year (IPCC, 2013), which results from riverine input to the oceans, the amount of oceanic CO_2 uptake corresponds to 30 % of all anthropogenic CO_2 emission, which IPCC (2013) estimates to be 9 GtC per year. Global ocean CO_2 uptake is affected by the variability of global SST distribution and biological activity, and decreases/increases in boreal summer/winter (Figure 3.1-8 (b)). The estimated annual global ocean CO_2 uptake has increased since 2000.

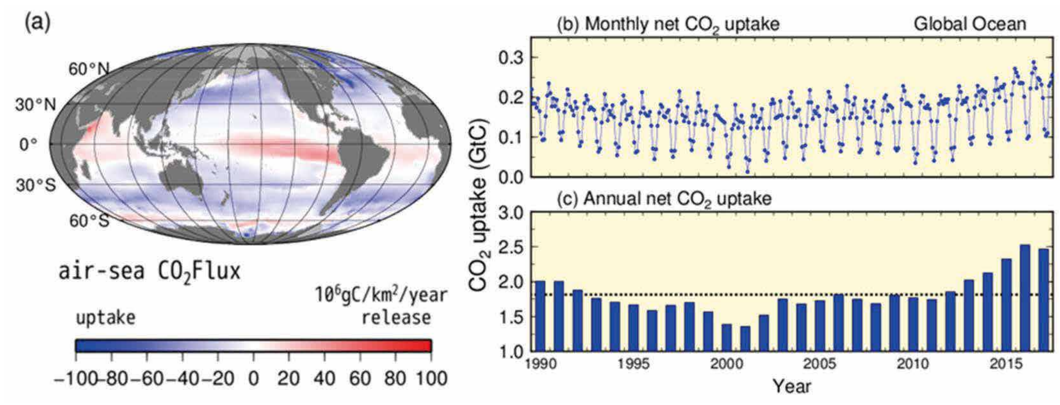

Figure 3.1-8 Distribution of global ocean CO_2 uptake/release for 2017 (a) and time-series representations of monthly (b) and annual (c) CO_2 uptake from 1990 to 2017

The blue/red area in the map on the left (a) indicates ocean uptake/release of CO_2 from/into the atmosphere. The grey area shows the border of the region analyzed. The dotted line in graph (c) shows the 1.8 GtC average for the period from 1990 to 2017.

The column inventory of oceanic CO_2 was estimated using long-term time-series data on dissolved inorganic carbon from 1990s (Figure. 3.1-9). The column inventory rates of oceanic CO_2 between the sea surface and 27.5 σ_θ (1,200 to 1,400 m in depth) along 137°E and 165°E are approximately 5 – 12 and 3 – 12 tC·km^{-2}·year^{-1}, respectively. The column inventory rates of oceanic CO_2 around 20 – 30°N are higher than those at 10°N and 35°N. This is caused by the transport of CO_2 from the surface to the ocean interior by water masses known as North Pacific subtropical mode water and North Pacific intermediate water.

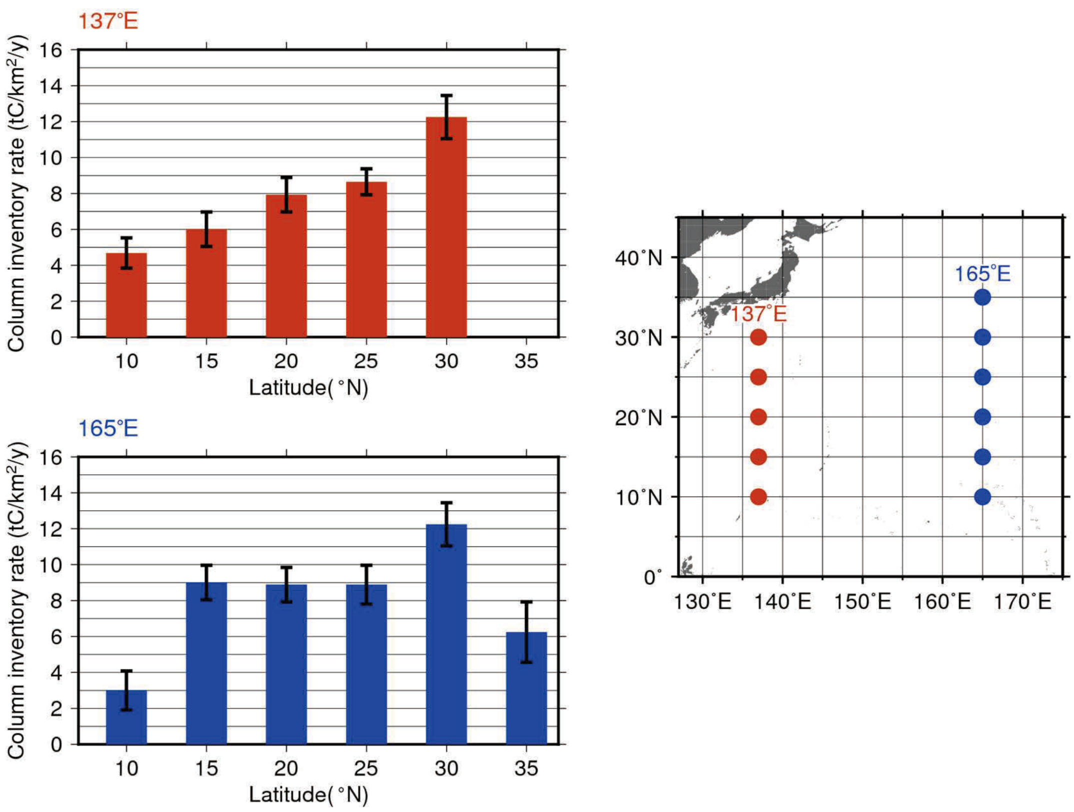

Figure 3.1-9 Changes in oceanic CO_2 between the sea surface and 27.5 σ_θ (approx. 1,200 – 1,400 m in depth) along 137 and 165°E for the periods 1994 – 2018 and 1992 – 2018.

Error bars denote a 95% confidence level

(4) Ocean acidification

The ocean acts as a large sink for CO_2 emitted as a result of human activity, and the chemical properties of seawater have changed due to the uptake and reserve of anthropogenic CO_2. Ocean acidification, known as the decrease in seawater pH (hydrogen ion exponents), is a particular issue of concern because it accelerates global warming by limiting the ocean's capacity of CO_2 uptake from the atmosphere and affects marine ecosystems by disturbing plankton growth. The IPCC AR5 (2013) included an estimate that the average global surface seawater pH has decreased by 0.1 due to ocean uptake of atmospheric CO_2 emitted as a result of human activity since the beginning of the industrial era (1750). According to numerical model experiments based on future CO_2 emission estimates, surface seawater pH will further decease by 0.065 – 0.31 by the end of 21st century. The CO_2 absorbed by the ocean is considered to have been transported into the ocean interior through ocean circulation and biological processes, and to be causing ocean acidification in the interior as well as in the surface layer (Doney et al., 2009).

JMA has long conducted oceanographic observations in the western North Pacific to monitor long-term variability relating to the ocean, such as global warming and ocean acidification. The Agency monitor long-term trends in surface and interior seawater pH along repeat hydrographic lines at 137°E and 165°E, and performs analysis to determine the average decrease in surface seawater pH throughout the Pacific using data on oceanic CO_2 concentration and related factors. The results clearly show a decreasing trend in surface seawater pH for the whole Pacific, and 0.013 to 0.021 and 0.014 to 0.031 per decade at individual stations on the 137°E and 165°E lines, respectively (Figures 3.1-10 and 3.1-11). Ocean interior pH along these lines also shows decreasing trends of 0.011 to 0.035 per decade (Figure 3.1-12) with higher rates in the northern than the southern subtropics due to greater accumulation of anthropogenic CO_2 in the former.

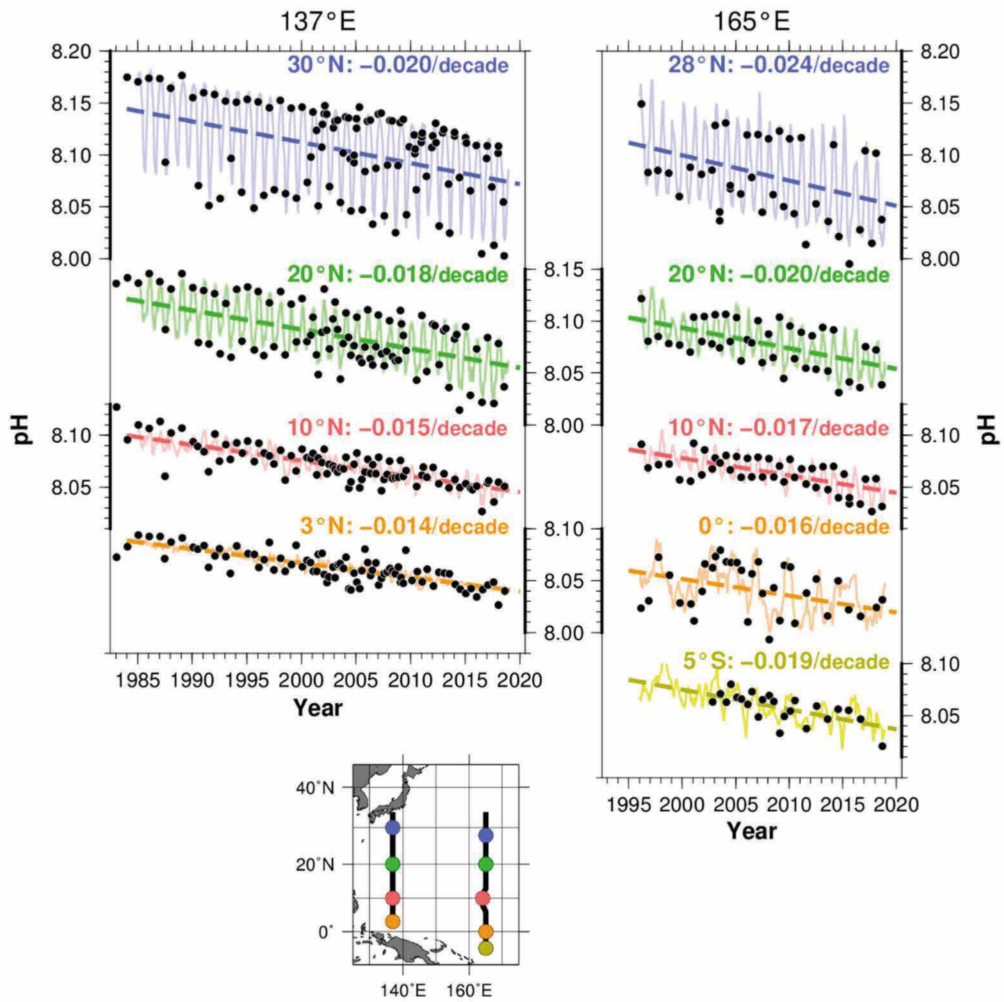

Figure 3.1-10 Long-term trends of pH at each latitude in JMA's repeat hydrographic lines at 137°E (left) and 165°E (right).

Black plots show pH observation values based on pCO_2 observation data. Solid lines represent monthly pH values reconstructed using the method of Ishii et al. (2011), dashed lines show the long-term trend of pH, and numbers indicate rates of change at each latitude.

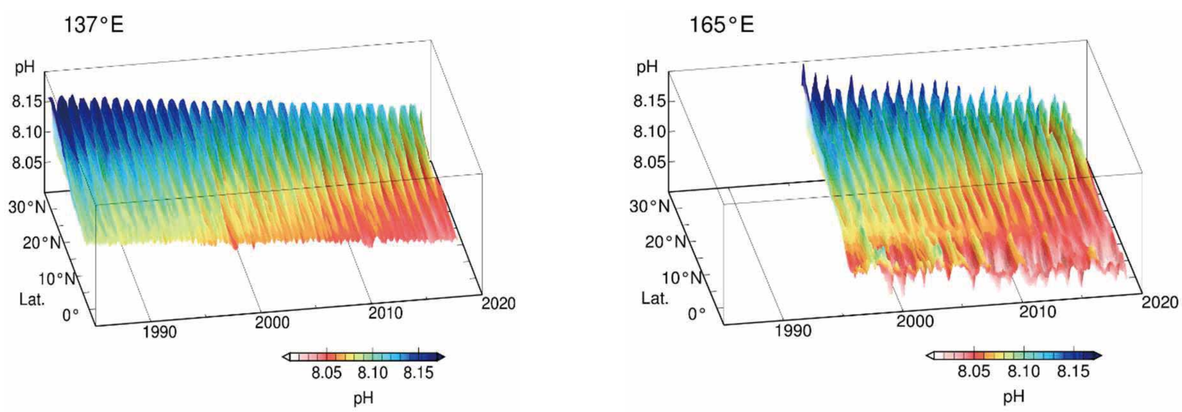

Figure 3.1-11 Time-latitude distribution of pH along the 137°E (left) and the 165°E (right) lines.

Colors indicate reconstructed monthly pH values. The part on the left shows pH along 137°E (3-34°N) since 1985, and the part on the right shows pH along 165°E (5°S-35°N) since 1996.

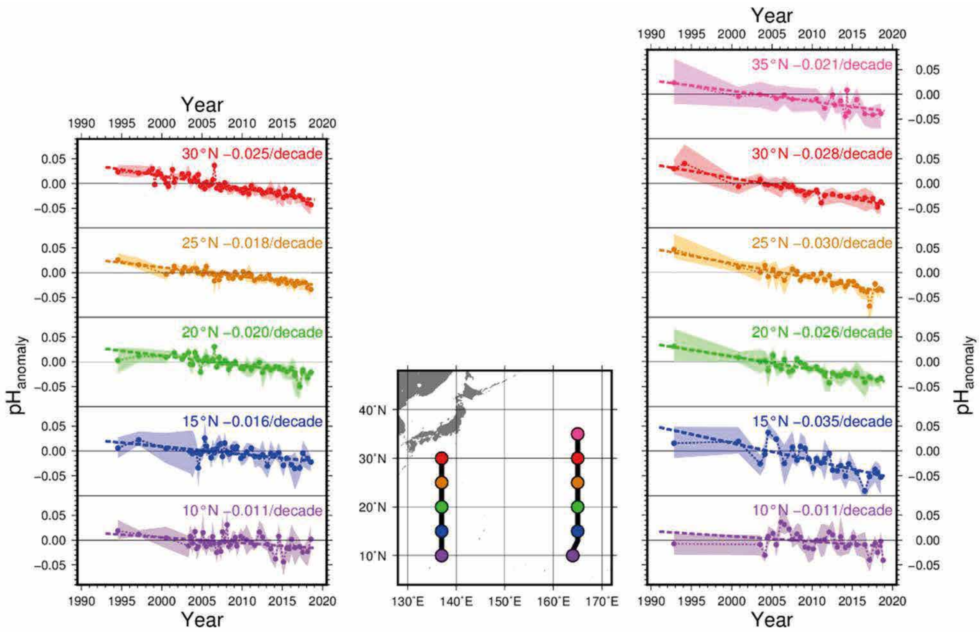

Figure 3.1-12 Long-term trends of pH between 25.0 σ_θ and 26.9 σ_θ (a depth range of about 150~800 m) along 137°E (left) and 165°E (right).

Plots show pH anomalies from the normal (i.e., the average for the period from 1991 to 2010) at each latitude. The shaded areas and bold dotted lines represent the standard deviation range (±1 σ) and the long-term trend, respectively. The numbers indicate rates of change at each latitude.

(5) Concentration of carbon dioxide in the upper air

Since 2011, JMA has monitored upper-air CO_2 concentrations using cargo aircraft with support from Japan Ministry of Defense, with air samples taken along the route from Atsugi Air Base (35.45°N, 139.45°E) to Minamitorishima Island (24.29°N, 153.98°E) during level flight at an altitude of approximately 6 km and during descent to the island once a month (Tsuboi *et al.*, 2013; Niwa *et al.*, 2014).

Figure 3-1.13 shows measured and averaged concentrations for samples collected during level flight in black and blue dots, respectively. Monthly mean concentrations at the ground-based station on the island are also shown in red. The dashed curves in blue and red represent components after removal of seasonal cycles for aircraft and Minamitorishima, respectively. Concentrations exhibit a gradual increase over time in the upper air as well as on the surface, although values tend to be lower in the former.

At ground level on the island, concentrations are higher from winter to spring and lower from summer to fall. Those in the upper air tend to be lower than on the surface during winter to spring, while similar values are observed for the corresponding altitudes in summer. Consequently, the amplitude of seasonal cycles is smaller in the upper air shown in Figure 3-1.14. The Figure shows the vertical dependence of average seasonal cycles based on air samples collected during descent in addition to level-flight data and ground-based data. From winter to spring, concentrations are lower toward higher altitudes.

Figure 3-1.15 shows concentrations for samples taken during descent minus the daily mean value recorded at the ground-based station on the flight date for February (left) and August (right). While concentrations are lower toward higher altitudes in February, there is no clear vertical dependence in August.

The above results suggest that parts of surface air affected by the terrestrial biosphere in continental regions are transported to the ground and upper levels of the island, and that air transport behavior varies with seasons and altitudes. The characteristic of strong vertical dependence from winter to spring and weak dependence from summer to fall is also identified in data from other aircraft observations around North America and Asia (Sweeney *et al*., 2015; Umezawa *et al*., 2018).

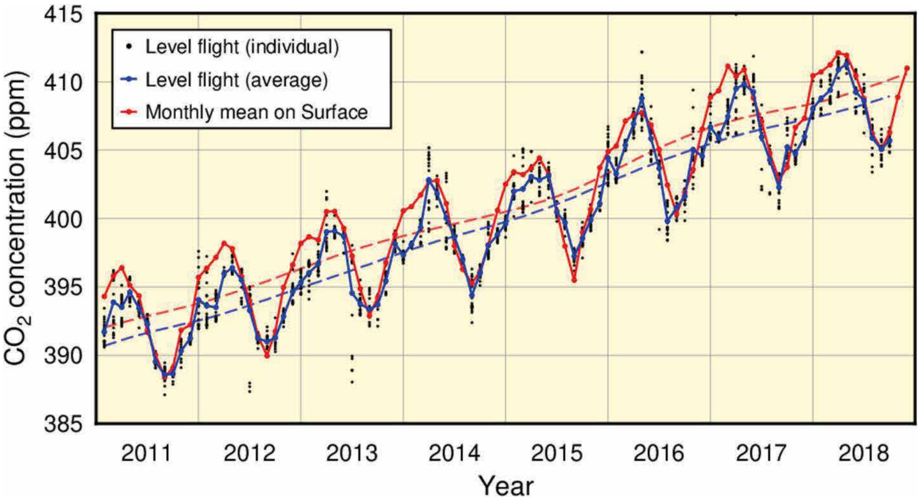

Figure 3.1-13 Measured and averaged CO_2 concentrations for air samples collected during level flight (at a height of approx. 6 km) of cargo aircraft along the route from Atsugi Air Base to Minamitorishima (black and blue dots, respectively) and monthly mean concentrations at the Minamitorishima ground-based station (red dots).

Blue and red dashed curves represent the component after removal of seasonal cycles from the series of red and blue dots, respectively. The analysis is based on WMO (2009).

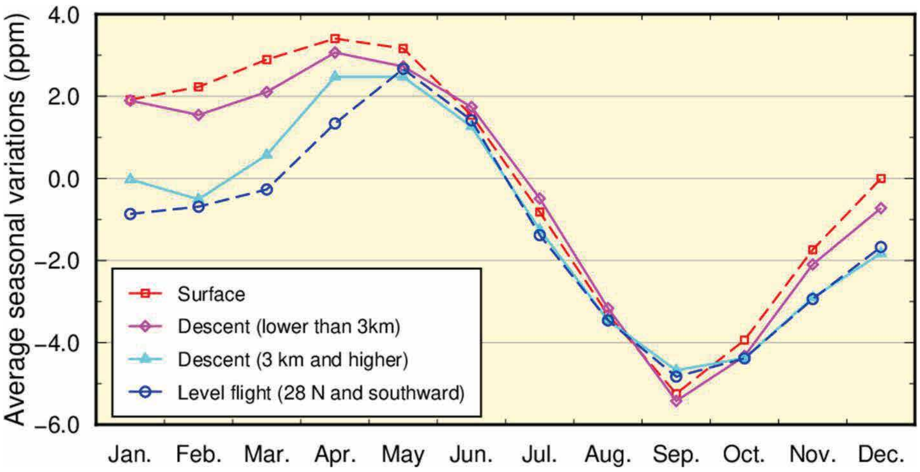

Figure 3.1-14 Vertical dependence of average seasonal cycles around Minamitorishima for monthly mean concentrations on the surface (red), concentrations for air samples taken during level flight at latitudes 28°N and southward (blue), and those taken during descent with altitudes less than 3 km (magenta) and otherwise (cyan).

Monthly values are calculated by averaging concentrations after the removal of long-term trends (components without seasonal cycles) of surface data.

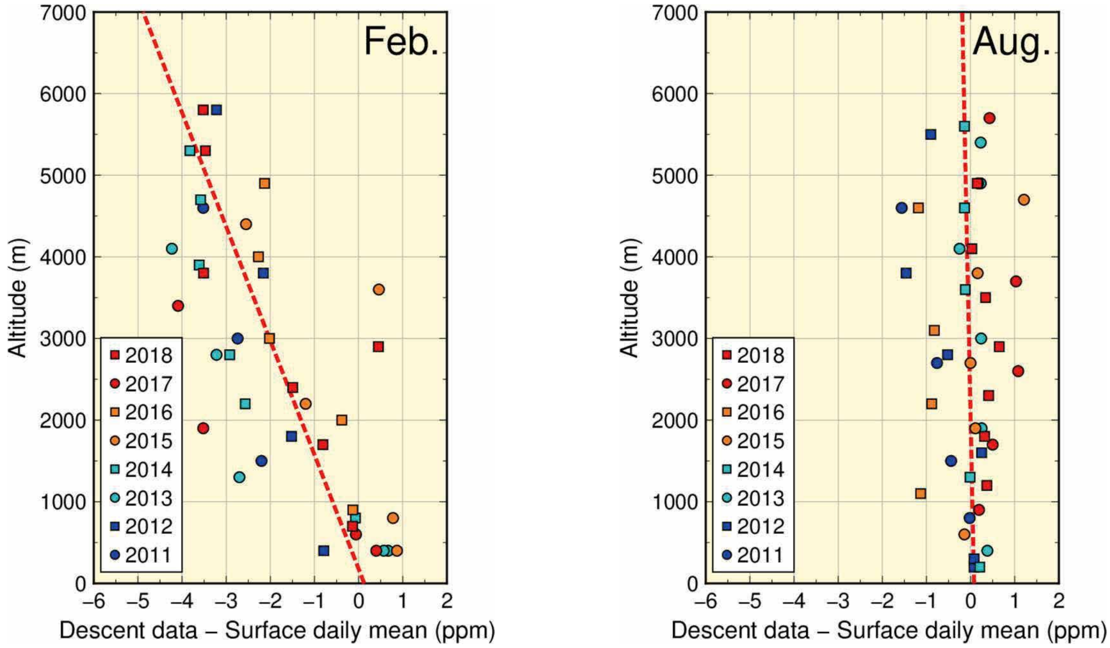

Figure 3.1-15 Vertical variations of CO_2 concentrations over Minamitorishima
Circles and squares show concentrations of air samples taken during descent to the island minus the daily mean value recorded at the ground-based station on the flight date. Symbol colors and shapes represent observation years. Dashed red lines show the vertical gradient of the symbols as determined using the least squares method.

3.1.2 Concentration of methane

(1) Concentration of global atmospheric methane

The global mean concentration of atmospheric CH_4 has been increasing since at least the mid-1980s when worldwide monitoring began, except for a stationary phase from 1999 to 2006 (Figure 3.1-16). The mechanism behind the stationary phase remains unclear, but several scenarios have been proposed (IPCC, 2013). The greater concentrations observed since 2007 indicate an increase in CH_4 emissions from tropical wetlands and human activity in the mid-latitudes of the Northern Hemisphere (WMO, 2018b).

WDCGG analysis shows that the global mean concentration of CH_4 in 2017 was 1,859 ppb, which is the highest since records began (Table 3.1-1).

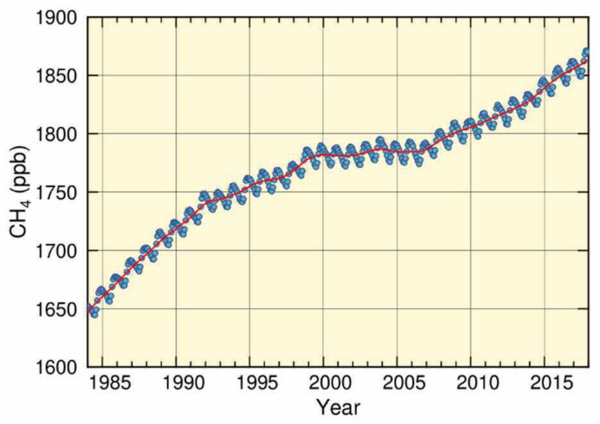

Figure 3.1-16 Global mean concentration of atmospheric CH_4

The blue dots are monthly values, and the red line represents the corresponding sequence after the removal of seasonal variations. Graph content is based on analysis of observation data reported to WDCGG based on the method of WMO (2009). Data contributors are listed in WMO (2019).

Figure 3.1-17 shows the latitudinal dependence of CH_4 concentrations. In the high and mid-latitudes of the Northern Hemisphere, concentrations begin to sharply decrease toward the south. This is because CH_4 is mostly emitted from land areas in the Northern Hemisphere, and disappears due to reaction with hydroxyl radicals[31] over tropical oceans during transportation to the Southern Hemisphere. In summer, more hydroxyl radicals are produced as a result of enhanced ultraviolet radiation, and a larger amount of CH_4 is destroyed. This reaction creates seasonal variation of CH_4 concentrations, as seen in Figures 3.1-16 and 3.1-17.

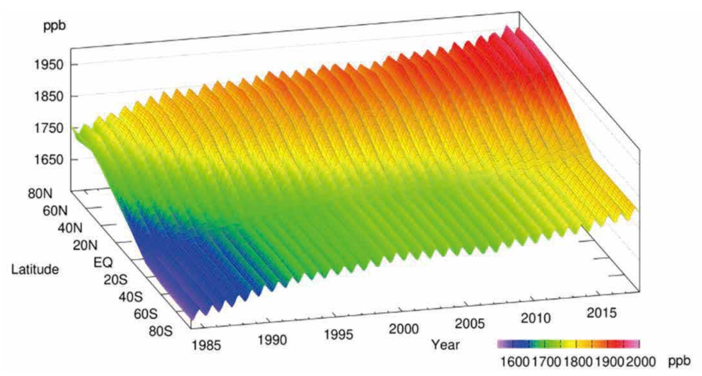

Figure 3.1-17 Latitudinal distribution of atmospheric CH_4 concentrations

The data set and analysis method are as per Figure 3.1-16.

31 Hydroxyl radicals are highly reactive chemicals generated by the reaction of atomic oxygen, which is derived from UV photolysis of ozone, with airborne water vapor. It is particularly abundant at low latitudes, where UV radiation is strong and water vapor is plentiful.

The remarkable increase observed in global mean atmospheric concentrations of CH_4 since the industrial era (+157%) has been much more rapid than that of CO_2 (+46%) (Table 3.1-1). This is partly because the amount of anthropogenic emissions of CH_4 relative to natural emissions exceeds that of CO_2. The long-term trend of CH_4 concentration depends on various factors of uncertainty, including anthropogenic/natural emissions and chemical reactions. Accordingly, further development of the global CH_4 observation network is required.

(2) Concentration of atmospheric methane in Japan

Atmospheric CH_4 concentrations at all of Japan's three observation stations exhibit a trend of increase with seasonal variations in the same way as the global mean concentration (Figure 3.1-18 (a)). Ryori usually observes the highest concentration among the three stations because it is located in the northern part of Japan, where CH_4 sources in the Asian continent are more influential and reaction with hydroxyl radicals is less marked. Although Yonagunijima and Minamitorishima are located at similar latitudes, the former tends to record higher concentrations in winter because CH_4 sources on the Asian continent have a stronger impact there in winter as a result of continental air mass expansion. In summer, meanwhile, a hydroxyl radical-rich maritime air mass covers both stations, and similarly low concentrations are observed. Since 2010, Yonagunijima has occasionally observed concentrations as high as those of Ryori in winter. The annual mean CH_4 concentration in 2018 was 1,941 ppb at Ryori, 1,893 ppb at Minamitorishima and 1,915 ppb at Yonagunijima, all of which are the highest on record (based on preliminary estimations).

The growth rate of atmospheric CH_4 concentration exhibits interannual variations that differ significantly from station to station (Figure 3.1-18 (b)).

(a)

(b)

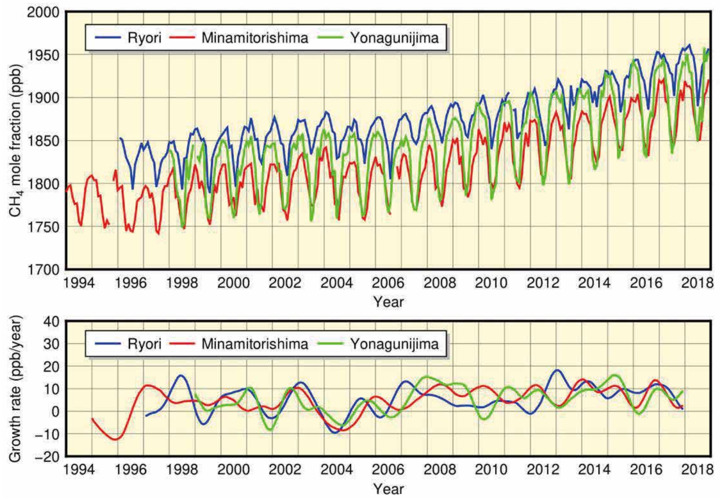

Figure 3.1-18 Monthly mean concentrations (a) and corresponding growth rates (b) of atmospheric CH_4 observed at Ryori (blue), Minamitorishima (red) and Yonagunijima (green)

The method for calculating the growth rate is described in WMO (2009).

3.1.3 Concentration of nitrous oxide

Figure 3.1-19 shows that the global mean concentration of atmospheric N_2O has been continuously increasing with small seasonal variations, in contrast to the situations with CO_2 and CH_4. The annual mean concentration in 2017 was 329.9 ppb, which was 22% above the pre-industrial level of 270 ppb (Table 3.1-1). The hemispheric mean concentration is approximately 1 ppb higher in the Northern Hemisphere than in the Southern Hemisphere (Figure 3.1-20) because there are more sources of anthropogenic and soil emissions in the former. This interhemispheric difference is, however, much smaller than those observed with CO_2 and CH_4.

The atmospheric N_2O concentration at Ryori exhibits characteristics similar to those of the global mean (Figure 3.1-21). The annual mean concentration in 2018 at Ryori was 332.7 ppb (based on preliminary estimations).

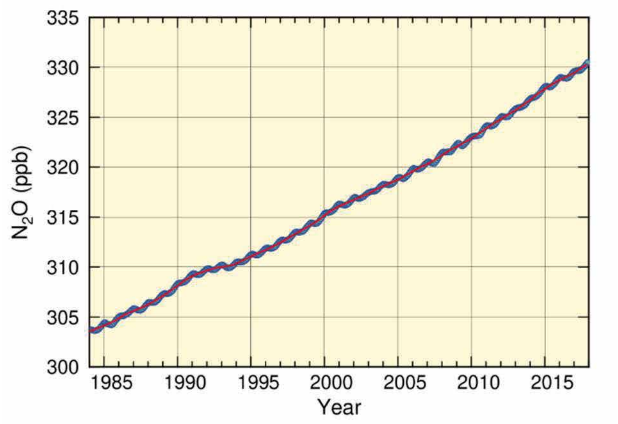

Figure 3.1-19 Global mean concentration of atmospheric N_2O

The blue dots are monthly values, and the red line represents the corresponding sequence after the removal of seasonal variations. Graph content is based on analysis of observation data reported to WDCGG based on the method of WMO (2009). Data contributors are listed in WMO (2019).

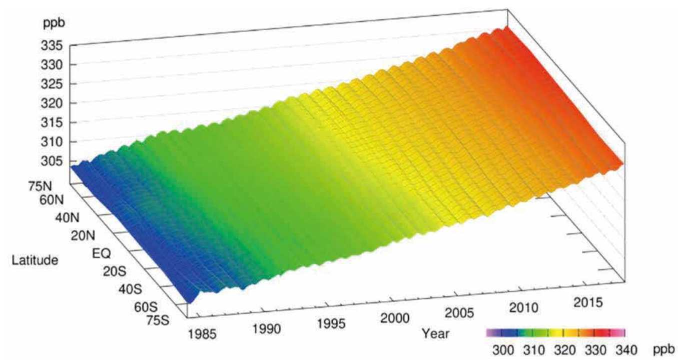

Figure 3.1-20 Latitudinal distribution of atmospheric N_2O concentrations

The data set and analysis method are as per Figure 3.1-19.

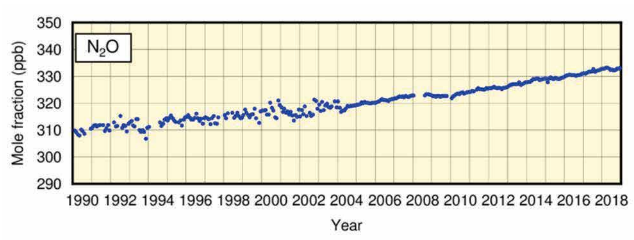

Figure 3.1-21 Monthly mean concentrations of atmospheric N_2O at Ryori

Improvement of observation equipment in 2004 resulted in improved stability of measurements.

3.2 Monitoring of the ozone layer and ultraviolet radiation[32]

- ○ Global-averaged total ozone amount decreased significantly in the 1980s and the early 1990s, and remains low today with a slightly increasing trend.
- ○ The annual maximum area of the ozone hole in the Southern Hemisphere increased substantially in the 1980s and 1990s, but a statistically significant decreasing trend since 2000 has been identified.
- ○ UV radiation levels at three domestic sites have increased since the early 1990s. Annual cumulative daily erythemal UV radiation at Tsukuba is virtually certain to have increased for the whole of the observational period at a rate of 4.5% per decade.
- ○ Global atmospheric concentrations of chlorofluorocarbons (CFCs) have gradually decreased in recent years.

JMA monitors total ozone and/or vertical profiles of ozone at three domestic sites and one Antarctic site (Sapporo, Tsukuba, Naha and Syowa Station) under the Act on the Protection of the Ozone Layer through the Control of Specified Substances and Other Measures[33]. It also monitors ultraviolet radiation at Tsukuba and Syowa. JMA also monitors the surface concentration of CFCs at Ryori (Figure 3.2-1).

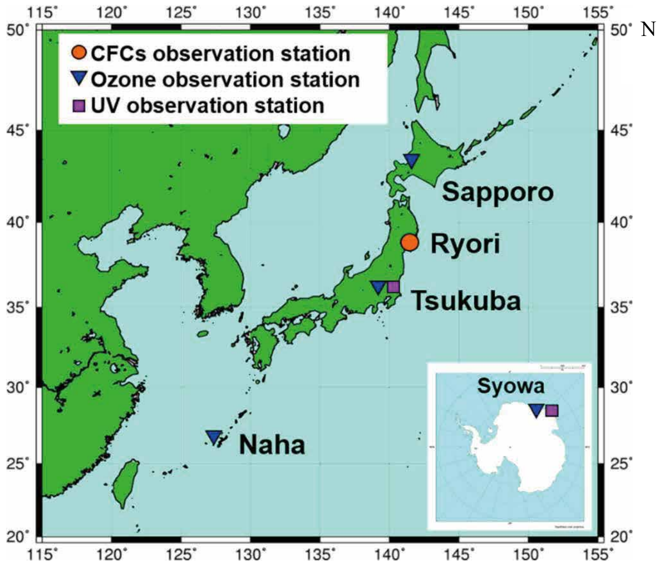

Figure 3.2-1 JMA's ozone layer and ultraviolet radiation observation network

3.2.1 Ozone layer

(1) Global ozone layer

Globally averaged total ozone amount decreased considerably in the 1980s and the early 1990s (Figure 3.2-2). Although uniformity or a slightly increasing trend has been observed since the mid-1990s, total ozone levels have remained lower than those seen before the 1980s. Global mean total ozone with enough data points for statistical analysis for the period 2013 – 2017 was approximately 1% higher than the 1994 – 2008 mean and 3% lower than the 1970 – 1980 mean, which is a representative value for the period prior to the onset of ozone depletion. A report titled

32 Information on the ozone layer and ultraviolet radiation is published on JMA's website.
https://www.data.jma.go.jp/gmd/env/ozonehp/en/diag_o3uv_e.html

33 Law No. 53 of May 20, 1988, Article 22: Observation and monitoring
1. The Director-General of the Meteorological Agency shall observe the state of the ozone layer and the atmospheric concentrations of specified substances and publish the results obtained.

Scientific Assessment of Ozone Depletion: 2018 (WMO, 2018a) stated that action taken under the Montreal Protocol has led to a reduction in the atmospheric abundance of controlled ozone-depleting substances (ODSs), and that upper-stratospheric ozone have increased since 2000.

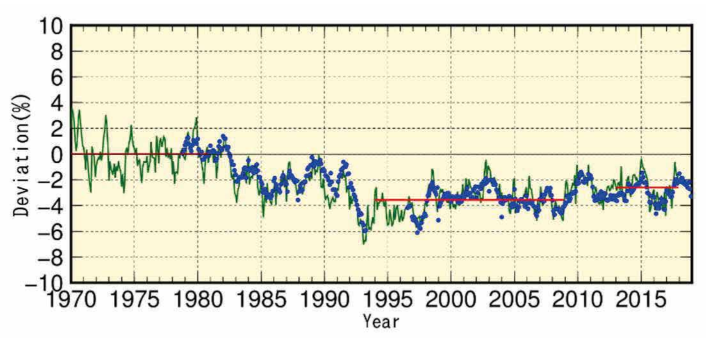

Figure 3.2-2 Time-series representation of global-averaged total ozone deviations shown as percentages
The green line represents deviations of monthly mean global-area-weighted total ozone from the 1970 – 1980 mean, the three red lines represent the 1970 – 1980 mean, the 1994 – 2008 mean and the mean over the last five years when there were enough data points for a statistical analysis (2013 – 2017), and the blue dots show NASA TOMS/OMI satellite data averaged at latitudes of 70°S – 70°N. Each data set is deseasonalized with respect to the whole observation period. A total of 114 ground-based stations were used for this calculation (91 in the Northern Hemisphere and 23 in the Southern Hemisphere).

(2) Antarctic ozone hole[34]

The annual maximum area of the ozone hole in 2018 exceeded the most recent decadal average due to very cold stratospheric conditions, but was smaller than those observed from the late 1990s to the early 2000s. The annual maximum area of the ozone hole in the Southern Hemisphere increased substantially in the 1980s and 1990s, but a statistically significant decreasing trend since 2000 has been identified as described in Topics II (The trend of Antarctic ozone layer recovery).

The annual ozone hole area depends on regional interannual climate variations, but also shows decadal variations in line with total amounts of ODSs in the stratosphere. A report titled *Scientific Assessment of Ozone Depletion: 2018* (WMO, 2018a) stated that the Antarctic ozone hole is expected to gradually close, with springtime total column ozone returning to 1980 values in the 2060s.

34 See the Glossary for terms relating to ozone hole.

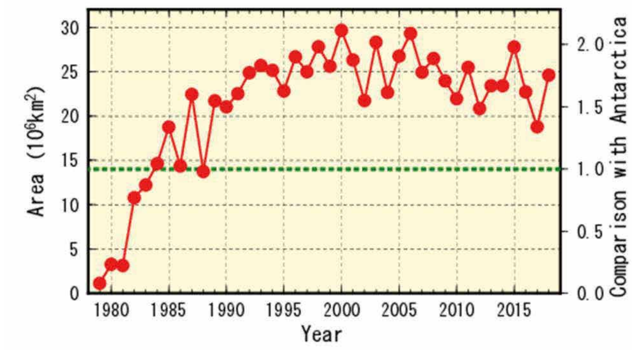

Figure 3.2-3 Time-series representation of the annual maximum ozone hole area

The ozone hole area is defined as the region over which total ozone south of 45°S is equal to or less than 220 m atm-cm. NASA TOMS/OMI and NOAA-TOVS satellite data are used in calculation of the area for 1979 – 2018. The green line indicates the overall area of the Antarctic (1.39×10^7 km^2). The left axis shows the ozone hole's maximum area in units of 10^6 km^2, and the right axis shows its ratio to the area of Antarctica itself.

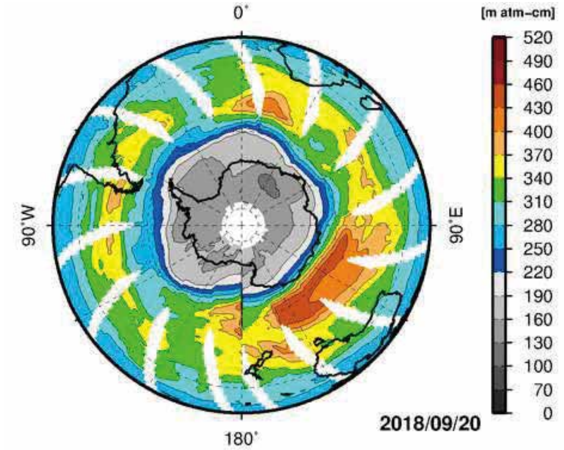

Figure 3.2-4 Southern Hemisphere distribution of total ozone on 20 September 2018, when the area of the ozone hole reached its maximum for the year

The unit is m atm-cm, and the map is produced using NASA OMI satellite data. The grey shading in the center shows ozone hole areas where the total ozone column value is 220 m atm-cm or less. White regions are domains where no satellite data were available.

(3) Ozone layer over Japan

Figure 3.2-5 shows time-series representations of annual-mean total ozone observed at Sapporo, Tsukuba and Naha. A decrease is seen in the 1980s and the early 1990s at Sapporo and Tsukuba. After 2000, slightly increasing trends are observed at all three sites, but an ongoing trend of relatively low values has been seen in recent years at Naha.

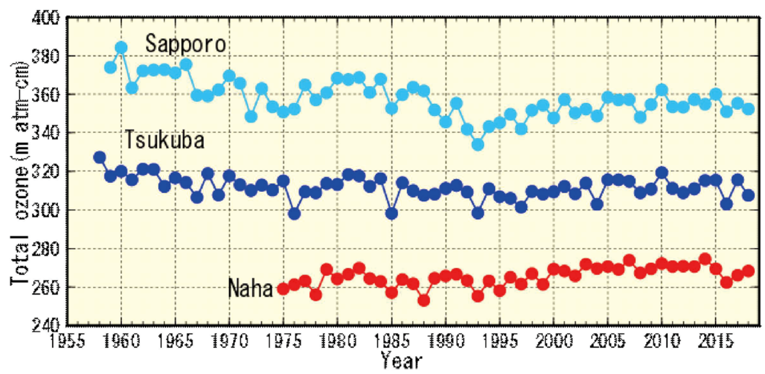

Figure 3.2-5 Time-series representations of annual-mean total ozone at stations in Japan

The stations here are at Sapporo, Tsukuba and Naha. JMA began observing total ozone at Tsukuba in 1957 and currently monitors total ozone and/or vertical profiles of ozone at three domestic sites (Sapporo, Tsukuba, Naha) and one Antarctic site (Syowa Station).

3.2.2 *Solar UV radiation in Japan*

UV radiation levels at three domestic sites have been increased from early-1990s. Annual cumulative daily erythemal UV radiation[35] at Tsukuba is virtually certain to have increased for the whole of the observational period by ratios of 4.5% per decade (Figure 3.2-6). At Sapporo, UV radiation levels increased from the mid-1990s to the 2000s. At Tsukuba, UV radiation levels increased in 1990s. At Naha, data show no marked changes since the increase observed in the 1990s. This phenomenon may be attributable to a decreasing tendency of aerosols and air pollution, and/or to changes in cloudiness and other meteorological conditions over monitoring sites (UNEP, 2015; JMA, 2011).

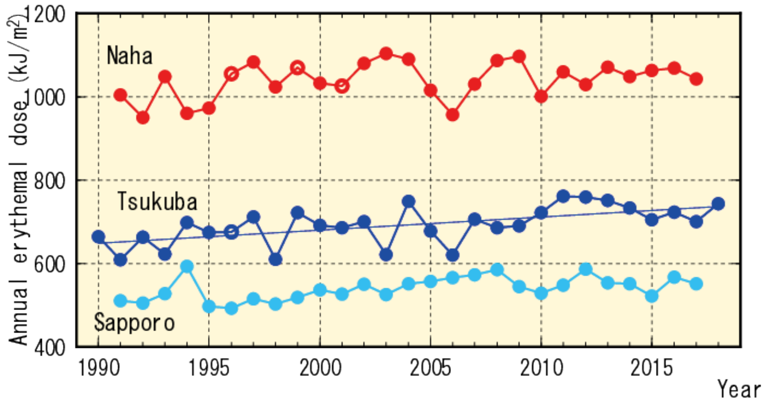

Figure 3.2-6 Time-series representations of annual cumulative daily erythemal UV radiation

Observation of erythemal UV at Sapporo, Tsukuba and Naha in Japan started in the early 1990s. Each annual cumulative total is calculated from monthly-mean equivalent values multiplied by the number of days in each month. The monthly-mean equivalent value is based on calculation using daily values from which missing data are excluded. Open circles represent cases of at least a month in which there are fewer than 20 days of monitoring data. Regression lines cover the whole observation period (statistically significant at a confidence level of 99% for Tsukuba). UV radiation observations at Sapporo and Naha were terminated in January 2018.

3.2.3 *Concentration of ozone-depleting substances*

Chlorofluorocarbons (CFCs: CFC-11, CFC-12 and CFC-113), which are compounds of carbon, fluorine and chlorine, and other halogenated gases are ozone-depleting substances (ODSs). They are regulated under the 1987 Montreal Protocol on Substances that Deplete the Ozone Layer and its Amendments and Adjustments. Although ODSs have atmospheric concentrations equivalent to about a millionth of CO_2 levels at most, they contribute considerably to global warming because of their significant radiative effects per unit mass, some of which are several thousand times greater than that of CO_2.

(1) Global concentration of ozone-depleting substances

Global concentrations of atmospheric CFCs increased rapidly until the 1980s before entering a decreasing trend in the 1990s (Figure 3.2-7). The concentration of CFC-11 peaked in 1992 – 1994, and has since shown a decreasing tendency. The concentration of CFC-12 increased until around 2003, and has also since shown a decreasing tendency. The concentration of CFC-113 reached its maximum in around 1993 in the Northern Hemisphere and around 1996 in the Southern Hemisphere. Differences in the concentrations of these gases between the Northern Hemisphere, where most emissions sources are located, and the Southern Hemisphere, which has significantly fewer sources, have decreased since the 1990s in contrast to the situation of the 1980s. These observations indicate that the CFC emission controls under the Montreal Protocol have been effective.

---

35 See the Glossary for terms relating to erythemal UV radiation.

However, a slowdown in the decline of CFC-11 concentrations has been observed since 2012 (WMO, 2018a; WMO, 2018b; Montzka *et al*., 2018), with decreasing rate approximately two thirds of those seen in the preceding decade. Numerical model calculation reporting by Montzka *et al*. (2018) attributed this to increased global CFC-11 emissions with main sources probably located in eastern Asia.

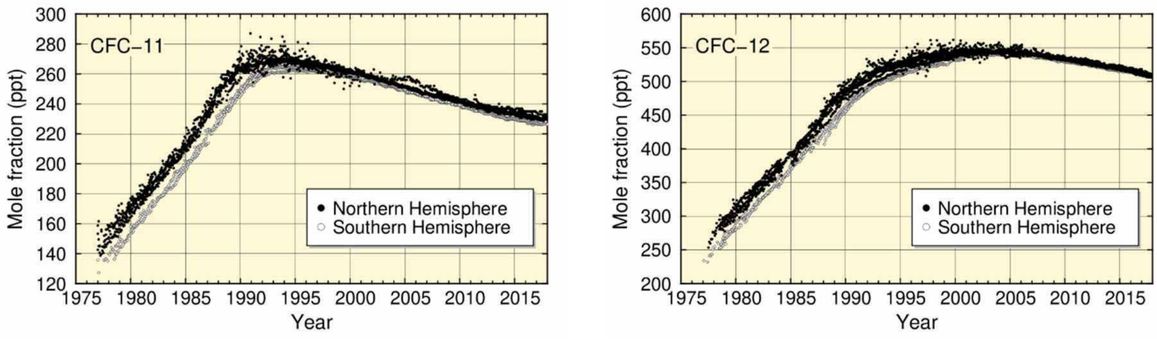

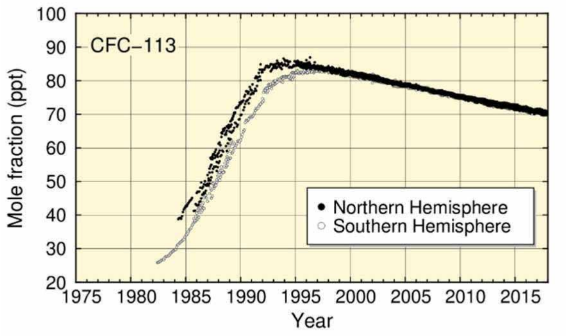

Figure 3.2-7 Monthly mean concentrations of CFC-11 (upper left), CFC-12 (upper right) and CFC-113 (lower left)

Graph content is based on monthly mean values reported to WDCGG. Dots and circles correspond to observation points in the Northern/Southern Hemisphere, respectively. Data contributors are listed in WMO (2019).

(2) Concentration of ozone-depleting substances in Japan

Concentrations of CFC-11, CFC-12 and CFC-113 at Ryori have shown decreasing tendencies since reaching maxima in various years (Figure 3.2-8). The concentration of CFC-11 peaked at about 270 ppt in 1993 – 1994, and has since decreased. The distinct peak of concentration observed in summer 2011 is considered attributable to emissions from polyurethane foam insulation materials released by the Great East Japan Earthquake and the subsequent hugely destructive tsunami of 11 March 2011 (Saito *et al*., 2015). The rate of increase in CFC-12 concentration slowed around 1995, and a gradual decrease has been seen since 2005. There was no clear tendency of increase or decrease in the concentration of CFC-113 until 2001, but a decreasing tendency has been seen since then.

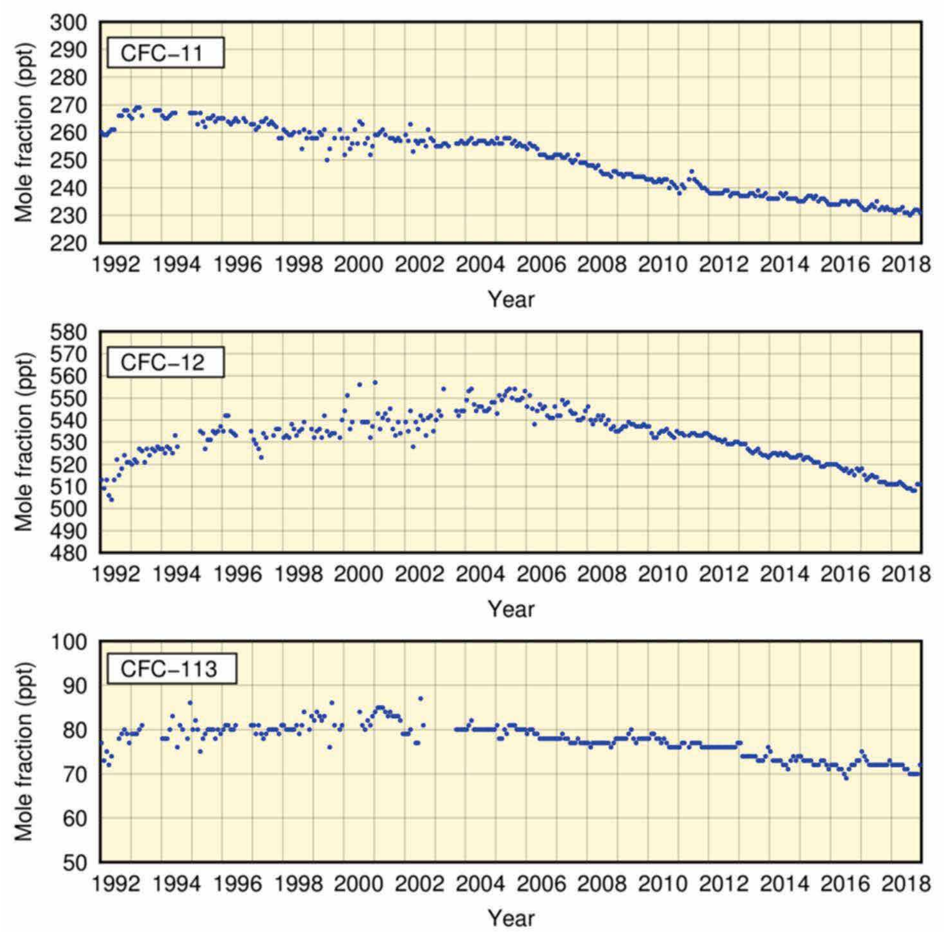

Figure 3.2-8 Monthly mean atmospheric concentrations of CFC-11 (top), CFC-12 (middle) and CFC-113 (bottom) at Ryori

Improvement of observation equipment in 2003 resulted in improved stability of measurements.

3.3 Monitoring of aerosols and surface radiation[36]

○ In Japan, background atmospheric turbidity coefficient values (which depend on concentrations of aerosols, water vapor and other constituents in the air) have returned to approximate levels seen before the eruption of Mt. Agung in 1963. This is mainly because of no large-scale eruptions impacting the global climate since that of Mt. Pinatubo in 1991.

○ The number of days when any meteorological station in Japan observed Kosa was 11 in 2018, and the total number of stations reporting its occurrence during the year was 104.

3.3.1 Aerosols

Interannual variations in the atmospheric turbidity coefficient[37], which is calculated from direct solar radiation[38] measurements taken at five stations in Japan excluding the fluctuation component of the troposphere, shows a clear impacts of stratospheric aerosols resulting from volcanic eruptions (Figure 3.3-1). The increased turbidity coefficients observed for several years after 1963 and during the periods of 1982 – 1983 and
1991 – 1993 were caused by the eruptions of Mt. Agung (Indonesia) in 1963, Mt. El Chichón (Mexico) in 1982 and Mt. Pinatubo (Philippines) in 1991, respectively. The increased turbidity stems from the persistent presence of sulfate aerosol in the stratosphere resulting from huge amounts of SO_2 released by the volcanic eruptions. The turbidity coefficient has now returned to approximately the same level as that observed before the eruption of Mt. Agung because no large-scale eruptions have occurred since that of Mt. Pinatubo.

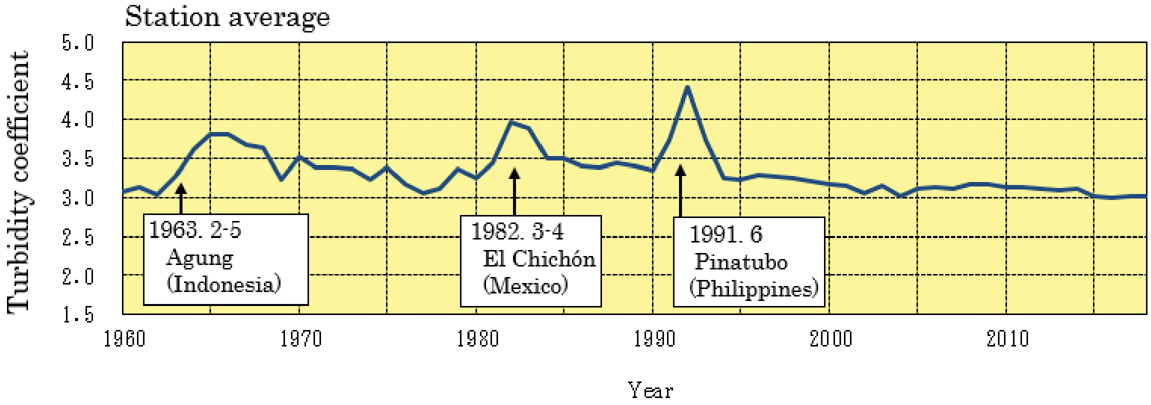

Figure 3.3-1 Time-series representation of annual mean atmospheric turbidity coefficients (1960 – 2018)
To eliminate the influence of variations in tropospheric aerosols such as water vapor, dust and air pollutants, the annual mean atmospheric turbidity coefficient is calculated using the minimum turbidity coefficient for each month.

36 See the Glossary for terms relating to aerosols.
Information on aerosols and Kosa is published on JMA's website.
https://www.jma.go.jp/en/kosa/ (Prediction and observation of Kosa)

37 The atmospheric turbidity coefficient indicates the ratio of the atmospheric optical depth affected by aerosols, water vapor and gases in the atmosphere to that uninfluenced by constituents other than air molecules such as oxygen and nitrogen in the atmosphere. Larger values indicate greater amounts of turbid matter in the air.

38 Direct solar radiation is the incident solar energy acting on the earth's surface from the sun. The atmospheric turbidity coefficient (also known as the Feussner-Dubois turbidity coefficient) can be calculated from direct solar radiation amounts.

3.3.2 Kosa (Aeolian dust)

Kosa (Aeolian dust) is a kind of aerosols that are blown up from semi-arid areas of the Asian continent and transported by westerly winds to Japan. A total of 59 JMA meteorological stations (as of 31 December 2018) perform Kosa monitoring. The phenomenon is recorded when visually observed by station staff. The number of days when any meteorological station in Japan observed Kosa was 11 in 2018 (Figure 3.3-2), and the total number of stations reporting its occurrence during the year was 104 (Figure 3.3-3).

The number of days on which Kosa is observed and the annual total number of stations reporting the phenomenon show large interannual variability. As a result, the long-term trend of occurrence remains unclear.

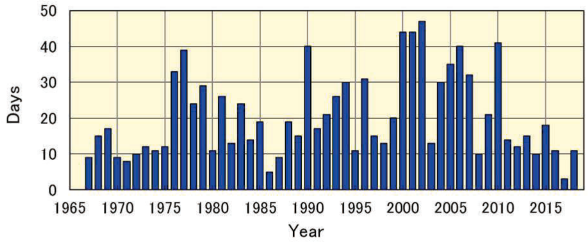

Figure 3.3-2 Number of days when any station in Japan observed Kosa (1967 – 2018) based on the 59 stations that were active for the whole period

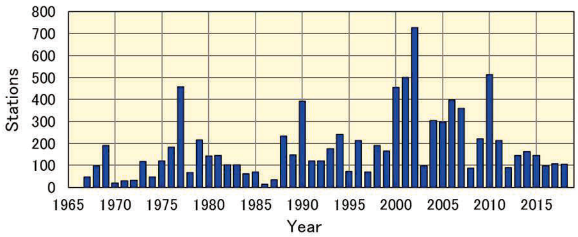

Figure 3.3-3 Annual total number of stations observing Kosa in Japan (1967 – 2018) based on the 59 stations that were active for the whole period

3.3.3 Solar radiation and downward infrared radiation

The earth's radiation budget is a source of energy for climate change, and monitoring of its variations is important. To this end, JMA conducts measurements of direct solar radiation, diffuse solar radiation and downward infrared radiation[39] at five stations in Japan (Sapporo, Tsukuba, Fukuoka, Ishigakijima and Minamitorishima) (Figure 3.3-4).

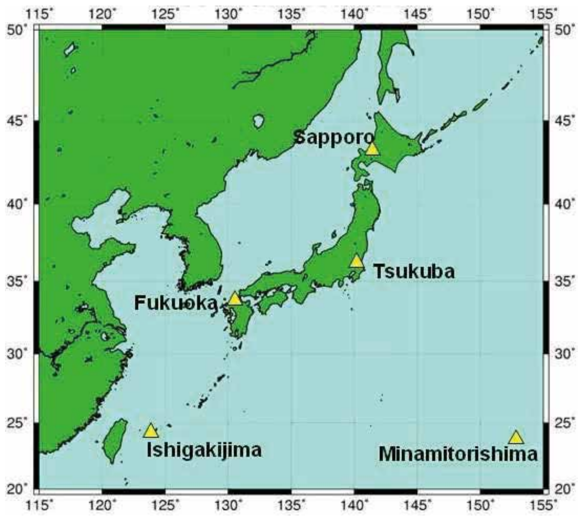

Figure 3.3-4 JMA's solar radiation and infrared radiation observation network

JMA conducts observation of direct solar, diffuse solar and downward infrared radiation at five stations (Sapporo, Tsukuba, Fukuoka, Ishigakijima and Minamitorishima).

39 Downward infrared radiation is the incident infrared radiation acting on the earth's surface from all directions in the sky. It is emitted from clouds and atmospheric constituents such as water vapor and carbon dioxide in proportion to the fourth power of their temperature, and can be used as an index of global warming.

(1) Global solar radiation

Reports indicate that global solar radiation decreased from around 1960 to the late 1980s before increasing rapidly from the late 1980s to around 2000, and no obvious changes have been observed in most regions of the world (Ohmura, 2009).

In Japan, global solar radiation declined rapidly from the late 1970s to around 1990 before increasing rapidly from around 1990 to the early 2000s. Since then, data from measurements at the five observation stations show no obvious changes. These long-term variations are consistent with those reported globally (Figure 3.3-5). Variations are considered to stem mainly from changes in anthropogenic aerosols in the atmosphere, and to be partly attributed to changes in cloud cover and cloud characteristics (Wild, 2009). Norris and Wild (2009) quantitatively estimated the cause of the rapid increase in global solar radiation observed in Japan from around 1990 to the beginning of the 2000s. According to their estimates, two thirds of the increase was due to reduced anthropogenic aerosols in the atmosphere and the other third was due to reduced cloud cover. These results imply that the presence of anthropogenic aerosols has a profound effect on solar radiation variations. Results produced by Kudo et al. (2012) indicated that the solar radiation increase was mainly caused by changes in the optical characteristics of aerosols due to changes in the aerosol composition of the atmosphere.

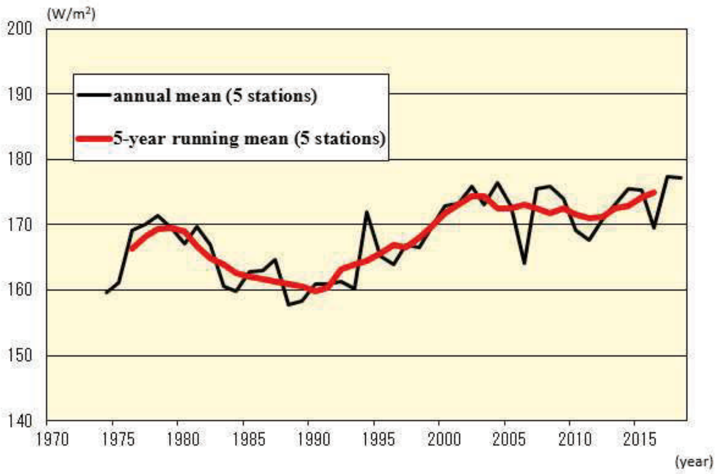

Figure 3.3-5 Time-series representations of annual and five-year-running means of global solar radiation at five stations in Japan (Sapporo, Tsukuba, Fukuoka, Ishigakijima and Minamitorishima)

(2) Downward infrared radiation

Atmospheric concentrations of carbon dioxide and other greenhouse gases, which cause global warming, show increasing yearly trends. Observation of downward infrared radiation is effective for the evaluation of global warming because signals of global warming due to increased greenhouse gases are seen more clearly from increased downward infrared radiation than from increased surface temperatures. While general circulation model experiments suggest that two decades of downward infrared radiation monitoring are necessary to detect statistically significant increases with a confidence level of 95%, analysis of in situ observation data covering about a decade has shown an overall increase (Wild and Ohmura, 2004).

In Japan, downward infrared radiation has been monitored since the early 1990s at Tsukuba. Analysis of the data obtained shows an increasing trend at a rate of about 0.3 W/m^2 per year during the period from 1993 to 2018 (Figure 3.3-6). This is consistent with the trend seen in the results of analysis using data from 20 BSRN[40] stations worldwide (+0.3 W/m^2 per year during the period from 1992 to 2009) (WCRP, 2010).

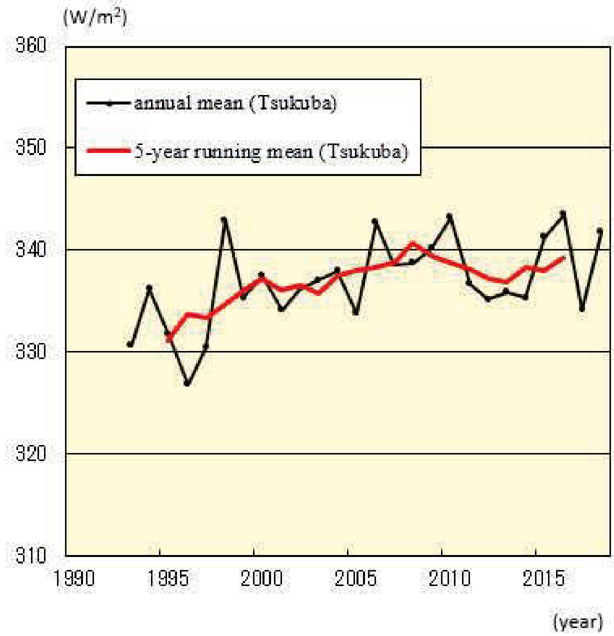

Figure 3.3-6 Time-series representations of annual and five-year-running means of downward infrared radiation at Tsukuba

40 The BSRN (Baseline Surface Radiation Network) is a global observation network for measuring high-precision surface radiation balance on an ongoing basis. JMA operates five BSRN stations in Japan (Sapporo, Tsukuba, Fukuoka, Ishigakijima and Minamitorishima) and one in Antarctica (Syowa Station).

Explanatory note on detection of statistical significance in long-term trends

Meteorological observation data, including those relating to temperature and precipitation, are subject to large amplitude fluctuations due to the influence of atmospheric and oceanic dynamics on a broad spectrum of spatial and temporal scales. To examine the possible presence of long-term climate system trends associated with global warming in consideration of natural variability, raw climate data need to be converted into suitable statistical time-series representations and subjected to statistical testing in order to highlight the likelihood of systematic temporal trends that cannot be explained by random variability alone. When the results of such testing allow reasonable conclusion that random variability is unlikely to be the sole factor at work, a change is described as statistically significant.

In this report, the likelihood of a systematic long-term change existing in a time-series representation is based on the results of statistical significance testing performed at confidence levels of 99, 95 and 90%. The following terminology summary describes each level:

Level of confidence	Term
≥ 99%	**Virtually certain** to have increased/decreased (statistically significant at a confidence level of 99%)
≥ 95%	**Extremely likely** to have increased/decreased (statistically significant at a confidence level of 95%)
≥ 90%	**Very likely** to have increased/decreased (statistically significant at a confidence level of 90%)
< 90%	No discernible trend

The following statistical methods are applied for the data used in this report:

i) For statistical variables whose annual fluctuation component can be assumed to follow normal distribution

For temperature anomalies, trend-removed annual variability data are expected to approximately follow normal distribution. T-testing is performed for statistical variables assumed to be normally distributed using a coefficient of correlation between years and values.

ii) For statistical variables whose annual fluctuation component cannot be assumed to follow normal distribution

The assumption of normality may not be applicable to frequency statistics regarding weather conditions, including those for extremely warm days, tropical nights and hourly precipitation amounts exceeding 50 mm. Accordingly, non-parametric testing, which does not depend on underlying assumptions about distribution, is applied to such variables.

It should be noted that statistical tests are in theory inevitably susceptible to the establishment of false conclusions even if the results indicate a statistically significant trend. Even outcomes indicating statistical significance at confidence levels of 90, 95 or 99% imply that there are small inherent probabilities of up to 10, 5 and 1%, respectively, of the significance being erroneously detected when in fact the observed long-term change occurred by mere random chance. Conversely, when a systematic long-term change actually exists, statistical testing may fail to detect the significance correctly. In general, test results are not considered highly stable if they are based on observation records that are temporally limited, influenced by large annual fluctuations/rare events or subject to change when new observations are added to a data sequence. Readers are encouraged to interpret the analytical results presented in the report appropriately with due note of these considerations.

Glossary

Aerosols

Aerosols are airborne solids or liquids in fine particle form. Their many types include particles of natural origin blown up from land/sea surfaces, anthropogenic particles and secondary aerosols formed from anthropogenic and biogenic precursors. In addition to absorbing and scattering sunlight, they also provide condensation nuclei for clouds. Particulate matter 2.5 (PM2.5) is the name given to aerosol particles measuring 2.5 micrometers or less in diameter (about 30 times thinner than a human hair), and is considered to have possible adverse effects on human health when inhaled.

Anthropogenic

Resulting from or produced by human activity.

Arctic Oscillation

The Arctic Oscillation (AO) is a major atmospheric circulation variation exhibiting an annular pattern of sea-level pressure anomalies in a seesaw fashion with one sign over the Arctic region and the opposite sign over the mid-latitudes. Its negative phase, which is characterized by positive and negative sea-level pressure anomalies over the Arctic region and the mid-latitudes, respectively, helps cold Arctic air move into the mid-latitudes. The positive phase, whose sea-level pressure anomaly pattern is reversed, keeps Arctic air over the Arctic region.

Erythemal UV radiation

Erythema is sunburn – a reddening of the skin resulting from continuous exposure to ultraviolet (UV) rays present in solar radiation. It is known that excessive erythema and long-term exposure to the sun can cause human health problems such as a high incidence of skin cancer and cataracts. Erythemal UV radiation is widely used as a scale of UV radiation for evaluation of its effects on the human body, and is calculated in consideration of various influences depending on wavelength.

Extreme climate event

In general, an extreme climate event is recognized as an unusually severe or rare climate event creating disaster conditions or exerting significant socio-economic influence. The definition includes severe weather conditions covering periods ranging from only a few hours (such as heavy rain or strong wind) to several months (such as drought or cold summer conditions). JMA defines extreme climate events as those occurring once every 30 years or longer.

IPCC (Intergovernmental Panel on Climate Change)

The Intergovernmental Panel on Climate Change (IPCC) is an international organization established by the United Nations Environment Programme (UNEP) and the World Meteorological Organization (WMO) in 1988. It reviews and assesses scientific, technical and socio-economic information on climate change, the potential impacts of such change and related vulnerability, and options for adaptation and mitigation, in collaboration with scientists and experts on an international basis. The Panel's reports highlight common understanding of such information to support political matters such as treaty negotiations on global warming.

Kosa (Aeolian dust)

Kosa (Aeolian dust) is a meteorological phenomenon in which fine dust is blown up to an altitude of several thousand meters by cyclonic or other wind systems from deserts or cropland in semi-arid areas of the Asian continent, and is transported over long distances by westerly winds, resulting in haze or dustfall in downstream areas. It is often observed between March and June in Japan and makes the sky yellow and hazy. Heavy Kosa can affect transportation by obstructing visibility.

Monsoon

The term *monsoon* primarily refers to seasonally reversing winds, and by extension includes related seasonal rainfall change with wet and dry phases. Monsoon climate regions where seasonal winds prevail are found in numerous places around the world, with a major one located over a broad area from the Asian continent to northern Australia.

Normals

Normals represent climatic conditions at meteorological stations, and are used as a base to evaluate meteorological variables (e.g., temperature, precipitation and sunshine duration) and produce generalizations (e.g., cool summer, warm winter and dry/wet months) for particular periods. JMA uses averages for the most recent three decades (currently 1981 – 2010) as normals, which are updated every decade in line with WMO Technical Regulations.

Terms relating to surface temperature variations

El Niño/La Niña events: In an El Niño event, sea surface temperatures (SSTs) are higher than normal across a wide region from near the date line to the area off the coast of South America in the equatorial Pacific for about a year. In a La Niña event, SSTs are lower than normal in the same area. Both occur every few years, and are associated with frequent extreme climate conditions worldwide.

JMA recognizes the occurrence of an El Niño event when the five-month running mean of SST deviations from the climatological means (based on a sliding 30-year period averaged over the NINO.3 El Niño Monitoring Region (5ºN – 5ºS, 150ºW – 90ºW; Figure A)) remains +0.5°C or above for a period of six months or more. Similarly, a La Niña event is recognized when the corresponding figure is −0.5°C or below for the same area/period.

Figure B shows typical SST deviations from the normal during El Niño and La Niña events. The dark red and blue shading seen from the date line to the coast of South America indicates large deviations.

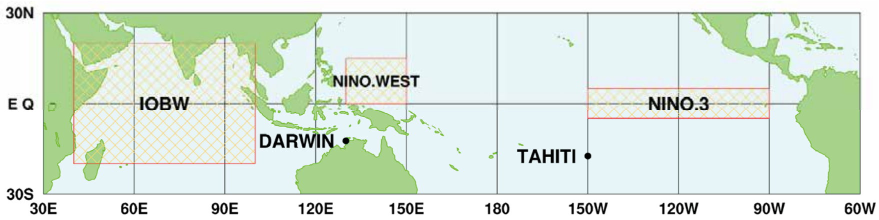

Figure A El Niño monitoring regions

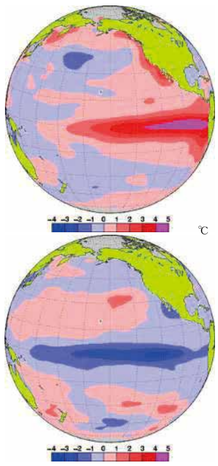

Figure B Left: monthly mean SST anomalies for El Niño (November 1997); right: for La Niña (December 1998)

Red and blue shading represents positive and negative SST deviations, respectively. Darker shading indicates larger deviations. The unit of temperature is degrees Celsius.

Southern Oscillation: El Niño and La Niña events are closely related to trade winds (easterlies blowing around the tropical Pacific), which tend to be weak during the former and strong during the latter. The strength of such winds is closely related to the sea level pressure difference between eastern and western parts of the Pacific. This pressure difference varies in a phenomenon known as the Southern Oscillation. El Niño/La Niña events and the Southern Oscillation are not independent of each other; they are different manifestations of the same phenomenon involving atmospheric and oceanic interaction, and are referred to as ENSO (El Niño – Southern Oscillation) for short.

Pacific Decadal Oscillation (PDO): A phenomenon in which variables in the atmosphere and oceans tend to co-vary with a period of more than ten years in the North Pacific. When sea surface temperatures are lower (higher) than their normals in the central part of the North Pacific, those in its part along the coast of North America are likely to be higher (lower) than their normals, and sea level pressures in the high latitudes of the North Pacific are likely to be lower (higher) than their normals. These atmospheric variations affect meteorological conditions in North America and elsewhere.

Terms relating to the greenhouse effect

Greenhouse effect: The earth's atmosphere contains small amounts of greenhouse gases, which absorb a large part of the infrared radiation emitted from the earth's surface and re-emit it back, thereby warming the surface. This process is known as the greenhouse effect. Without it, the earth's average surface temperature of around 14°C would be approximately −19°C. Increased concentrations of greenhouse gases enhance the greenhouse effect, thereby producing higher surface temperatures. Major greenhouse gases include carbon dioxide, methane and nitrous oxide. Although water vapor has the strongest greenhouse effect, it is not usually regarded as a greenhouse gas in the context of global warming because the amount of water vapor on a global scale is not directly affected by human activity.

Carbon dioxide: Of all greenhouse gases, carbon dioxide (CO_2) is the most significant contributor to global warming. Since the start of the industrial era in the mid-18th century, its atmospheric concentration has increased as a result of emissions associated with human activity, such as fossil fuel combustion, cement production and deforestation. Around half of all cumulative anthropogenic CO_2 emissions have remained in the atmosphere. The rest was removed from the atmosphere and stored in natural terrestrial ecosystems and oceans (IPCC, 2013).

Methane: Methane (CH_4) is the second most significant greenhouse gas after CO_2, and is emitted into the atmosphere from various sources including wetlands, rice paddy fields, ruminant animals, natural gas production and biomass combustion (WMO, 2018b). It is primarily removed from the atmosphere via photochemical reaction with reactive and unstable hydroxyl (OH) radicals.

Nitrous oxide: Nitrous oxide (N_2O) is a significant greenhouse gas because of its large radiative effect per unit mass (about 300 times greater than that of CO_2) and its long lifetime (about 121 years) in the atmosphere. It is emitted into the atmosphere by elements of nature such as soil and the ocean, and as a result of human activity such as the use of nitrate fertilizers and various industrial processes. It is photo-dissociated in the stratosphere by ultraviolet radiation.

ppm, ppb, ppt: In this report, greenhouse gas concentrations are described in terms of mole fractions in units of ppm/ppb/ppt, representing the numbers of molecules of the gas per million/billion/trillion molecules of dry air, respectively.

Terms relating to the ozone layer

Total ozone: Total ozone at any location on the globe is defined as the sum of all ozone in the atmosphere directly above that location, and is often reported in m atm-cm or Dobson units. The unit of m atm-cm (read as "milli-atmosphere centimeters") indicates the columnar density of a trace gas (ozone) in the earth's atmosphere. A value of 1 m atm-cm represents a layer of gas that would be 10 μm thick under standard temperature and pressure conditions. For example, 300 m atm-cm of ozone brought down to the earth's surface at 0°C would occupy a layer 3 mm thick. Typical values of total ozone vary between 200 and 500 m atm-cm over the globe, and the global mean is about 300 m atm-cm.

Ozone-depleting substances: Ozone-depleting substances (ODSs) are those that deplete the ozone layer as listed in the Montreal Protocol, which bans their production. Major ODS species include chlorofluorocarbons (CFC-11, CFC-12 and CFC-113 among others), carbon tetrachloride, hydrochlorofluorocarbons (HCFCs), 1,1,1-trichloroethane, chloromethane, halons and bromomethane. These are also powerful greenhouse gases that trap heat in the atmosphere and contribute to global warming.

Ozone hole: The phenomenon referred to as the ozone hole is a reduction in the concentration of ozone high above the earth in the stratosphere over the Antarctica. For simplicity, it is often regarded as the area in which the total ozone amount is equal to or less than 220 m atm-cm to the south of the southern latitude of 45 degrees. The hole has steadily grown in size and annual length of presence (from August to December) over the last two decades of the last century.

Montreal Protocol: The Montreal Protocol on Substances that Deplete the Ozone Layer (a protocol to the Vienna Convention for the Protection of the Ozone Layer) is an international treaty designed to protect the ozone layer by phasing out the production of numerous substances believed to be responsible for ozone depletion. The treaty was opened for signatures in 1987 and came into force in 1989. Since then, it has undergone several revisions. Japan ratified the protocol in 1988.

Terms relating to water masses

North Pacific Subtropical Mode Water (NPSTMW) area: A thermostad between the seasonal and main thermoclines. The NPSTMW area is considered to form in the surface mixed layer just south of the Kuroshio Extension as a result of huge heat loss in winter. It is defined as an area of 16 – 18-degree water at depths of 100 to 400 m at around 20 to 30°N along the 137°E line.

North Pacific Intermediate Water (NPIW) area: The NPIW area forms in the mixed region between the Kuroshio Extension and the Oyashio front. It is defined as water with a salinity level of 34.0 or less at a depth of around 800 m at around 20 to 30°N along the 137°E line.

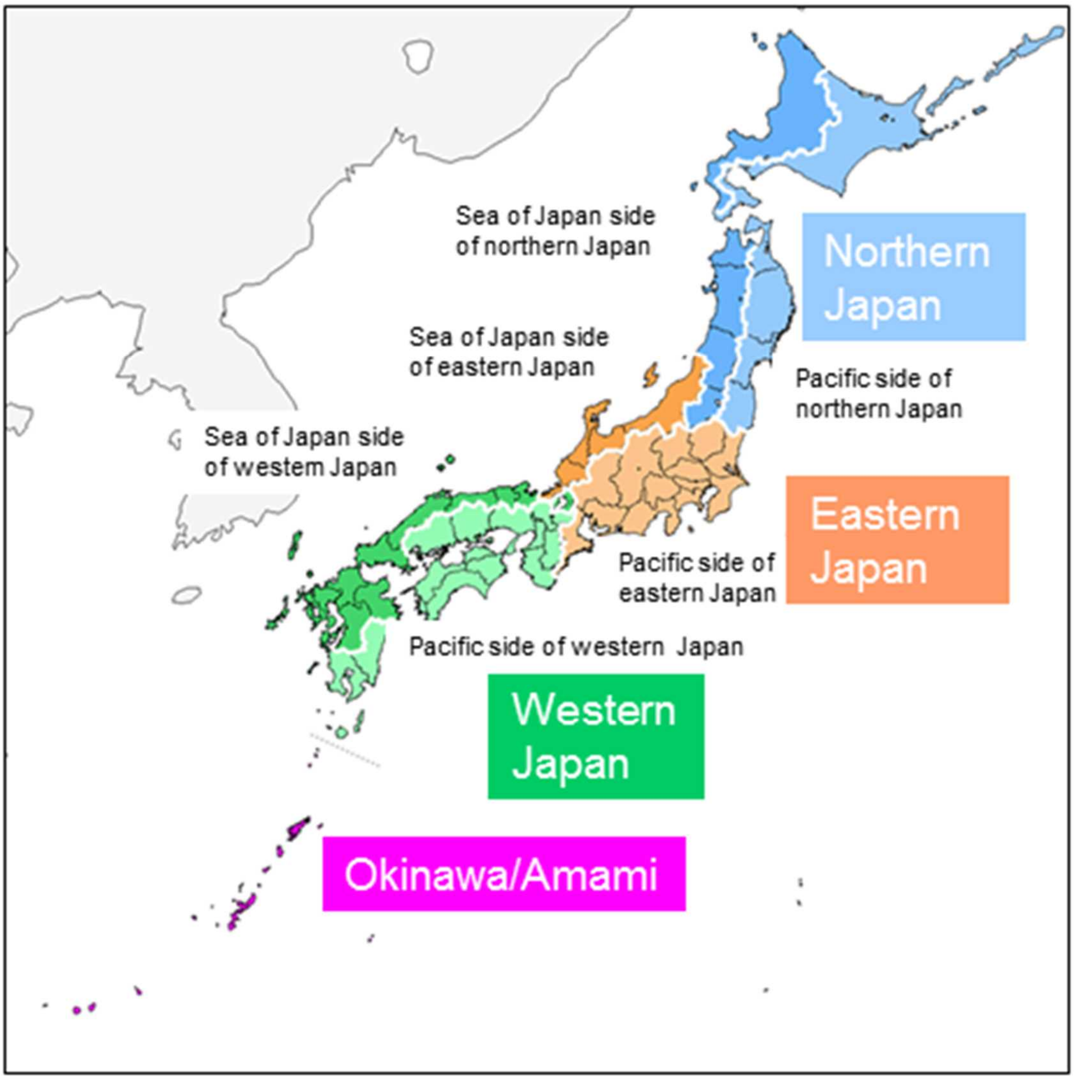

Names of Japanese regions used in this report

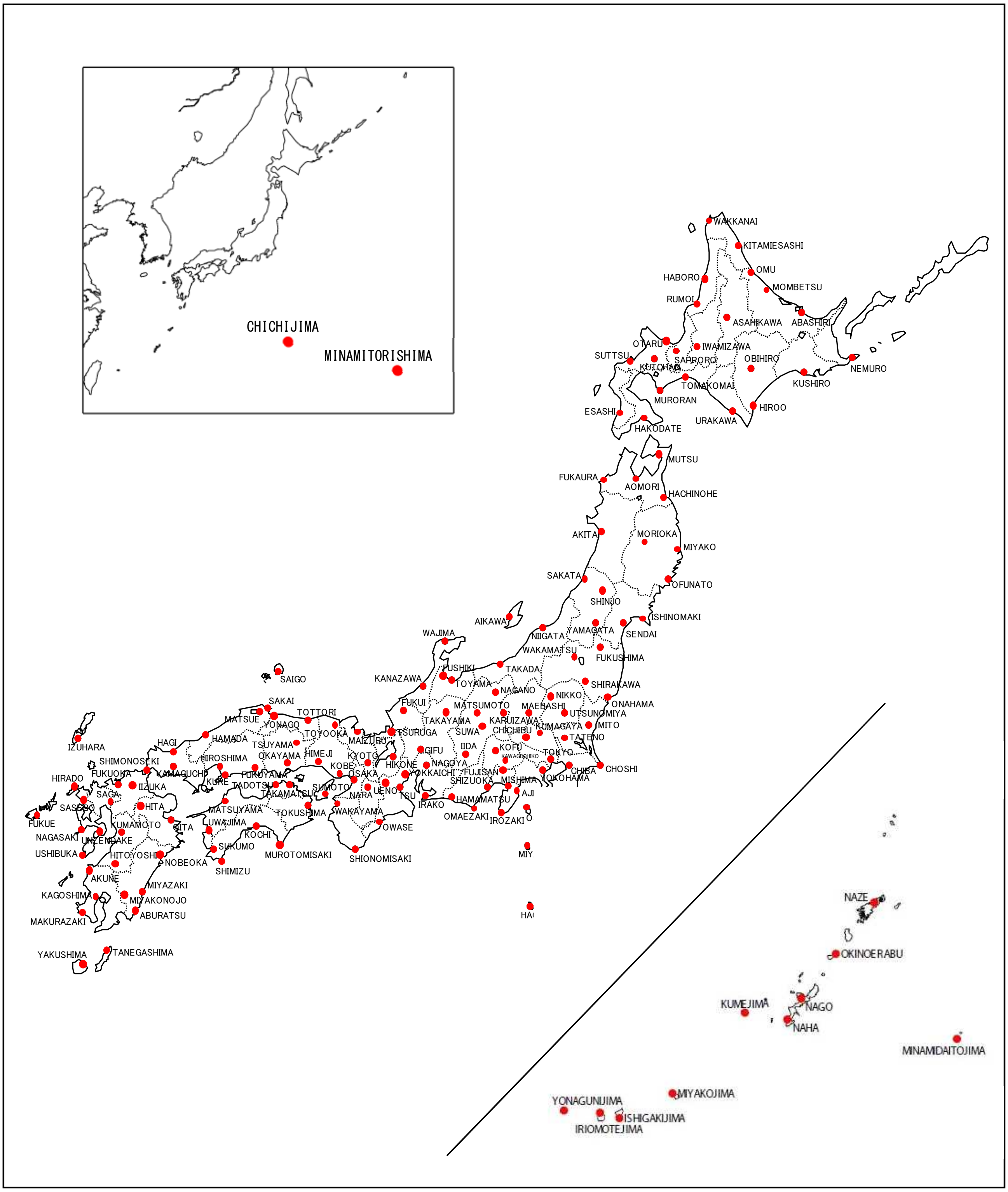

Distribution of surface meteorological observation stations in Japan

References

Topics

Kosaka, Y., and H. Nakamura, 2010: Mechanisms of meridional teleconnection observed between a summer monsoon system and a subtropical anticyclone. Part I: The Pacific-Japan pattern. J. Climate, 23, 5085 – 5108.

Nitta, T., 1987: Convective activities in the tropical western Pacific and their impact on the Northern Hemisphere summer circulation. J. Meteor. Soc. Japan, 65, 373 – 390.

Chapter 1

EM-DAT: The OFDA/CRED International Disaster, Database – www.emdat.be – Université Catholique de Louvain – Brussels – Belgium

IPCC, 2013: Climate Change 2013: The Physical Science Basis. Contribution of Working Group I to the Fifth Assessment Report of the Intergovernmental Panel on Climate Change [Stocker, T.F., D. Qin, G.-K. Plattner, M. Tignor, S.K. Allen, J. Boschung, A. Nauels, Y. Xia, V. Bex and P.M. Midgley (eds.)]. Cambridge University Press, Cambridge, United Kingdom and New York, NY, USA, 1535 pp.

JMA, 1997: Monthly Report on Climate System, June 1997.

Chapter 2

IPCC, 2013: Climate Change 2013: The Physical Science Basis. Contribution of Working Group I to the Fifth Assessment Report of the Intergovernmental Panel on Climate Change [Stocker, T.F., D. Qin, G.-K. Plattner, M. Tignor, S.K. Allen, J. Boschung, A. Nauels, Y. Xia, V. Bex and P.M. Midgley (eds.)]. Cambridge University Press, Cambridge, United Kingdom and New York, NY, USA, 1535 pp.

Mantua, N. J. and S. R. Hare, 2002: The Pacific decadal oscillation. J. Oceanogr., 58, 35–44.

Trenberth, K. E., J. M. Caron, D. P. Stepaniak and S. Worley, 2002: The evolution of El Niño–Southern Oscillation and global atmospheric surface temperatures, J. Geophys. Res., 107, D8, doi: 10.1029/2000JD000298.

Chapter 3

Dettinger, M. D. and M. Ghil, 1998: Seasonal and interannual variations of atmospheric CO_2 and climate. Tellus, 50B, 1–24.

Doney, S. C., V. J. Fabry, R. A. Feely and J. A. Kleypas, 2009: Ocean acidification: The other CO_2 problem, Annu. Rev. Mar. Sci., 1, 169–192, doi:10.1146/annurev.marine.010908.163834.

Iida, Y., et al., 2015: Trends in $p$$CO_2$ and sea-air CO_2 flux over the global open oceans for the last two decades. J. Oceanogr. doi:10.1007/s10872-015-0306-4.

IPCC, 2013: Climate Change 2013: The Physical Science Basis. Contribution of Working Group I to the Fifth Assessment Report of the Intergovernmental Panel on Climate Change [Stocker, T.F., D. Qin, G.-K. Plattner, M. Tignor, S.K. Allen, J. Boschung, A. Nauels, Y. Xia, V. Bex and P.M. Midgley (eds.)]. Cambridge University Press, Cambridge, United Kingdom and New York, NY, USA, 1535 pp.

Ishii, M., et al, 2011: Ocean acidification off the south coast of Japan: A result from time series observations of CO2 parameters from 1994 to 2008, J. Geophys. Res., 116, C06022, doi:10.1029/2010JC006831.

JMA, 2011: Annual Report on Ozone Layer Monitoring (in Japanese).

Keeling, C. D., T. P. Whorf, M. Wahlen and J. van der Plicht, 1995: Interannual extremes in the rate of rise of atmospheric carbon dioxide since 1980. Nature, 375, 666–670.

Keeling, R. F., S. C. Piper, and M. Heinmann, 1996: Global and hemispheric CO_2 sinks deduced from changes in atmospheric O_2 concentration. Nature, 381: 218-221.

Kudo, R., et al, 2012: Aerosol impact on the brightening in Japan. J. Geophys. Res., 117(D07208), doi:10.1029/2011JD017158.

Le Quéré, C., et al., 2016: Global Carbon Budget 2016, Earth Syst. Sci. Data, 8, 605-649, doi:10.5194/essd-8-605-2016.

Le Quéré, C., et al., 2018: Global Carbon Budget 2018, Earth Syst. Sci. Data, 10, 2141-2194, doi:10.5194/essd-10-2141-2018.

Montzka, S. A. et al., 2018: An unexpected and persistent increase in global emissions of ozone-depleting CFC-11, Nature, 557, 413-417, doi:10.1038/s41586-018-0106-2.

Niwa, Y., et al, 2014: Seasonal Variations of CO_2, CH_4, N_2O and CO in the Mid-Troposphere over the Western North Pacific Observed Using a C-130H Cargo Aircraft. J. Meteorol. Soc. Japan, 92(1), 50-70, doi:10.2151/jmsj.2014-104.

Norris, J. R. and M. Wild, 2009: Trends in aerosol radiative effects over China and Japan inferred from observed cloud cover, solar ‘‘dimming,’’ and solar ‘‘brightening,’’. J. Geophys. Res., 114(D00D15), doi:10.1029/2008JD011378.

Ohmura, A., 2009: Observed decadal variations in surface solar radiation and their causes. J. Geophys. Res., 114(D00D05), doi: 10.1029/2008JD011290.

Rayner, P. J., I. G. Enting, R. J. Francey, and R. Langenfelds, 1999: Reconstructing the recent carbon cycle from atmospheric CO_2, $\delta^{13}C$ and O_2/N_2 observations. Tellus, 51B, 213-232.

Saito, T., et al, 2015: Extraordinary halocarbon emissions initiated by the 2011 Tohoku earthquake. Geophys. Res. Lett., 42, doi:10.1002/2014GL062814.

Sweeney, C., et al., 2015: Seasonal climatology of CO_2 across North America from aircraft measurements in the NOAA/ESRL Global Greenhouse Gas Reference Network, J. Geophys. Res. Atmos., 120, 5155-5190, doi:10.1002/2014JD022591.

Tsuboi, K., et al, 2013: Evaluation of a new JMA aircraft flask sampling system and laboratory trace gas analysis system. Atmos. Meas. Tech., 6, 1257–1270, doi:10.5194/amt-6-1257-2013.

Umezawa, T., et al, 2018: Seasonal evaluation of tropospheric CO_2 over the Asia-Pacific region observed by the CONTRAIL commercial airliner measurements, Atmos. Chem. Phys., 18, 14851-14866, doi:10.5194/acp-18-14851-2018.

UNEP, 2015: Environmental effects of ozone depletion and its interactions with climate change: 2014 assessment, 236pp.

WCRP, 2010: Summary Report from the Eleventh Baseline Surface Radiation Network (BSRN) Scientific Review and Workshop. WCRP Informal Report No. 08/2010, 21 pp.

Wild, M., 2009: Global dimming and brightening: A review. J. Geophys. Res., 114(D00D16), doi:10.1029/2008JD011470.

Wild M. and A. Ohmura, 2004: BSRN longwave downward radiation measurements

combined with GCMs show promise for greenhouse detection studies, GEWEX news, 14(4), 20pp.
WMO, 2009: Technical Report of Global Analysis Method for Major Greenhouse Gases by the World Data Center for Greenhouse Gases. GAW Report, 184, WMO/TD No.1473.
WMO, 2018a: Scientific Assessment of Ozone Depletion: 2018. Global Ozone Research and Monitoring Project-Report, 58.
WMO, 2018b: WMO Greenhouse Gas Bulletin No.14. http://www.wmo.int/pages/prog/arep/gaw/ghg/GHGbulletin.html
WMO, 2019: WMO WDCGG DATA SUMMARY, WDCGG No.43, GAW Data Volume IV-Greenhouse Gases and Other Atmospheric Gases, published by the Japan Meteorological Agency in co-operation with World Meteorological Organization. Available at https://gaw.kishou.go.jp/publications/summary.